INSTITUTE OF PHYSICS OF THE POLISH ACADEMY OF SCIENCES

DOCTORAL THESIS

Formation of Pure and Surfactant-laden Droplets with Many-body Dissipative Particle Dynamics

---

Author:
Luís Henrique Carnevale da Cunha

Supervisor:
Panagiotis E. Theodorakis

A thesis submitted in fulfillment of the requirements
for the degree of Doctor of Philosophy
in the

Group of Soft Matter and Fluids Physics,
Division of Theoretical Physics

January 16, 2025

Declaration of Authorship

I, Luís Henrique Carnevale da Cunha, declare that this thesis titled, "Formation of Pure and Surfactant-laden Droplets with Many-body Dissipative Particle Dynamics", which is submitted in fulfillment of the requirements for the Degree of Doctor of Philosophy, represents my own work except where due acknowledgment have been made. I further declared that it has not been previously included in a thesis, dissertation, or report submitted to this Institute or to any other institution for a degree, diploma or other qualifications.

Signed: _____

Date: _____

Acknowledgements

I owe my deepest gratitude to my supervisor, Panos, whose exceptional mentorship has guided me not only in my research but also in my professional growth. His guidance and support extended beyond the scope of my research, significantly contributing to my professional development. Our insightful discussions were consistently rewarding and played a pivotal role in shaping both my studies and the writing of this thesis. I am equally grateful to my collaborators, Piotr Deuar and Zhizhao Che, whose active engagement in our productive group meetings was instrumental in advancing my research and contributing to our published work.

I am also deeply thankful to ThermaSMART for providing me with the opportunity to collaborate on a research project with Prof. Lennon Ó Náraigh at University College Dublin. Working with him was an enriching experience; not only did I acquire valuable new mathematical tools under his guidance, but I also thoroughly enjoyed our collaboration. Additionally, I am grateful to ThermaSMART for facilitating my research visit to the Federal University of Rio de Janeiro, where I had the privilege of working with Prof. Gustavo R. Anjos. His expertise and mentorship have profoundly influenced my research career.

This thesis was supported by the National Science Centre, Poland, under grant No. 2019/34/E/ST3/00232. I gratefully acknowledge Polish high-performance computing infrastructure PLGrid (HPC Centers: ACK Cyfronet AGH) for providing computer facilities and support within computational grants no. PLG/2020/014344, PLG/2022/015261, PLG/2022/015747, and PLG/2023/016608.

Abstract

Formation of Pure and Surfactant-laden Droplets with Many-body Dissipative Particle Dynamics

by Luís Henrique Carnevale da Cunha

This thesis employs many-body dissipative particle dynamics (MDPD) to investigate the molecular mechanisms underlying the breakup of pure and surfactant-laden liquid threads. MDPD is a particle-based mesoscale simulation technique that captures thermal fluctuations and soft-core interactions, bridging molecular and macroscopic scales. By simulating the Rayleigh–Plateau instability, MDPD provides critical insights into how molecular forces and thermal fluctuations influence droplet formation at nanoscales.

Surfactants, which adsorb at liquid interfaces and reduce surface tension, play a crucial role in altering the breakup dynamics of liquid threads. Their presence introduces additional complexity by driving Marangoni flows due to surface tension gradients. MDPD simulations demonstrate how surfactant concentration affects droplet size, distribution, and the formation of undesirable satellite droplets, offering strategies to mitigate these effects.

This study focuses on the interplay between molecular interactions and fluid instability during liquid thread breakup, highlighting how molecular-level mechanisms contribute to different breakup regimes. The findings advance the understanding of the Rayleigh–Plateau instability and provide practical insights for optimizing droplet formation in applications requiring precise control over fluid behavior.

By integrating molecular-level insights with mesoscale simulations, this research offers a framework for studying droplet formation and fluid instability. The results have significant implications for technologies such as nanotechnology manufacturing, microfluidics, and emulsification, paving the way for more efficient and controlled droplet-based systems.

Streszczenie

Formowanie kropel czystych i zawierających surfaktanty z dyssypacyjną dynamiką cząstek wielu ciał

Luís Henrique Carnevale da Cunha

W niniejszej rozprawie wykorzystano dynamikę cząstek dyssypatywnych wielu ciał (MDPD) do zbadania mechanizmów molekularnych leżących u podstaw rozpadu czystych i obciążonych surfaktantami nici cieczy. MDPD jest opartą na cząstkach techniką symulacji mezoskalowej, która wychwytuje fluktuacje termiczne i interakcje miękkiego rdzenia, łącząc skalę molekularną i makroskopową. Symulując niestabilność Rayleigha–Plateau, MDPD zapewnia krytyczny wgląd w to, jak siły molekularne i fluktuacje termiczne wpływają na tworzenie się kropli w nanoskali.

Środki powierzchniowo czynne, które adsorbują się na granicy faz cieczy i zmniejszają napięcie powierzchniowe, odgrywają kluczową rolę w zmianie dynamiki rozpadu ciekłych nici. Ich obecność wprowadza dodatkową złożoność poprzez napędzanie przepływów Marangoniego z powodu gradientów napięcia powierzchniowego. Symulacje MDPD pokazują, w jaki sposób stężenie środka powierzchniowo czynnego wpływa na wielkość kropli, rozkład i tworzenie niepożądanych kropel satelitarnych, oferując strategie łagodzenia tych efektów.

Niniejsze badanie koncentruje się na wzajemnym oddziaływaniu między interakcjami molekularnymi a niestabilnością płynu podczas rozpadu ciekłej nici, podkreślając, w jaki sposób mechanizmy na poziomie molekularnym przyczyniają się do różnych reżimów rozpadu. Odkrycia te przyczyniają się do lepszego zrozumienia niestabilności Rayleigha–Plateau i zapewniają praktyczny wgląd w optymalizację tworzenia kropli w zastosowaniach wymagających precyzyjnej kontroli nad zachowaniem płynu.

Integrując wiedzę na poziomie molekularnym z symulacjami mezoskalowymi, badania te oferują ramy do badania tworzenia się kropel i niestabilności płynów. Wyniki mają znaczący wpływ na technologie takie jak produkcja nanotechnologiczna, mikroprzepływy i emulgowanie, torując drogę do bardziej wydajnych i kontrolowanych systemów opartych na kroplach.

Contents

List of Figures

List of Tables

List of Publications

King L. Ng, **Luís H. Carnevale**, Michał Klamka, Piotr Deuar, Tomasz Bobinski, Panagiotis E. Theodorakis; Oscillations of a water droplet on a horizontally vibrating substrate. Physics of Fluids 2025; 37 (1): 014121. https://doi.org/10.1063/5.0250009

Luís H. Carnevale, Panagiotis E. Theodorakis; Many-body dissipative particle dynamics with the MARTINI "Lego" approach. European Physical Journal Plus 139, 539 (2024). https://doi.org/10.1140/epjp/s13360-024-05362-1 **Featured on the front cover of the journal**

Luís H. Carnevale, Piotr Deuar, Zhizhao Che, Panagiotis E. Theodorakis; Surfactant-laden liquid thread breakup driven by thermal fluctuations. Physics of Fluids 2024; 36 (3): 033301. https://doi.org/10.1063/5.0198154 **Editor's pick of Physics of Fluids**

Luís H. Carnevale, Piotr Deuar, Zhizhao Che, Panagiotis E. Theodorakis; Liquid thread breakup and the formation of satellite droplets. Physics of Fluids 2023; 35 (7): 074108. https://doi.org/10.1063/5.0157752 **Featured article in Physics of Fluids**

Chapter 1

Introduction

Droplets are all around us — from the formation of clouds in the sky to the condensation of dew droplets on a cold morning. They are present in various industrial applications, such as in spray technologies, cooling devices, chemical processing, and inkjet printing. The most ubiquitous physical process that generates droplets is that of the breakup of a liquid thread, or liquid jet, and its study can be traced back to the works of Savart [1], Plateau [2] and Rayleigh [3] in the 19^{th} century. They observed that small perturbations applied to a liquid jet are the source of an instability driven by surface tension that eventually leads to the breakup of the thread and subsequent formation of droplets. This process is known as the Rayleigh–Plateau instability.

While continuum theories, such as linear stability analysis, have long described the macroscopic dynamics of thread breakup, molecular-level insights are still required to fully understand the interplay of forces at nanoscales, especially in the presence of surfactants. Surfactants are amphiphilic molecules composed of hydrophilic and hydrophobic parts that adsorb at interfaces, reducing surface tension. This change in surface tension alters the dynamics of liquid thread breakup and understanding the role of surfactants in the formation of droplets requires detailed molecular-level investigation.

When a liquid thread reaches a small enough length scale, typically a few nanometers, thermal fluctuations due to molecular motion influence the breakup process [4, 5]. Thermal fluctuations compete against surface tension and induce surface thermocapillary waves which can drive the Rayleigh–Plateau instability. These waves have been experimentally observed at micrometer scales for certain complex liquid solutions, which exhibit extremely low interfacial tension [6–8].

In this thesis, many-body dissipative particle dynamics (MDPD) is employed to simulate the breakup of pure and surfactant-laden liquid threads to gain molecular-level insights into the formation of droplets. MDPD is a mesoscale computational method that bridges the gap between atomistic and macroscopic scales, capturing molecular interactions and thermal fluctuations [9–11]. Unlike traditional continuum models, MDPD incorporates stochastic forces to account for thermal fluctuations and uses soft-core potentials to simulate interactions between coarse-grained particles.

By shedding light on the molecular mechanisms underlying surfactant-laden liquid thread breakup, this work advances the understanding of fluid instability at molecular scales. These insights pave the way for the development of more precise and efficient droplet formation techniques, which are crucial for optimizing industrial processes in nanotechnology, printing, and emulsification. The ability to control droplet size and distribution through surfactant concentration and dynamic regime transitions offers a powerful tool for advancing technologies that rely on liquid thread manipulation.

In this chapter (Chapter 1) we provide a brief introduction on droplet formation and surfactants. In Chapter 2, we give a review on the MDPD simulation method and its theoretical background. Chapter 3 discusses the Rayleigh–Plateau instability and compares the continuum macroscopic predictions to MDPD simulations of pure liquids. Chapter 4 presents the MDPD surfactant model and applies it to the breakup of liquid threads. A conclusion to this thesis is presented in Chapter 5. A parametrization example to obtain MDPD interactions is given in Appendix A, which is part of our work towards a general-purpose MDPD forcefield.

1.1 Droplet Formation

Droplets can form through various mechanisms. Broadly, most methods of droplet generation involve free boundary problems that require the rupture or breakup of a larger liquid volume — a process that has been widely studied [12]. While this thesis primarily focuses on the breakup phenomenon, it is important to note that droplets can also form through other mechanisms, such as condensation or phase separation [13, 14]. Different breakup methods can be categorized into two main approaches: continuous production and drop-on-demand (DOD) production. Figure 1.1 provides a visual summary of these droplet generation techniques.

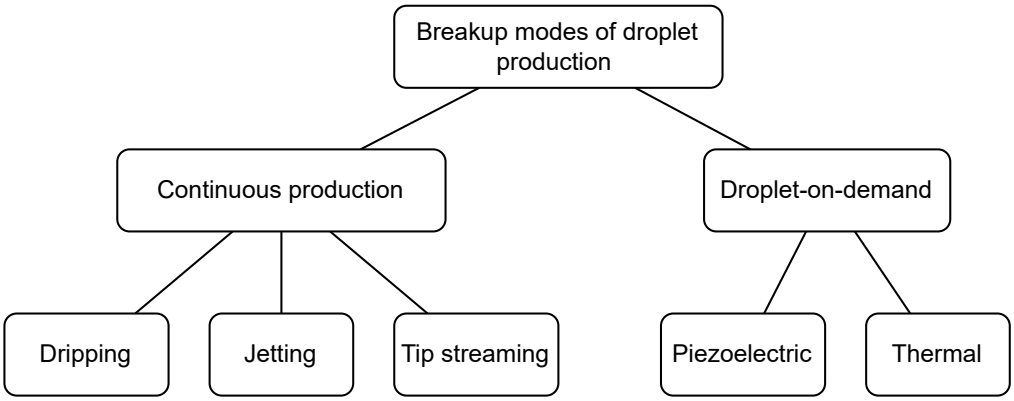

FIGURE 1.1: Classification of various droplet generation methods based on the breakup of a liquid volume.

Drop-on-demand methods produce individual droplets as needed, typically with high precision. One commonly used approach involves the activation of a piezoelectric element, which causes a nozzle to alternately contract and relax. This generates a pressure wave that ejects a single droplet, with its size determined by an appropriate electric signal [15]. Another widely used DOD method is the thermal inkjet technique, in which a small resistor heats the fluid until it vaporizes, forming a bubble. The rapid collapse of this bubble generates a pressure wave that propels a droplet out of the nozzle [16]. These techniques find applications in various fields, including inkjet printing [17] and tissue engineering [18], where precise droplet control is essential.

Continuous droplet production methods can be further divided based on the mode of breakup. Dripping is probably the most intuitive as most people have seen a leaky faucet. In dripping, droplets form directly at the exit of a capillary tube or nozzle when gravitational forces slightly exceed surface tension. This causes the fluid to elongate and eventually pinch off to form a droplet. If the flow rate is increased, dripping transitions into a jetting mode. In jetting, a continuous liquid column is expelled from the nozzle, eventually breaking into droplets due to the Rayleigh–Plateau instability. While dripping typically produces droplets with a more uniform size distribution, jetting enables much higher production rates. However, both modes can produce undesirable satellite droplets alongside the main droplets due to nonlinear effects [19]. The formation of these satellite droplets depends on the fluid's properties, such as viscosity and surface tension, and they are often undesirable in practical applications.

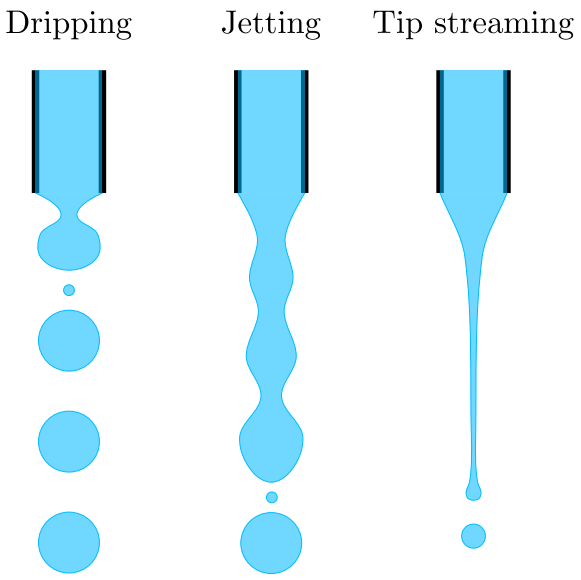

FIGURE 1.2: Schematic representation of different breakup modes present in continuous droplet formation techniques.

Another notable mode of breakup is tip streaming. In this mechanism, external forces direct the fluid to the tip of a deformed film or thin liquid thread, producing tiny droplets from the tip. Tip streaming is frequently observed in microfluidic systems, such as flow-focusing devices, where tangential interfacial stress between two fluids stretches the liquid into a thin thread. This technique can produce droplets up to two orders of magnitude smaller than the feeding capillary tube [20]. Figure 1.2 illustrates the differences among dripping, jetting, and tip streaming modes.

Breakup behavior is commonly characterized using dimensionless numbers, which encapsulate the interplay between various forces and fluid properties. These include:

$$\mathrm{Re} = \frac{\rho R U}{\mu}, \quad \mathrm{Ca} = \frac{\mu U}{\gamma}, \quad \mathrm{Bo} = \frac{\rho g R^2}{\gamma}, \quad \mathrm{We} = \frac{\rho R U^2}{\gamma}, \quad \mathrm{Oh} = \frac{\mu}{\sqrt{\rho R \gamma}}, \tag{1.1}$$

where ρ is the density, μ is the viscosity , γ is the surface tension, R is the droplet radius, U is the characteristic velocity, and g is the gravitational acceleration.

Each dimensionless number highlights a different balance of forces. For instance, the Reynolds number, Re, compares inertial to viscous forces, while the Weber number, We, compares inertial to surface tension forces. The Bond number, Bo, captures the influence of gravity relative to surface tension. Similarly, the Ohnesorge number, Oh, characterizes the balance between viscous, surface tension and

inertial forces, while the capillary number, Ca, reflects the relative significance of viscous forces compared to surface tension.

The transition between dripping and jetting has been shown to occur for We numbers above a critical value that depend on the Bo number [21]. However, relations between the Weber number and the capillary number can also be utilized to distinguish both breakup modes in certain systems [22]. Tip streaming requires a delicate balance between the forces acting on the fluid and its dynamics have been comprehensively reviewed in a recent study by Montanero and Gañán-Calvo [20].

This thesis concentrates on the Rayleigh–Plateau instability, making its findings particularly relevant to the jetting mode of droplet production. Despite this, the breakup process exhibits self-similar behavior near pinch-off, meaning that the local dynamics around the pinching point remain identical regardless of the global breakup mode under consideration [12]. Various scaling laws have been derived by seeking similarity solutions to approximations of the Navier–Stokes equations.

For inviscid liquids (I regime), where $\mathrm{Re} \gg \mathcal{O}(1)$, the pinching point radius, h_{min}, scales as $h_{\mathrm{min}} \sim \tau^{2/3}$, where $\tau = t_{\mathrm{breakup}} - t$ represents the time remaining until breakup [23]. In the opposite limit (V regime), where $\mathrm{Re} \ll \mathcal{O}(1)$, the pinching radius for a viscous liquid thread scales as $h_{\mathrm{min}} \sim \tau$ [24]. When both inertial and viscous forces are balanced (IV regime) and $\mathrm{Re} \approx \mathcal{O}(1)$, the pinching point also scales as $h_{\mathrm{min}} \sim \tau$, but with a different rate that depends on the Ohnesorge number [25].

Transitions between these regimes can occur during the breakup process, and it is generally believed that the final stage before pinch-off corresponds to the IV regime. The transition from the I to IV regime is expected to occur when $h_{\mathrm{min}} \sim \mathrm{Oh}^2$, while the transition from the V to IV regime is expected when $h_{\mathrm{min}} \sim \mathrm{Oh}^{2/(2\beta-1)}$, where $\beta = 0.175$ [26]. However, these transitions are far more complex, as many intermediate stages may arise during the breakup process [27].

The scaling laws mentioned above assume that the interface of a liquid thread be smooth at the smallest scales, in reality, the interface becomes rough due to thermal fluctuations near molecular scales, a phenomenon that has been experimentally observed [6]. These thermal fluctuations typically dominate the breakup process when the liquid thread radius becomes smaller than the thermal length scale $l_T = \sqrt{k_B T/\gamma}$, where k_B is the Boltzmann constant, and T the temperature. For water at room temperature, $l_T \approx 0.3$ nm — a scale that is extremely

challenging to observe experimentally. However, in certain complex liquid systems with sufficiently low interfacial tension, l_T can reach approximately 1 μm, making thermal fluctuations dominant at a more accessible scale [7]. A scaling law for the pinch-off in this situations (TF regime) has been semi-analytically obtained from a one-dimensional fluctuating hydrodynamic equation and is given by $h_{\min} \sim \tau^{0.418}$ [5]. The TF breakup regime has been experimentally observed for a phase separated colloid-polymer solution [8].

Surface tension plays a major role in droplet formation. From the dimensionless numbers in Eq. 1.1, we see its effect in determining the transition between dripping and jetting modes of droplets production. Surface tension also dictates which pinch-off regimes occur, their transitions, and is the driving force behind the Rayleigh–Plateau instability. Given its central importance, the ability to modify surface tension to enhance control over droplet production is highly desirable. The next section of this chapter introduces surfactants — molecules that can achieve precisely this.

1.2 Surfactants

Most chemical groups can be classified as either hydrophobic, meaning it is mostly repelled by water, or hydrophilic, meaning they are mostly attracted by water. Surfactants are a special class of molecules that contain both kinds of groups, namely, they are categorized as amphiphilic molecules (Fig. 1.3 a)). Due to their dual nature, surfactant molecules tend to accumulate at the interface between polar and apolar media, such as water–oil or water–air interfaces, lowering their interfacial tension. At low concentrations, most molecules will be found at the interface, but as the concentration increases, the interface becomes saturated and surfactants begin to aggregate in the bulk liquid. These situations are indicated in Fig. 1.3 b), where molecules aggregate in a micelle. Other kinds of aggregates can be formed depending on the concentration and molecular structure [28]. Another common aggregate phase is the lamellar bilayer (Fig. 1.3 c)). Lipids are a form of bio-surfactants that form such bilayers as a cell membrane [29]. Surfactants also play a role in stabilization of emulsions, as they preferentially increase the interfacial area between immiscible fluids [30].

The influence of surfactants in a system and how they affect surface tension can be quantified by the surface excess concentration, Γ. This quantity expresses how many more molecules are present at an interface when compared to the bulk. It

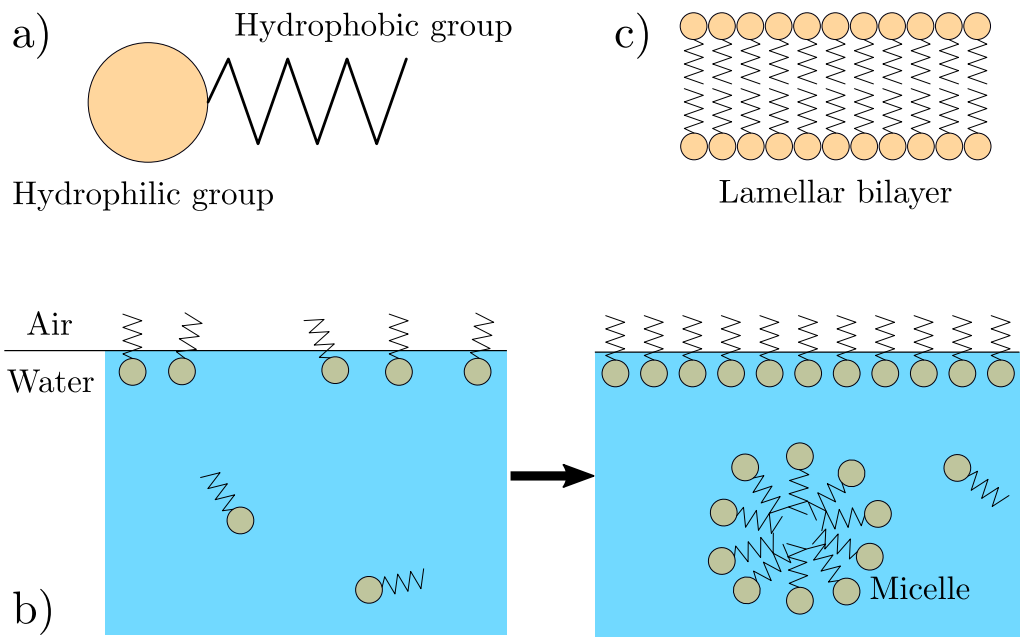

FIGURE 1.3: Representation of surfactant molecules and different systems. a) Generalized molecular structure of a surfactant in terms of hydrophobic and hydrophilic groups; b) Adsorption of surfactants at the interface and formation of micelles; c) Aggregation of surfactants in a lamellar bilayer.

can be computed by

$$\Gamma = \frac{N^{\text{total}} - N^{\alpha} - N^{\beta}}{A} = \frac{N}{A}\,, \tag{1.2}$$

where N^{total} is the total number of molecules present in the system, N^{α} is the number of molecules present in the bulk of phase α, N^{β} is the number of molecules present in the bulk of phase β, A is the interfacial area between phases α and β, and N is the number of molecules at the interface. The value of Γ is clearly positive for systems with surfactants, but it can also be negative when components that prefer to stay in the bulk phases are considered, such as ions. To understand the relevance of the surface excess concentration, we first need to define interfacial tension, also named surface tension when referred to liquid–vapor interfaces.

The origin of surface tension lies on the cohesive interactions between the molecules in a liquid. A molecule in the bulk of a liquid is completely surrounded by other molecules and is in a lower energetic state when compared to a molecule at an interface, where they have less interactions (Fig. 1.4). We can define surface tension, γ, as a measure of work necessary to change the interfacial area and, by assuming that the grand canonical surface free energy is $G^{\text{surface}} = A\gamma(T, \mu_i)$ [31], we arrive at

$$Ad\gamma = -SdT - \sum_i N_i d\mu_i, \tag{1.3}$$

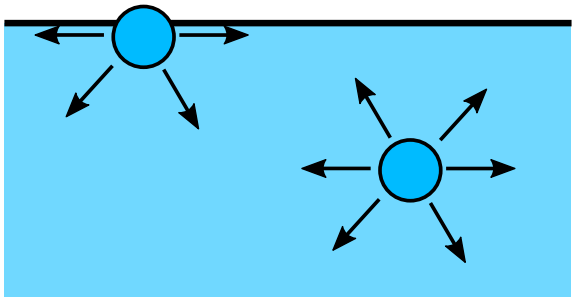

FIGURE 1.4: Schematic representation of the difference in cohesive interactions between a molecule at the interface and in the bulk of a liquid.

where S is the interface entropy, T is the temperature, and N_i, μ_i are the number of molecules and chemical potential of the i-th component of a system, respectively.

From the interfacial Gibbs–Duhem equation (Eq. 1.3) it is clear that for an ideal system with a single component at the interface

$$\left(\frac{\partial \gamma}{\partial \mu}\right)_T = -\frac{N}{A} = -\Gamma. \tag{1.4}$$

Therefore, a positive surface excess concentration will decrease interfacial tension, whereas a negative Γ will increase it.

During the breakup of a surfactant-laden liquid thread, surfactant molecules can be advected by the flow, leading to the formation of a surface concentration gradient. This gradient, in turn, creates a surface tension gradient that opposes the direction of advection. The transport mechanism induced by the surface tension gradient is known as the Marangoni effect, which tends to slow down the breakup dynamics [32, 33].

In the case of strong advection, the breakup still follows the scaling law $h_{\min} \sim \tau$ [34, 35]. However, in the opposite limit, where the surface concentration remains homogeneous, the breakup follows an exponential scaling law, $h_{\min} \sim e^{\tau}$, due to the difference between surface and bulk viscosity [36].

Given the complexity introduced by surfactants and the need to understand the breakup process at the molecular level, an appropriate simulation method must be employed. The next chapter will introduce many-body dissipative particle dynamics, a mesoscale particle-based method that can achieve this goal.

Chapter 2

Many-body Dissipative Particle Dynamics

The systems examined in this thesis operate on mesoscopic length scales, typically ranging from a few nanometers to tens of micrometers. At these scales, atomistic simulations become computationally prohibitive for investigating large systems over long time periods. This challenge is typically addressed using coarse-graining techniques, where groups of individual atoms are represented by an interaction site. In this context, we employ many-body dissipative particle dynamics (MDPD) as our method of choice. MDPD is an extension of dissipative particle dynamics (DPD) that allows for the simulation of liquid–vapor systems.

In this chapter, we provide a brief overview of the development of MDPD, beginning with standard DPD. In the final section, we outline the specific simulation details used for the practical implementation of the method, as well as the tools utilized.

2.1 Dissipative particle dynamics

Standard dissipative particle dynamics (DPD) was first introduced by Hoogerbrugge and Koelman [37] as an efficient particle-based method for simulating hydrodynamic systems. It offered significant computational advantages over traditional molecular dynamics (MD) while avoiding the limitations of the Lattice Gas Automata method, which constrained particles to move on a regular lattice. Hoogerbrugge and Koelman demonstrated that Navier–Stokes-like behavior naturally emerges from the interactions between particles, making DPD suitable for mesoscopic scales where thermal fluctuations and Brownian motion are significant.

Subsequently, Español and Warren [11] provided a rigorous statistical mechanics foundation for DPD by deriving a Fokker–Planck equation from a stochastic differential equation equivalent to the original DPD algorithm. In DPD, the equation of motion for a particle i with mass m and velocity $\boldsymbol{v}_i$ is given by:

$$m\frac{d\boldsymbol{v}_i}{dt} = \sum_{j\neq i} \boldsymbol{F}_{ij}^C + \boldsymbol{F}_{ij}^R + \boldsymbol{F}_{ij}^D, \tag{2.1}$$

where $\boldsymbol{F}_{ij}^C$ is the conservative force representing the interaction between particles i and j, while $\boldsymbol{F}_{ij}^R$ and $\boldsymbol{F}_{ij}^D$ are the random and dissipative forces, respectively, which together act as a thermostat to maintain the system's temperature. The explicit forms of these forces are as follows:

$$\boldsymbol{F}_{ij}^C = \begin{cases} a_{ij}\left(1-\frac{r_{ij}}{r_c}\right)\boldsymbol{e}_{ij}, & r_{ij} \leq r_c \\ 0, & r_{ij} > r_c \end{cases}, \tag{2.2}$$

$$\boldsymbol{F}_{ij}^D = -\sigma\omega^D(r_{ij})(\boldsymbol{e}_{ij}\cdot\boldsymbol{v}_{ij})\boldsymbol{e}_{ij}, \tag{2.3}$$

$$\boldsymbol{F}_{ij}^R = \xi\omega^R(r_{ij})\theta_{ij}(t)\boldsymbol{e}_{ij}. \tag{2.4}$$

All of the forces are assumed pair-wise additive and depend on the distance between particles $r_{ij} = |\boldsymbol{r}_{ij}| = |\boldsymbol{r}_i - \boldsymbol{r}_j|$, with $\boldsymbol{r}_i$ being the position vector of particle i. The direction of the forces is given by the unit vector $\boldsymbol{e}_{ij} = \boldsymbol{r}_{ij}/r_{ij}$. The strength of the conservative force in Eq. 2.2 is set by the parameter a_{ij} and it only acts on particles within the cutoff distance r_c. Usually in DPD this is a repulsive force, *i.e.* $a_{ij} > 0$.

On Eqs. 2.3, 2.4, $\boldsymbol{v}_{ij} = \boldsymbol{v}_i - \boldsymbol{v}_j$ is the relative velocity, σ is a parameter that sets the strength of dissipation, while ξ sets the strength of the random force. Both equations have the weight functions ω^D and ω^R. Español and Warren [11] has demonstrated the dependence between the parameters σ and ξ through the fluctuation–dissipation theorem, given by

$$\sigma = \frac{\xi^2}{2k_BT}, \tag{2.5}$$

where k_B is the Boltzmann constant and T the temperature of the system. Typically, in simulations, we set $k_BT = 1$ as our energy scale. The weight functions are also connected by the fluctuation-dissipation theorem and act only within the same cutoff r_c as

$$\omega^D(r_{ij}) = \left[\omega^R(r_{ij})\right]^2 = \left(1 - \frac{r_{ij}}{r_c}\right)^2. \tag{2.6}$$

Lastly, the time dependent term θ_{ij} in Eq. 2.4 is a symmetric Gaussian white-noise with zero mean and unit variance.

2.1.1 Equation of state and limitations

With the DPD model fully developed, Groot and Warren [38] studied the influence of the repulsion parameter a_{ij} in simulations to understand the thermodynamic behavior of the system. This was done by obtaining the equation of state (EOS) for the model by using the virial theorem

$$p = \rho k_B T + \frac{1}{3V}\left\langle \sum_{j>i} \boldsymbol{r}_{ij} \cdot \boldsymbol{F}_{ij}^C \right\rangle, \tag{2.7}$$

with p being the pressure, V the volume, and ρ the density of the system. The angle brackets denote ensemble average.

By doing simulations at different system conditions, Groot and Warren [38] managed to obtain an approximate EOS with quadratic dependence on the density, given by

$$p = \rho k_B T + ca\rho^2, \tag{2.8}$$

where $c = 0.101 \pm 0.001$ is a fitting parameter.

From this result, we can see the first limitation of the standard DPD method. Because of the purely quadratic dependence on density due to the form of conservative force, the model is not capable of producing liquid–vapor coexistence. Furthermore, Trofimov et al. [39] has shown that by mapping the isothermal compressibility of the simulations to a real system, the pressure will have an unrealistic high value.

2.2 Many-body dissipative particle dynamics

To overcome the limitations of standard DPD, Pagonabarraga and Frenkel [10] proposed a modification to the conservative interaction. This is done by assuming that the excess free energy of every particle is a function of its local density

$$\psi_i = f(\bar{\rho}_i) \tag{2.9}$$

$$\bar{\rho}_i = \sum_j w_\rho(r_{ij}) \tag{2.10}$$

where ψ_i is the free energy of particle i, $\bar{\rho}_i$ is its local density and $w_\rho(r_{ij})$ is a normalized weight function that depends only on the distance r_{ij} between particle i and its neighbors.

With this assumption, we can still write a pair wise additive force as

$$\boldsymbol{F}_i^C = -\sum_j \frac{\partial \psi_j}{\partial \boldsymbol{r}_{ij}} = -\sum_j \left(\psi_i' + \psi_j'\right) w_\rho'(r_{ij}) \boldsymbol{e}_{ij} \tag{2.11}$$

with $\boldsymbol{e}_{ij}$ being the unit vector pointing from particle i to j.

In essence, the function $f(\bar{\rho})$ can be chosen depending on the desired thermodynamics of the system. However, MDPD became widely used to study systems where liquid–gas phase separation is important and Warren [9] proposed a form of free energy function capable of modeling such systems and is the most used version of MDPD nowadays.

The free energy expression developed by Warren [9] contains an attractive and a repulsive term that act on neighbor particles within different cutoff distances r_c and r_d, respectively. The energy is given by

$$\psi_i = \frac{\pi r_c^4}{30} A \hat{\rho}_i + \frac{\pi r_d^4}{30} B \bar{\rho}_i^2, \tag{2.12}$$

where $A < 0$ is a parameter that sets the attractive strength and $B > 0$ sets the repulsive strength. The local densities are also defined for each cutoff as

$$\hat{\rho}_i = \sum_{j \neq i} \frac{15}{2\pi r_c^3} \left(1 - \frac{r_{ij}}{r_c}\right)^2, \tag{2.13}$$

$$\bar{\rho}_i = \sum_{j \neq i} \frac{15}{2\pi r_d^3} \left(1 - \frac{r_{ij}}{r_d}\right)^2. \tag{2.14}$$

These local density functions are the ones used in the vast majority of MDPD studies. However, functions like the Lucy kernel

$$\bar{\rho}_i = \sum_{j \neq i} \frac{105}{16\pi r_{c,d}^3} \left(1 + 3\frac{r_{ij}}{r_{c,d}}\right) \left(1 - \frac{r_{ij}}{r_{c,d}}\right)^3, \tag{2.15}$$

can also be chosen to compute local densities. Throughout this thesis we have used the Lucy Kernel on our simulations presented in Chapter 3 and the more standard Warren functions in Chapter 4. Both definitions were used because in the software used for our simulations, LAMMPS [40], only the Lucy kernel was originally implemented and we modified the source code to add the standard Warren weight function Warren [9] at a later stage.

The final form of the conservative force between particle i and j within MDPD is

$$\boldsymbol{F}_{ij}^C = A w^c(r_{ij}) \boldsymbol{e}_{ij} + B \left(\bar{\rho}_i + \bar{\rho}_j\right) w^d(r_{ij}) \boldsymbol{e}_{ij}, \tag{2.16}$$

and the weight functions that come from the choice of the local density form are

$$\omega^c(r_{ij}) = \begin{cases} 1 - \frac{r_{ij}}{r_c}, & r_{ij} \leq r_c \\ 0, & r_{ij} > r_c, \end{cases} \tag{2.17}$$

$$\omega^d(r_{ij}) = \begin{cases} 1 - \frac{r_{ij}}{r_d}, & r_{ij} \leq r_d \\ 0, & r_{ij} > r_d. \end{cases} \tag{2.18}$$

Typically, the value of the cutoff distance for interactions is set to $r_c = 1$ and $r_d = 0.75$ in MDPD units. These are the same values we adopted for all our simulations presented in this work.

It is worth noting that for the choice of free energy $\psi_i = A\bar{\rho}_i$ the traditional DPD method is recovered when $A > 0$. Also, the random and dissipative forces are kept the same as the original method (see Eqs. 2.3, 2.4).

2.2.1 Multicomponent systems

Trofimov et al. [39] has developed the theoretical background to extend MDPD for multicomponent systems. The generalization is done by first assuming a system with N_α components and defining partial local densities

$$\bar{\rho}_i^{(\alpha)} = \sum_{j,j\in\alpha} w(r_{ij}), \tag{2.19}$$

where every i-th particle has N_α different local densities, one for each component α. The free energy is then written as

$$\psi_i = \sum_\alpha f^{(\alpha)}\left(\bar{\rho}_i^{(\beta)}\right), \tag{2.20}$$

which expresses the interaction of a particle of type α with neighbors of type β. There is an ambiguity in the literature in how to combine these partial densities in the expression of excess free energy for each particle [41]. However, this discussion falls outside the scope of this thesis and, here, we follow Warren's self energy expression Warren [9] and the same procedure as for a single component system to obtain the conservative force

$$\boldsymbol{F}_{ij}^C = A_{ij} w^c(r_{ij}) \boldsymbol{e}_{ij} + B\left(\bar{\rho}_i + \bar{\rho}_j\right) w^d(r_{ij}) \boldsymbol{e}_{ij}. \tag{2.21}$$

The difference between Eq. 2.16 and Eq. 2.21 is only in the attractive term where now we have the matrix A_{ij} that sets the level of attraction between particle i and particle j depending on their respective types. Note that we do not have a matrix B_{ij} in the repulsive term. This is because Warren [42] derived MDPD's no-go theorem, which states that every element in the matrix B_{ij} has to have the same value to keep the force conservative. To prove this, we take only the repulsive term and assume that

$$\boldsymbol{F}^C = B_{ij}(\bar{\rho}_i + \bar{\rho}_j) w'_\rho(r_{ij}) \boldsymbol{e}_{ij}. \tag{2.22}$$

A necessary condition for a force to be conservative is to satisfy the Maxwell relation

$$\mathcal{D}_{ij} \equiv \frac{\partial \boldsymbol{F}_i}{\partial \boldsymbol{r}_j} - \frac{\partial \boldsymbol{F}_j}{\partial \boldsymbol{r}_i} = 0, \tag{2.23}$$

which should hold for any configuration of N particles. Without loss of generality, we can choose a system with only three co-linear particles at positions $x_1 < x_2 < x_3$. The distance between each particle is $x_{ij} = x_j - x_i$ and the forces between each particle are

$$F_{12} = -F_{21} = B_{12}(\bar{\rho}_1 + \bar{\rho}_2)w'_\rho(x_{12}) \tag{2.24}$$
$$F_{13} = -F_{31} = B_{13}(\bar{\rho}_1 + \bar{\rho}_3)w'_\rho(x_{13}) \tag{2.25}$$
$$F_{23} = -F_{32} = B_{23}(\bar{\rho}_2 + \bar{\rho}_3)w'_\rho(x_{23}). \tag{2.26}$$

The local densities are

$$\bar{\rho}_1 = w_\rho(x_{12}) + w_\rho(x_{13}) \tag{2.27}$$
$$\bar{\rho}_2 = w_\rho(x_{12}) + w_\rho(x_{23}) \tag{2.28}$$
$$\bar{\rho}_3 = w_\rho(x_{13}) + w_\rho(x_{23}). \tag{2.29}$$

By calculating every term $\mathcal{D}_{ij}$ we get that

$$\begin{aligned}\mathcal{D}_{12} = \mathcal{D}_{23} = \mathcal{D}_{31} = (B_{13} - B_{23})w'_\rho(x_{13})w'_\rho(x_{23}) \\ + (B_{12} - B_{13})w'_\rho(x_{12})w'_\rho(x_{13}) + (B_{12} - B_{23})w'_\rho(x_{12})w'_\rho(x_{23})\end{aligned} \tag{2.30}$$

from which we see that $\mathcal{D}_{ij}$ vanishes if and only if $B_{12} = B_{13} = B_{23}$. Thus B_{ij} has to have a single value B.

The no-go theorem imposes a constraint on the MDPD method for multicomponent systems. However, Vanya and Elliott [41] have proposed a way of circumventing this restriction by modifying the definition of the local densities and by fixing the ambiguity in the combination of the partial densities in the free energy.

2.2.2 Liquid properties and the equation of state

To demonstrate the improvement of MDPD over standard DPD, Warren [9] obtained an approximate equation of state from his definition of free energy that has a cubic dependence on density

$$p = \rho k_B T + \frac{\pi}{30}\left(A r_c^4 + 2B r_d^4 \rho\right)\rho^2, \tag{2.31}$$

which is capable of producing liquid/vapor coexistence. However, this was obtained from mean-field theory and the real EOS of the system deviates from Eq. 2.31 due to local density calculations. Different empirical equations have been

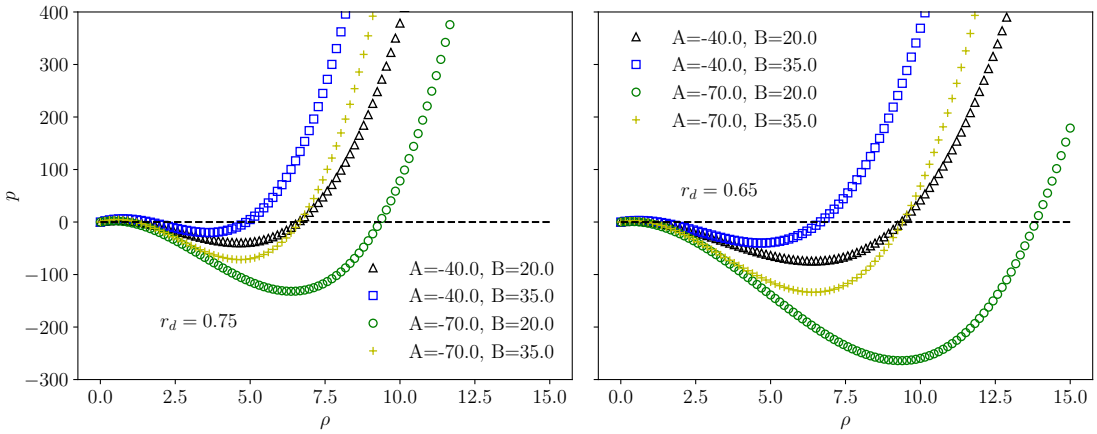

FIGURE 2.1: Empirical MDPD equation of state obtained by Jamali et al. [43]. Both plots have the same attractive cutoff $r_c = 1$ and different repulsive cutoff r_d. We see that the vapor phase has a density close to zero and that liquid densities can vary between 5 and 14 depending on the set of parameters.

proposed by fitting to simulation data and the most recent one was proposed by Jamali et al. [43]

$$p = \rho k_B T + \frac{\pi}{30} A r_c^4 \rho^2 + \frac{\pi}{15} B r_d^4 \left(\rho^3 - c\rho^2 + d\rho\right) - \frac{\pi B r_d^4}{30\sqrt{|A|}} \rho^2, \tag{2.32}$$

The EOS in MDPD is capable of representing the real model within a certain range of parameters and density of particles in the simulation domain [43]. The equation of state is shown in Fig. 2.1 for a few sets of parameters $\{A, B, r_d\}$ and keeping the cutoff $r_c = 1$. We can see the region of liquid–vapor coexistence and by requiring the pressure to vanish, we also obtain the particle density on each phase. Vanya et al. [44] has done a parametric study on various fluid properties at different sets of parameters and they arrived at a fitting equation for density of particles in MDPD as

$$\rho(A, B) = d_1(r_d) - A B^{d_3(r_d)} d_2(r_d) \tag{2.33}$$

where d_1, d_2 and d_3 are fitting parameters as a function of the repulsive cutoff.

Surface tension is another relevant fluid property that emerges from the model and understanding how it behaves as a function of the model parameters and its connection with real fluids is of great importance in simulating liquid–vapor systems. In MDPD we use the same procedures as in molecular dynamics to calculate surface tension, γ. Arienti et al. [45] used the mechanical route to compute

the surface tension from the pressure tensor across a planar interface normal to the z direction as

$$\gamma = L_z \left\langle P_{zz} - \frac{P_{yy} + P_{xx}}{2} \right\rangle \tag{2.34}$$

where L_z is the length of the computational domain and the pressure tensor can be computed from the virial definition using the Kirkwood–Buff method [46, 47]. From the simulation results and by comparing it to a mean-field expression for the surface tension, Arienti et al. [45] arrived at the fitting equation

$$\gamma = \frac{\pi}{240} \left(0.42 A r_c^5 \rho^2 + 0.003 B r_d^5 \rho^3 \right), \tag{2.35}$$

which depends on MDPD parameters and particle density. Ghoufi and Malfreyt [48] has shown that for a coarse-grained level where each one MDPD particle represents three water molecules, both density and surface tension can be mapped to values of real water, and Ghoufi et al. [49] shows that surface tension of the MDPD model decreases as a function of the curvature in small droplets. This change in surface tension is connected to the discussion of the Tolman length [50], which is still an open question in the literature whether surface tension should change and even if the Tolman length is positive or negative [51].

Another crucial hydrodynamic property that must be accurately captured by the model is viscosity. Marsh et al. [52] derived a Chapman–Enskog solution to the Fokker–Planck–Boltzmann equation, which provides an expression for viscosity arising from the dissipative interaction term, $\boldsymbol{F}^D$. Their analysis, however, neglected the contribution of conservative forces between particles. In contrast, Zhao et al. [53] demonstrated that in the case of MDPD, conservative forces also influence viscosity. Through MDPD simulations employing Lees–Edwards boundary conditions, they quantified both the dissipative and conservative contributions to viscosity, $\eta = \eta_C + \eta_D$, by varying simulation parameters A, B, r_d, and shear rate. Moreover, they confirmed the validity of the dissipative contribution derived by Marsh et al. [52] and proposed a fitting equation to account for the conservative contribution as

$$\eta_C = \kappa_1 \rho^{\kappa_2} B^2 \tag{2.36}$$

with the coefficients κ_1 and κ_2 being fitting parameters that depend on the repulsive cutoff r_d. Some typical values of the aforementioned properties are shown in Table 2.1 in MDPD units for different parameters. By changing the attractive and repulsive parameters A, B, and the cutoff, r_d, we can specify the fluid properties that closely resemble the system of interest in the simulation. Due to its simplicity

and flexibility, Zhao et al. [55] argued that MDPD is a promising method to study interfacial behavior at mesoscopic scales and complex fluids. Moreover, they also show validations of the method when applied to droplet and bubble dynamics, polymer solutions, capillary wetting, etc.

2.2.3 Parametrization and mapping to real liquids

Typically, reduced units are used to present MDPD results and to define simulation parameters and system properties. Moreover, using non-dimensional numbers calculated in the reduced units ensures a good way of comparing results to real physical measurements. In certain cases, as in the parametrization of general purpose force-fields, a direct relationship between reduced units to real units is desirable. A force-field is a set of parameters that define all the interactions and topology between different kinds of particles and is usually applied to a specific simulation method. An example of parametrization of an MDPD force-field is presented in Appendix A. The parametrization follows the same strategy as the one used in the coarse-grained molecular dynamics force-field Martini [56, 57].

There are different ways of mapping MDPD units to real units. In this thesis, we use a semi-top-down approach based on the coarse-grained degree N_{CG} [48] and matching surface tension. The CG degree indicates how many real molecules (or atoms) a single MDPD particle represents. The reduced units in MDPD are set such that $m = r_c = k_B T = 1$. To compare these units to real units, we use the superscript * to denote a variable in MDPD units. Variables without the superscript are expressed in real units. This notation follows until the end of this section or when stated otherwise.

TABLE 2.1: Fluid properties in MDPD units obtained for different attractive parameter values, A, in the MDPD model. The density, ρ, was obtained from the simulation, the surface tension, γ, and the viscosity, η, were calculated from fitting equations from Refs. [45] and [53], respectively. All values were obtained by keeping $B = 25$ and $r_d = 0.75$ as in Ref. [54].

A	ρ	γ	η
-40	6.1	7.95	4.06
-50	6.9	12.5	7.22
-60	7.7	19.45	10.76
-70	8.4	26.76	18.31
-80	9.1	36.25	33.90

The length-scale mapping is obtained from the volume of a single molecule, v_0, and the densities in the simulation, ρ^* [58]. The number of molecules in a cube with volume r_c^3 is given by $N = r_c^3/v_0$, while the molecular volume is calculated by

$$v_0 = \frac{M}{N_a \rho}, \tag{2.37}$$

where M is the molar mass, and $N_a = 6.023 \times 10^{23}$ is Avogadro's number. However, the number of MDPD particles in a cube with volume r_c^{*3} is $N^* = \rho^*$. From the definition of CG degree we can equate

$$\rho^* N_{CG} = \frac{r_c^3}{v_0}, \tag{2.38}$$

which leads to

$$r_c = \left(\rho^* N_{CG} v_0\right)^{1/3}. \tag{2.39}$$

As an example, a simulation with the set of parameters $A = -40$, $B = 25$ and $r_d = 0.75$ has bulk liquid density $\rho^* = 6.1$ (see Tab. 2.1). By mapping three water molecules per MDPD particle, and knowing that the volume of a water molecule is $v_0 = 30$ Å^3, the length scale is $r_c = (6.1 \times 3 \times 30)^{1/3} = 8.2$ Å.

To match the surface tension, we use dimensional analysis. Using the notation $[M]$, $[L]$ and $[T]$ to denote mass, length, and time units, we can represent the dimensions of surface tension as $[\gamma] = [MT^{-2}]$. Our reference units have dimensions $[r_c] = [L]$, $[m] = [M]$ and $[k_B T] = [ML^2T^{-2}]$. We can express surface tension in terms of the reference units by requiring a dimensionless product:

$$\begin{aligned} [\gamma^{-1} r_c^{v_1} m^{v_2} (k_B T)^{v_3}] &= [MT^{-2}]^{-1} [L]^{v_1} [M]^{v_2} [ML^2T^{-2}]^{v_3} && (2.40) \\ &= [M]^{-1+v_2+v_3} [L]^{v_1+2v_3} [T]^{2-2v_3}. && (2.41) \end{aligned}$$

For the product to be dimensionless, all the exponents have to be equal to zero. These are obtained from the system

$$\begin{cases} -1 + v_2 + v_3 = 0 \\ v_1 + v_3 = 0 \\ 2 - 2v_3 = 0 \end{cases}, \tag{2.42}$$

with solution $v_1 = -2$, $v_2 = 0$, and $v_3 = 1$. This sets the correspondence between the MDPD and real surface tension as

$$\gamma = \gamma^* \frac{k_B T}{r_c^2}. \tag{2.43}$$

Using the same parameters as in the previous water example and assuming room temperature conditions, where $k_B T = 4.11 \times 10^{-21}$ J, the surface tension calculated from Eq. 2.43 is $\gamma = 48.6$ mN/m. This value is significantly lower than the experimentally observed surface tension of real water, approximately 72 mN/m. This discrepancy may stem from the absence of a scaling dependence on the coarse-graining level in Eq. 2.43 [59].

Nevertheless, it is possible to address this issue by solving an optimization problem to determine a specific set of parameters that accurately reproduces both the density and surface tension of water [47]. For a CG level of $N_{CG} = 3$, the parameter set that achieves this is $A = -50$, $B = 25$, and $r_d = 0.75$.

2.3 Modified Velocity-Verlet algorithm

With the full model described above, we now focus on the numerical integration of the equations of motion (see Eq. 2.1) for each particle. This is accomplished using a finite difference technique known as the modified velocity-Verlet (MVV) method, which is widely employed in molecular dynamics (MD) simulations. It differs from the standard velocity-Verlet method by the inclusion of an intermediate velocity step calculation that can be empirically varied by the order parameter, λ. The MVV method also offers superior performance when compared to other methods, such as the Euler method, due to its enhanced numerical stability, time reversibility, and reduced numerical error (second order in time, as opposed to the first-order error in Euler's method). Additionally, MVV is classified as a symplectic integrator, meaning it preserves the system's energy over time and avoids the energy drift commonly observed in non-symplectic methods, such as Euler and Runge–Kutta.

The position $\boldsymbol{r}$ and velocity $\boldsymbol{v}$ of each particle are updated at discrete time intervals, with a time step Δt, following the sequence:

$$\boldsymbol{r}(t+\Delta t) = \boldsymbol{r}(t) + \Delta t \boldsymbol{v}(t) + \frac{1}{2}\Delta t^2 \boldsymbol{F}(t) \tag{2.44}$$

$$\tilde{\boldsymbol{v}}(t+\Delta t) = \boldsymbol{v}(t) + \lambda \Delta t \boldsymbol{F}(t) \tag{2.45}$$

$$\boldsymbol{F}(t+\Delta t) = \boldsymbol{F}\left(\boldsymbol{r}(t+\Delta t), \tilde{\boldsymbol{v}}(t+\Delta t)\right) \tag{2.46}$$

$$\boldsymbol{v}(t+\Delta t) = \boldsymbol{v}(t) + \frac{1}{2}\Delta t \left(\boldsymbol{F}(t) + \boldsymbol{F}(t+\Delta t)\right) \tag{2.47}$$

An intermediate velocity step, $\tilde{\boldsymbol{v}}$, is introduced in Eq. 2.45 to compute the updated forces, and the actual velocity at time $t + \Delta t$ is then corrected in the final step (Eq. 2.47). The parameter λ is an empirical factor that accounts for additional effects arising from stochastic interactions.

When computing the random force, special care is needed, as it is expressed as:

$$\boldsymbol{F}_{ij}^R = \xi \omega^R(r_{ij}) \theta_{ij} \Delta t^{-1/2} \boldsymbol{e}_{ij}. \tag{2.48}$$

The inclusion of the $\Delta t^{-1/2}$ term can be derived by treating the random force as a Wiener process [11]. Heuristically, this can be understood by considering the random force as generating a random walk. In such a walk, the root mean square displacement of a particle is proportional to the square root of the number of steps, which corresponds to Δt in this context. Consequently, we assume that $\langle f^2 \rangle \sim \xi^2 / \Delta t$, where f is the random force acting on a particle [38].

2.4 Software

All simulations discussed in this thesis were performed using the open-source software LAMMPS (Large-scale Atomic/Molecular Massively Parallel Simulator) [40]. LAMMPS provides parallelized C++ implementations of the modified velocity-Verlet (MVV) algorithm, and the many-body dissipative particle dynamics (MDPD) interactions were integrated through a user- defined package, DPD-MESO [60]. LAMMPS is highly regarded for its extensive documentation, large user community, and its ability to accommodate custom modifications when necessary. Notably, the results presented in Chapter 4 were obtained by modifying the local density function within the DPD-MESO package's source code.

For simulations involving more complex molecular structures, Packmol and Moltemplate [61, 62] were employed to construct the initial configurations and

molecular structures, which were subsequently exported as LAMMPS data files. The software OVITO [63] was used to visualize the simulation trajectories. The free, open-source version of OVITO includes a Python API, which was utilized alongside custom scripts developed in-house to perform the analysis detailed in this thesis.

Chapter 3

Rayleigh–Plateau Instability

The Rayleigh–Plateau instability is a fundamental phenomenon in fluid dynamics that describes the spontaneous breakup of a liquid cylinder or thread into smaller droplets due to surface tension. First studied by Joseph Plateau in the 19th century and later mathematically formulated by Lord Rayleigh, this instability occurs when a liquid column or jet is perturbed, causing its surface energy to decrease as the column elongates and forms distinct, periodic bulges. These bulges eventually pinch-off, minimizing the system's overall surface energy and leading to the formation of droplets.

The breakup instability plays a crucial role in various natural and industrial processes [4], including inkjet printing [17, 64], spray formation [65], nanoscale manufacturing and chemical processing [66], and liquid jets [25, 26]. It provides insight into the balance between cohesive forces within a liquid and the disruptive influence of surface tension [27]. Understanding this instability not only enhances our theoretical knowledge of fluid behavior, but, also, has practical implications for designing technologies that involve the manipulation of liquids at small scales.

In this thesis, we aim to explore the mechanisms driving the Rayleigh–Plateau instability, by first deriving the stability argument given by Plateau and exposing Rayleigh's linear stability analysis for the case of inviscid liquid threads, i.e., by assuming no viscous effects. To further explore this phenomena, we will investigate the influence of thermal fluctuations in the breakup of liquid jets by performing mesoscale simulations. We will measure the characteristic wavelength that leads to the breakup of jets with different fluid properties and compare it to analytical expressions. Moreover, we will investigate post-breakup dynamics of droplet formation. Most of the simulation results shown in this chapter were presented in one of our publications (see Ref. [67]).

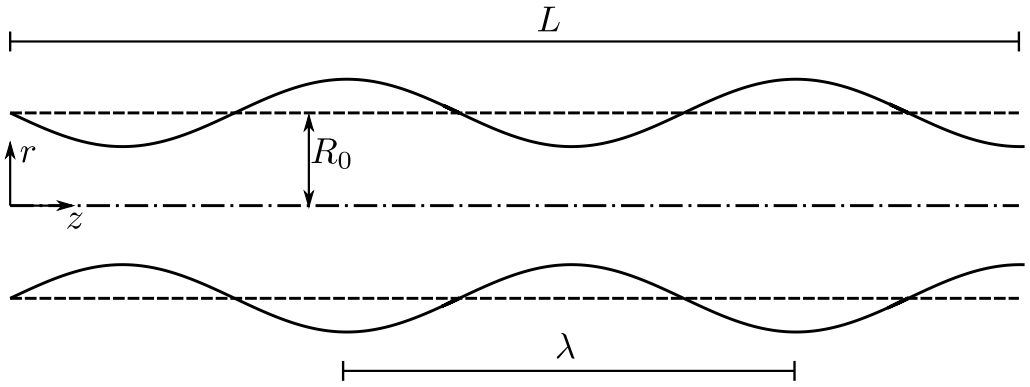

FIGURE 3.1: Schematic of the initial configuration of the system (dashed line) and the evolution of the breakup of a liquid thread of an initial radius, R_0. A typical periodic perturbation is represented by the solid lines with a given wavelength λ. Adapted from Carnevale et al. [67] with permission by AIP Publishing.

3.1 Stability

3.1.1 Plateau's energy analysis

Plateau derived the stability condition of a liquid thread by considering that small perturbations alter the surface area of the system, leading to a change in surface energy. For certain wavelengths, the liquid thread will transition to a lower energy state, which is energetically favorable. The surface free energy E of a liquid is related to its surface area A and surface tension γ, expressed as:

$$\delta E = \gamma \delta A \tag{3.1}$$

For an initial liquid thread of radius R_0, length L, and with its axis in the z direction as depicted in Fig. 3.1, the surface energy is given by:

$$E_0 = \int_0^L R_0 2\pi\gamma dz = 2\pi\gamma R_0 L. \tag{3.2}$$

Any perturbations along the azimuthal direction will lead to an increase in surface area, therefore they must be stable. Moreover, undulations of the jet axis will not change the surface area. Thus, we only need to consider axisymmetric perturbations that change the radius along its axis. Such perturbations can be modeled as:

$$h(z) = h_0 + \epsilon \cos(kz), \tag{3.3}$$

where ϵ is a small perturbation amplitude, k is the wavenumber (related to the wavelength by $k\lambda = 2\pi$), $h(z)$ is the thread radius at position z, and h_0 is the mean radius of the distorted cylinder which equals the initial radius only when $\epsilon = 0$. To obtain a relation between the mean radius and the initial radius, we require that the liquid thread volume remains constant, and we only need to integrate over one wavelength due to the periodicity of the perturbation

$$\int_0^\lambda \pi h^2 dz = \pi R_0^2 \lambda \tag{3.4}$$

$$\int_0^\lambda \left(h_0 + \epsilon\cos(kz)\right)^2 dz = R_0^2\lambda \tag{3.5}$$

$$h_0^2\lambda + 2h_0\epsilon\int_0^\lambda \cos(kz)dz + \epsilon^2\int_0^\lambda \cos^2(kz)dz = R_0^2\lambda \tag{3.6}$$

$$h_0^2\lambda + \frac{\epsilon^2\lambda}{2} = R_0^2\lambda \tag{3.7}$$

using the approximation for small x:

$$(1+x)^{1/2} \approx \left(1 + \frac{x}{2}\right), \tag{3.8}$$

we obtain the following relationship between the mean radius and the initial radius:

$$h_0 = R_0\left(1 - \frac{\epsilon^2}{4R_0^2}\right). \tag{3.9}$$

To evaluate the surface energy of the distorted liquid thread, we compute:

$$E = 2\pi\gamma\int_0^\lambda h\left(1 + h'^2\right)^{1/2} dz \tag{3.10}$$

where prime denotes the derivative in z direction. By using the approximation in Eq. 3.8 we proceed as

$$E = 2\pi\gamma\int_0^\lambda h\left(1 + \frac{h'^2}{2}\right) dz \tag{3.11}$$

$$E = 2\pi\gamma\int_0^\lambda \left[h_0 + \frac{h_0k^2\epsilon^2}{2}\sin^2(kz) + \epsilon\cos(kz) + \frac{k^2\epsilon^3}{2}\sin^2(kz)cos(kz)\right] dz \tag{3.12}$$

$$E = 2\pi\gamma h_0\lambda\left(1 + \frac{k^2\epsilon^2\pi^2 h_0}{4}\right). \tag{3.13}$$

By substituting h_0 in Eq. 3.13 by Eq. 3.9 we can calculate the change in energy $\Delta E = E - E_0$ as:

$$\Delta E = \frac{\pi\gamma\epsilon^2\lambda}{4R_0}\left[(kR_0)^2 - 1\right]. \tag{3.14}$$

The change in energy is negative if, and only if, $(kR_0)^2 < 1$, or equivalently, $\lambda > 2\pi R_0$. This indicates that perturbations with wavelengths greater than the circumference of the liquid thread are unstable, a conclusion reached by Plateau [68].

3.1.2 Linear stability analysis

Rayleigh was the first to apply linear stability analysis to study the liquid jet instability in a more detailed manner [69]. To obtain a dispersion relation that describes the growth rate of perturbations of different wavelengths, we consider an incompressible, inviscid fluid at a stationary base state. Our problem is governed by the Euler and continuity equations:

$$\frac{\partial \boldsymbol{v}}{\partial t} + \boldsymbol{v}\cdot\nabla\boldsymbol{v} = -\frac{1}{\rho}\nabla p \tag{3.15}$$

$$\nabla\cdot\boldsymbol{v} = 0. \tag{3.16}$$

We can decompose the velocity field in a base state solution plus a perturbation as $\boldsymbol{v} = \boldsymbol{v}_0 + \boldsymbol{v}'$ and the pressure $p = p_0 + p'$. Because we assume a stationary base state, the velocity $\boldsymbol{v_0} = 0$ and p_0 is equal to the Laplace pressure, which will be used later on. To proceed, we add these perturbations to the governing equations and consider only the axisymmetric case:

$$\frac{\partial v_r}{\partial t} = -\frac{1}{\rho}\frac{\partial p'}{\partial r} \tag{3.17}$$

$$\frac{\partial v_z}{\partial t} = -\frac{1}{\rho}\frac{\partial p'}{\partial z} \tag{3.18}$$

$$\frac{\partial v_r}{\partial r} + \frac{\partial v_z}{\partial z} + \frac{v_r}{r} = 0, \tag{3.19}$$

where v_r and v_z are the perturbations in the radial and axial direction, respectively. Moreover, the non-linear terms were neglected as perturbations are small, resulting in linear equations. We are looking for distortions of the interface of the form $h(z,t) = h_0 + \epsilon e^{\omega t + ikz}$, thus we anticipate that the perturbations will be of

the form:

$$v_r = R(r)e^{\omega t+ikz} \tag{3.20}$$

$$v_z = Z(r)e^{\omega t+ikz} \tag{3.21}$$

$$p' = P(r)e^{\omega t+ikz}, \tag{3.22}$$

where ω is the growth rate, $i = \sqrt{-1}$, and k the wavenumber.

Substituting Eqs. 3.20–3.22 in Eqs. 3.17–3.19 we obtain:

$$\frac{\partial P(r)}{\partial r} = -\rho\omega R(r) \tag{3.23}$$

$$ikP(r) = -\rho\omega Z(r) \tag{3.24}$$

$$\frac{\partial R(r)}{\partial r} + \frac{R(r)}{r} + ikZ(r) = 0. \tag{3.25}$$

By differentiating Eqs. 3.24, 3.25 with respect to r and then combining with Eq. 3.23 we arrive at:

$$r^2\frac{\partial^2 R(r)}{\partial r^2} + r\frac{\partial R(r)}{\partial r} - \left(1 + k^2r^2\right)R(r) = 0. \tag{3.26}$$

Equation 3.26 has a general solution in terms of the modified Bessel functions of the first and second kinds:

$$R(r) = C_1 I_1(kr) + C_2 K_1(kr), \tag{3.27}$$

where the constant C_2 has to vanish because the modified Bessel function of the second kind $K_1(kr) \to \infty$ as $r \to 0$ and we require our solution to be well behaved at the origin.

To determine the coefficient C_1 we use the kinematic boundary condition:

$$\frac{\partial H}{\partial t} + \boldsymbol{v} \cdot (\nabla H) = 0, \tag{3.28}$$

which describes the motion of an interface defined by a function, H which is constant exactly at the interface. This function for our problem is $H = r - h(z,t)$.

Substituting in the kinematic boundary condition at the base state interface position $r = h_0$ and neglecting the terms of order ϵ^2 we get:

$$\frac{\partial}{\partial t}(r-h) + v_r\frac{\partial}{\partial r}(r-h) + v_z\frac{\partial}{\partial z}(r-h) = 0 \tag{3.29}$$

$$\frac{\partial h}{\partial t} + v_z\frac{\partial h}{\partial z} = v_r \tag{3.30}$$

$$\frac{\partial}{\partial t}\left(h_0 + \epsilon e^{\omega t+ikz}\right) = v_r \tag{3.31}$$

$$\epsilon\omega e^{\omega t+ikz} = R(h_0)e^{\omega t+ikz} \tag{3.32}$$

$$\epsilon\omega = C_1 I_1(kh_0) \tag{3.33}$$

$$C_1 = \frac{\epsilon\omega}{I_1(kh_0)}. \tag{3.34}$$

Combining Eqs. 3.23, 3.27, 3.34 and integrating it by using the property of Bessel function $I_0'(kr) = kI_1(kr)$ with prime denoting derivative in r, we find that:

$$P(r) = -\frac{\rho\omega^2\epsilon}{k}\frac{I_0(kr)}{I_1(kh_0)}, \tag{3.35}$$

so that:

$$p' = -\frac{\rho\omega^2\epsilon}{k}\frac{I_0(kr)}{I_1(kh_0)}e^{\omega t+ikz}. \tag{3.36}$$

The next step needed to find the dispersion relation is to require a stress balance at the interface. This is done by using the Young–Laplace equation:

$$p - p_\infty = \gamma\nabla\cdot\hat{\boldsymbol{n}} = \gamma\left(\frac{1}{R_1} + \frac{1}{R_2}\right) \tag{3.37}$$

where p_∞ is the pressure outside of the cylinder, taken as equal to zero. The unit vector $\hat{\boldsymbol{n}}$ is normal to the interface and R_1, R_2 are the principal radii of curvature. The normal vector can be calculated from our surface function H:

$$\hat{\boldsymbol{n}} = \frac{\nabla H}{|\nabla H|} = \frac{1}{\left(1+h'^2\right)^{1/2}}\boldsymbol{e}_r - \frac{h'}{\left(1+h'^2\right)^{1/2}}\boldsymbol{e}_z \tag{3.38}$$

where primes denote derivative in z direction. The mean curvature is:

$$\nabla\cdot\hat{\boldsymbol{n}} = \frac{1}{h\left(1+h'^2\right)^{1/2}} - \frac{h''}{\left(1+h'^2\right)^{3/2}}. \tag{3.39}$$

For the base state cylinder, the surface is described by setting $h(z,t) = h_0$ so the Laplace pressure is:

$$p_0 = \frac{\gamma}{h_0} \tag{3.40}$$

The Laplace pressure on the perturbed cylinder is computed by setting $h(z,t) = h_0 + \epsilon e^{\omega t + ikz}$ and by neglecting the terms of order ϵ^2, so:

$$p = \gamma \nabla \cdot \hat{\boldsymbol{n}} \tag{3.41}$$

$$p_0 + p' = -\gamma \left(\frac{1}{h} - h'' \right) \tag{3.42}$$

$$\frac{\gamma}{h_0} + p' = \gamma \left(\frac{1}{h_0 + \epsilon e^{\omega t + ikz}} - \frac{\partial^2}{\partial z^2} \left(h_0 + \epsilon e^{\omega t + ikz} \right) \right) \tag{3.43}$$

$$\frac{\gamma}{h_0} + p' = \gamma \left(\frac{h_0 - \epsilon e^{\omega t + ikz}}{h_0^2 - \epsilon^2 e^{2\omega t + 2ikz}} - \epsilon i^2 k^2 e^{\omega t + ikz} \right) \tag{3.44}$$

$$\frac{\gamma}{h_0} + p' = \gamma \left(\frac{1}{h_0} - \frac{\epsilon e^{\omega t + ikz}}{h_0^2} + \epsilon k^2 e^{\omega t + ikz} \right) \tag{3.45}$$

$$p' = \gamma \epsilon \left(-\frac{1}{h_0^2} + k^2 \right) e^{\omega t + ikz} \tag{3.46}$$

Lastly, comparing Eqs. 3.46 and 3.36 at $r = h_0$, and because we are neglecting quadratic terms in ϵ, $h_0 = R_0$, we find the dispersion relation:

$$\omega^2 = \frac{\gamma k}{\rho R_0^2} \frac{I_1(kR_0)}{I_0(kR_0)} \left(1 - k^2 R_0^2 \right) \tag{3.47}$$

The perturbations will grow when $\omega^2 > 0$ and this is true if, and only if, $kR_0 < 1$, or equivalently, $2\pi R_0 < \lambda$, which is the same conclusion reached by Plateau.

In Rayleigh's solution, however, only inviscid fluids were considered, so the effect of viscosity was neglected at first. Effects of viscosity were later introduced by Rayleigh [70] by assuming the fluid is described on the basis of the Stokes equation. The full dispersion relation for an arbitrary fluid derived from the Navier–Stokes equation is attributed to Chandrasekhar [71]. However, its derivation is quite long, hence we will omit it here and only present the approximate relation:

$$\frac{\omega}{\omega_0} = \sqrt{\frac{1}{2}(\chi^2 - \chi^4) + \frac{9}{4}\mathrm{Oh}^2 \chi^4} - \frac{3}{2}\mathrm{Oh}\chi^2, \tag{3.48}$$

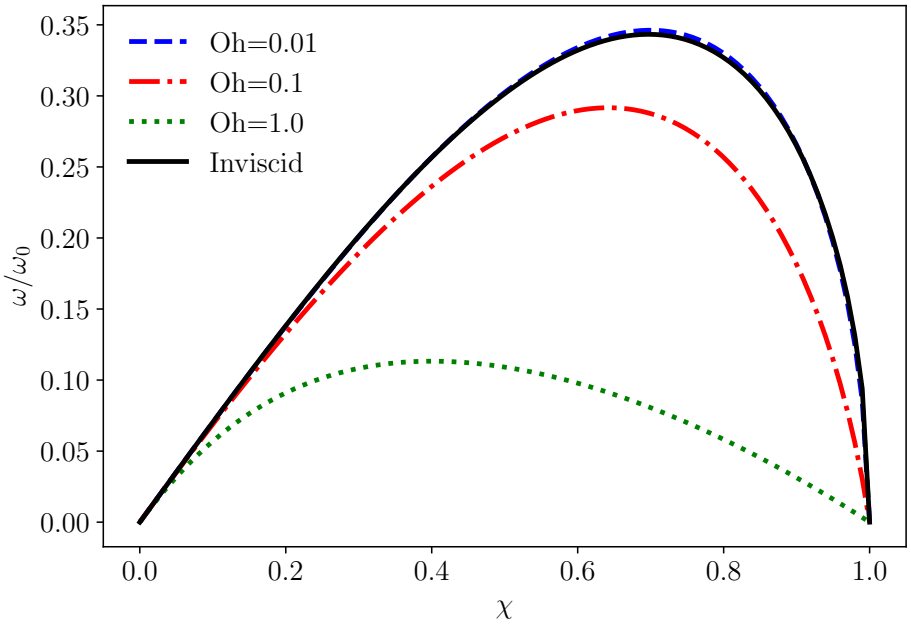

FIGURE 3.2: Growth rate of perturbations as a function of the reduced wavenumber $\chi = kR_0$. The inviscid case was plotted with Eq. 3.47 and the viscous cases with Eq. 3.48.

which was first obtained by Weber [72] and can be derived by an expansion of Chandrasekhar's solution. In Eq. 3.48, $\chi = kR_0$, Oh is the non-dimensional Ohnesorge number, which indicates the ratio of viscosity, μ, to surface tension and inertia. It is defined as:

$$\mathrm{Oh} = \frac{\mu}{\sqrt{\rho\gamma R_0}}. \tag{3.49}$$

The frequency, ω_0, is the inverse of the fluid inertial time scale and is defined as:

$$\omega_0 = \sqrt{\frac{\gamma}{\rho R_0^3}} = t_I^{-1} \tag{3.50}$$

The dispersion relation in Eq. 3.47 is plotted in Fig. 3.2 together with Eq. 3.48 for different Oh numbers as a function of the reduced wavenumber $\chi = kR_0$. We see from the figure that the viscous solution approaches the inviscid one in the limit $Oh \to 0$. Moreover, there is a wavenumber for which the growth rate is maximum. In the case of inviscid liquids, this is known as the Rayleigh mode, and its value is $\chi = 0.697$. For viscous fluids this point depends on Oh and can

be analytically calculated as:

$$\chi = \sqrt{\frac{1}{2+\sqrt{18}\mathrm{Oh}}}. \tag{3.51}$$

3.2 Simulations

It is possible to use the theory developed so far and the literature on the breakup of liquid threads to predict the formation of droplets and apply it in many practical systems. The most unstable perturbations and dispersion relations have been confirmed experimentally [73]. However, the influence of perturbations at the molecular-scale has not been properly quantified [74, 75].

While the process is fundamentally driven by surface tension, and affected by inertial and viscous forces, we expect that thermal fluctuations also play a role in the phenomena [4, 7, 8]. The importance of these fluctuations in our system can be determined by the non-dimensional number, Th, which we call the thermo-capillary number [76]. This number is defined as:

$$\mathrm{Th} = \sqrt{\frac{k_B T}{\gamma R_0^2}}. \tag{3.52}$$

To simulate the breakup of a liquid thread, we start by generating our initial system (Fig. 3.3) as randomly distributed particles in a cylindrical region of space with initial radius R_0 and length L. The number of particles is set by the density of the liquid phase at the liquid–vapor coexistence region in the equations of state presented in Chapter 2. The simulation parameters $B = 25$, $r_c = 1$, $r_d = 0.75$, and $\sigma = 18$, where kept the same for all simulations as we varied the attractive

TABLE 3.1: Fluid properties obtained for different A values in the MDPD model based on the Lucy Kernel. The density, ρ, was obtained from simulations, the surface tension, γ, and the viscosity, μ, were calculated from fitting equations 2.35, 2.36, respectively.

A	ρ	γ	μ
-40	6.75	9.95	4.06
-50	7.65	15.98	7.22
-60	8.30	22.60	10.76
-70	8.95	30.66	18.31
-80	9.60	40.29	33.90
-85	9.92	45.73	47.02
-90	10.24	51.62	64.01

FIGURE 3.3: Characteristic snapshots from the simulations during the time evolution of the breakup from the liquid thread to individual droplets. Here, $R_0 = 6$, $A = -50$, $L = 8\pi R_0$.

parameter A from -90 to -40 to represent different fluids. Since we used the Lucy kernel to compute the local densities in all of simulations in this chapter, the fluid properties are slightly different than the ones presented in Tab. 2.1, their new values are reproduced in Tab. 3.1. Periodic boundary conditions are applied in every side of the simulation domain.

No external perturbation is introduced in the system and the breakup spontaneously occurs due to the thermal fluctuations modeled as random and dissipative forces in MDPD. Depending on the goal of the simulations, we also changed the length L of the cylinder as a multiple of its circumference to make our results comparable between different initial radii.

A typical simulation trajectory is shown in Fig. 3.3, from the initial configuration until the formation of all the droplets. We see that initially the cylinder is undisturbed and then eventually starts to form asymmetric undulations on its surface that grow with time and lead to pinch-off at different positions and at different moments in time. After the pinch-off, we observe the formation of main and satellite droplets.

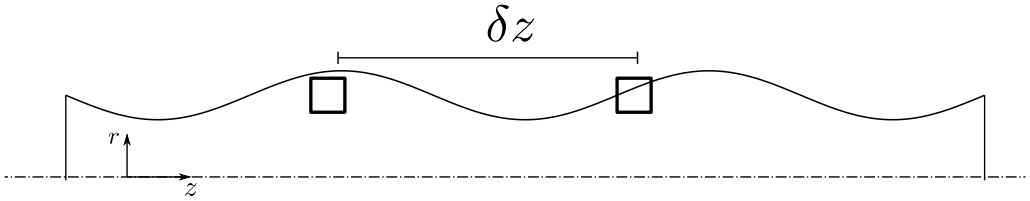

FIGURE 3.4: Representation of two annular bins at a distance δz used to compute the density correlation function in Eq. 3.53. The bin's density is simply the number of particles in the bin divided by the volume of each bin.

3.2.1 Characteristic wavenumber

The characteristic wavenumber χ is equivalent to the most unstable wavelength. To measure this value, we take advantage of the axisymmetric nature of the system and divide the liquid thread in annular bins with the bin size in the radial direction and the bin size in the axial direction equal to unity. Then, we compute density correlations along the z direction as a function of the distance δz between two bins. This process is illustrated in Fig. 3.4. For a fixed radial position, the correlation function is computed as:

$$G(r,\delta z) = \frac{\langle \rho(r,z)\rho(r,z+\delta z)\rangle_{z,T}}{\langle \rho^2(r)\rangle_{z,T}}. \tag{3.53}$$

The density is simply the number of particles in the bin divided by the volume of each bin. Furthermore, averaging happens along the z axis for $\delta z < L/2$ because of the periodic boundary conditions [77]. The subscript T indicates the ensemble average of many independent simulations at the same temperature ($k_b T = 1$). All our results were obtained by averaging 20 independent trajectories for the same set of parameters, changing only the random number generator seed on the random force. This is done to ensure statistically meaningful results.

We perform the ensemble averages at the last time step prior to the first breakup occurring, i.e. the breakup time, t_b, which is different for every simulation. The breakup time is automatically found by doing a binary search over time on each trajectory until we encounter a first time step in which the thread configuration has an empty bin along the axial direction at the radial position $r = 0$. The difference in average breakup time for different A is shown in Fig. 3.5 and as we make the attractive parameter more negative, which increases the attraction between MDPD particles, we observe that the liquid thread takes longer to break.

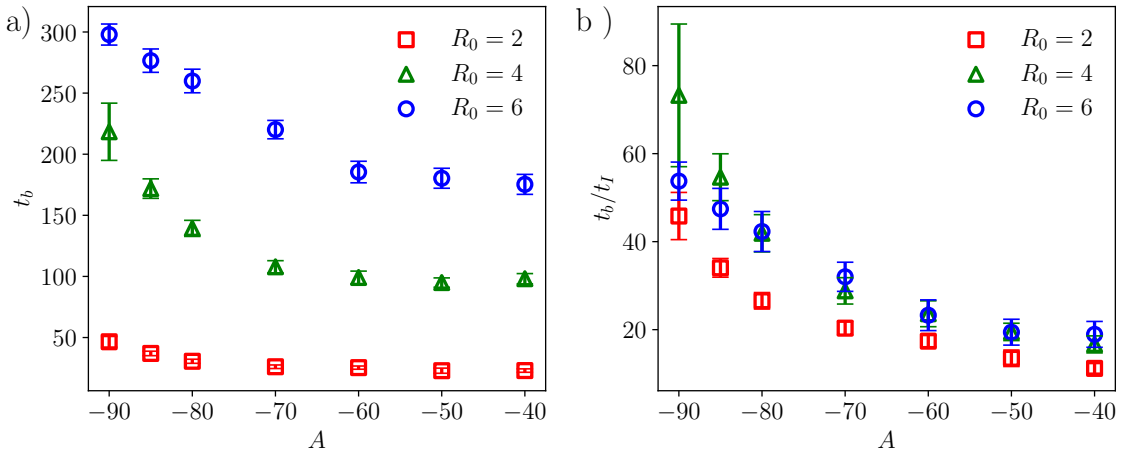

FIGURE 3.5: a) Dependence of the breakup time t_b on the attractive parameter A for threads with different initial radius R_0. Adapted from Carnevale et al. [67] with permission by AIP Publishing. b) Same dependence but with the breakup time normalized by the inertial time scale t_I. Time is in MDPD units.

After calculating the density correlations at the breakup time, we analyze the perturbation modes from a Fourier transform of the function. Figure 3.6 a) shows an example of such measurements on a thread with $R_0 = 6$ and $A = -50$, or equivalently, Oh $= 0.266$. The characteristic wavenumber is obtained by carrying out a Gaussian fit around the peak in the Fourier spectrum. Moreover, reduced wavenumbers are related to the Fourier frequency q as $\chi = 2\pi R_0 q$. The discrete Fourier transform (DFT) was computed by using the Scipy package [78]. For a sequence with N points the DFT is defined as:

$$\hat{G}(r,q) = \sum_{n=0}^{N-1} e^{-2\pi i \frac{qn}{N}} G(r,\delta z_n). \tag{3.54}$$

Finite-size effects were investigated by changing the length of the liquid thread. The results in Fig. 3.6 b) show that by increasing L we are able to obtain better statistics but the characteristic wavenumber stays reasonably well within the theoretical prediction $\chi = 0.565$ for Oh $= 0.266$ (Eq. 3.51). We henceforth only use long threads in the simulations to obtain the highest possible accuracy on the characteristic wavelength through the Fourier transform. Moreover, a larger number of droplets formed in the case of longer threads allows for better statistics on the post breakup analysis.

Repeating this procedure for the different sets of parameters used in our simulations, we can obtain a relation between the characteristic wavenumber and the Ohnesorge number. This dependence is presented in Fig. 3.7 and compared to

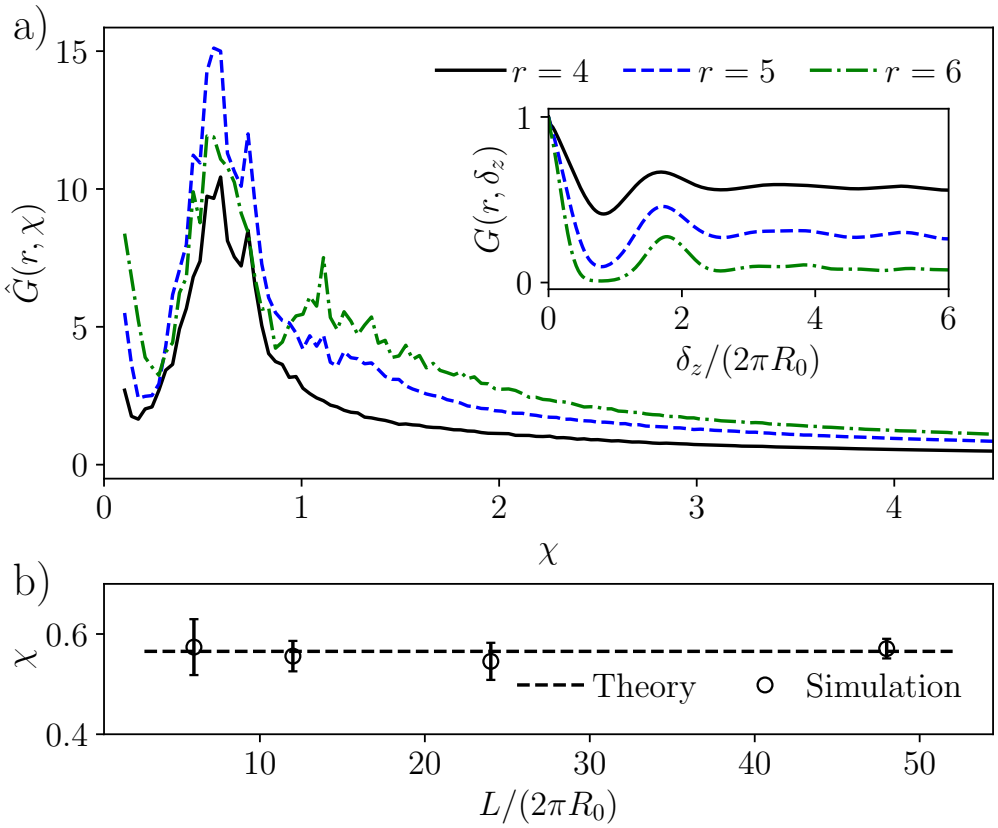

FIGURE 3.6: a) Fourier transform, $\hat{G}(r,\chi)$, of the correlation of the density fluctuations, $G(r,\delta z)$ (inset), at various radial distances, r, from the thread axis, as indicated. Example for Oh = 0.266; b) The characteristic wavelength for threads of different lengths, L. The dashed line indicates the theoretical prediction, $\chi = 0.565$, as obtained from Eq. 3.51. Adapted from Carnevale et al. [67] with permission by AIP Publishing.

Eq. 3.51. The results show that the theoretical prediction is generally valid for the range of parameters tested, and that the stochastic nature of the thermal fluctuation driven breakup does not seem to affect the wavenumber. It is worth noting that by changing the initial size of our system we are increasing the Th number so the relative importance of the fluctuations is higher.

3.2.2 Breakup dynamics and droplet-size distribution

Having characterized the most unstable wavelengths for various fluid systems, we now turn our focus on the post breakup analysis. The droplet-size distribution is an important quantity to be measured as it relates to the final quality in some applications, such as monodispersity in sprays or good resolution in inkjet printing. In view of the stochastic nature of the breakup we expect that the number of droplets changes with time. To investigate the droplets formation, we use

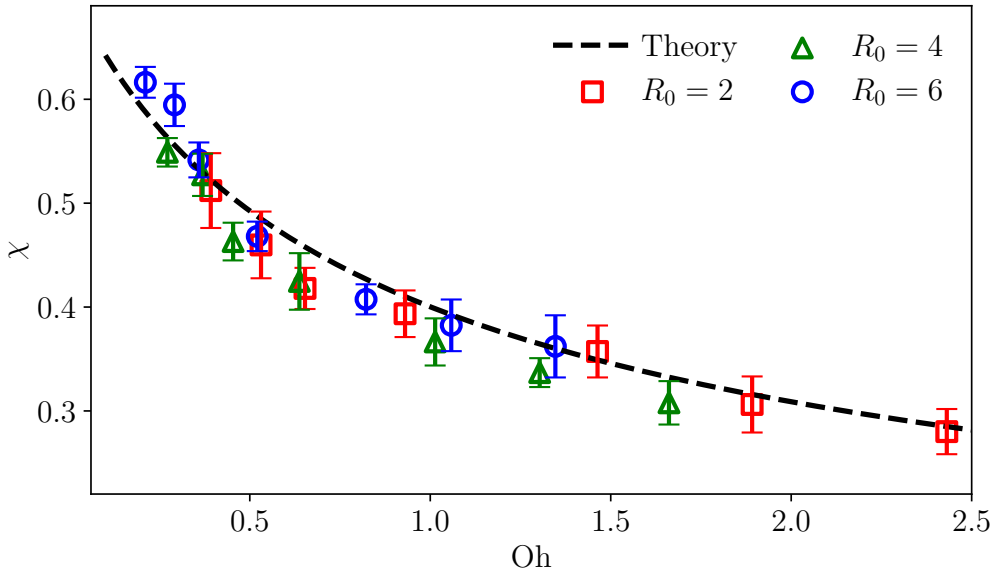

FIGURE 3.7: Characteristic wavenumber, χ, *versus* Oh number. The dashed line shows the theoretical prediction (Eq. 3.51). Adapted from Carnevale et al. [67] with permission by AIP Publishing.

Ovito's python API package [63] to perform a cluster analysis over time. This is done by grouping particles that are within a certain threshold distance from each other. The set of all particles that can be connected through a continuous path along its neighbors that are at a distance smaller than the cutoff $r_{cut} = 0.8$ were considered to be in the same cluster. However, a single cluster is not necessarily a droplet as it could still be an elongated part of the liquid thread that has not been broken yet. To help distinguish which clusters are droplets and to measure their sizes, one can calculate the gyration tensor for each cluster as:

$$S_{mn} = \frac{1}{2N^2} \sum_{i=1}^{N} \sum_{j=1}^{N} (r_{i,m} - r_{j,m})(r_{i,j} - r_{j,n}), \tag{3.55}$$

where $r_{i,m}$ is the m-th coordinate of the i-th particle and N is the total number of particles in the cluster. The gyration tensor is symmetric and can be described by a diagonal tensor with elements called the principal moments that are ordered as $\lambda_1^2 < \lambda_2^2 < \lambda_3^2$. We use a descriptor called relative shape anisotropy [79] that is calculated from the gyration tensor by the formula:

$$\kappa^2 = \frac{3}{2} \frac{\lambda_1^4 + \lambda_2^4 + \lambda_3^4}{\left(\lambda_1^2 + \lambda_2^2 + \lambda_3^2\right)^2} - \frac{1}{2}. \tag{3.56}$$

Values of relative shape anisotropy closer to zero indicate that a cluster has a stronger spherical symmetry while values closer to one rather indicate that all points lie along a line. Here, we required our clusters to satisfy the criterion that $\kappa^2 < 0.2$ to be considered droplets.

The size of each droplet is obtained from the radius of gyration, given by:

$$R_g = \sqrt{\lambda_1^2 + \lambda_2^2 + \lambda_3^2}, \tag{3.57}$$

which is related to the radius of a sphere by:

$$R_D^2 = \frac{5}{3} R_g^2. \tag{3.58}$$

The left panel on Fig 3.8 a) and b) display the evolution of the average number of clusters, normalized by the circumference of the liquid thread, for different values of the parameter A, with an initial thread radius $R_0 = 6$. The plots begin at the breakup time, as no droplets are formed before this point. It is apparent that the liquid threads require some time to reach a maximum number of droplets, after which the number of droplets decreases. This reduction is due to subsequent coalescence of droplets that move close together.

In Fig. 3.8 b), which refers to a system with a higher attraction parameter (Ohnesorge number Oh= 1.137), the system takes longer to reach its maximum droplet count. Furthermore, this system produces fewer satellite droplets compared to the system in Fig. 3.8 a), where Oh= 0.199.

The right panels in Fig 3.8 a) and b) show the droplet size distribution in the form of density histograms. These histograms are taken at a time step corresponding to the maximum number of droplets, i.e., the peak point on the left panels. The droplet size distributions are bimodal, reflecting the distinction between satellite droplets and main droplets, both of which are marked on the plots. In Fig. 3.8 b) the size distribution is broader, with its peak shifted to the right compared to Fig. 3.8 a), indicating that the higher Ohnesorge number system produces larger droplets.

A similar trend is observed for liquid threads with smaller initial radii, as shown in Fig. 3.9. However, in these cases, even fewer satellite droplets are produced compared to the systems with larger initial radii. Given that thermal fluctuations become more significant in smaller systems, it is likely that they play a role in satellite droplet formation, as we will see later.

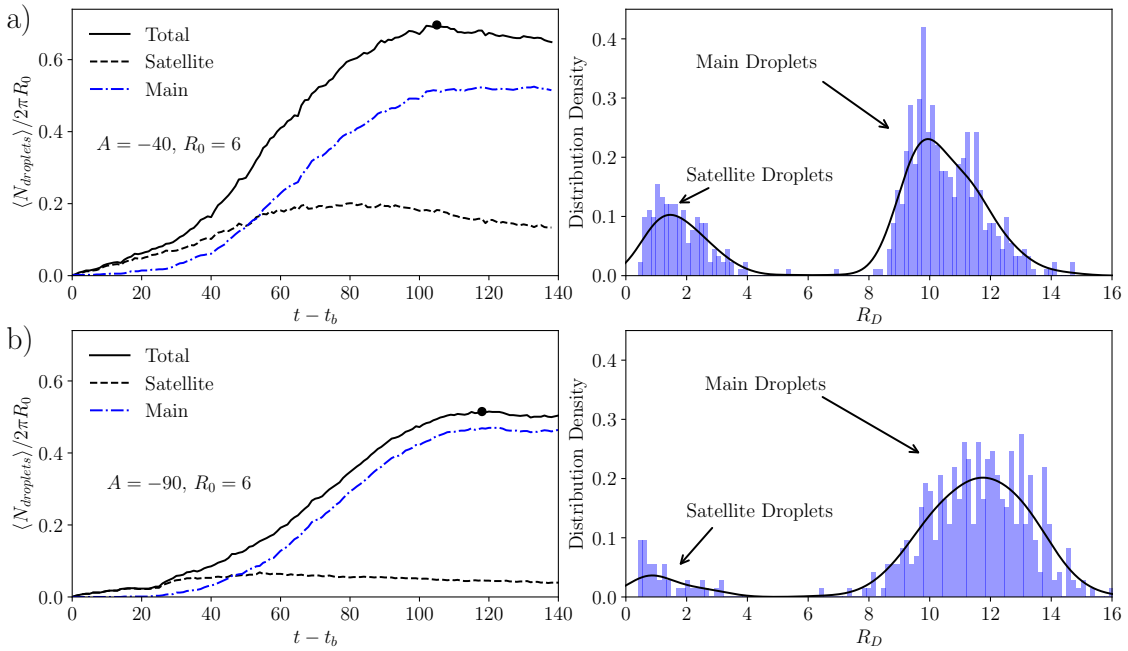

FIGURE 3.8: The left panels illustrate the evolution of the linear number density of droplets *versus* time (t_b is the time of the first breakup event) for the main and satellite droplets, as well the total sum of the two, as indicated, for a liquid with a) Oh = 0.199 and b) Oh = 1.137. The right panels show the distribution of the size of droplets (calculated from the radius of gyration, R_D) at the time of maximum droplet count, indicated by the black dot in the left panels. The two distinct populations are the satellite (left peak at smaller R_D) and the main (right peak at larger R_D) droplets. Both cases had initial cylinder radius $R_0 = 6$. Reprinted from Carnevale et al. [67] with permission by AIP Publishing.

To further explore the relationship between droplet size and the characteristic wavenumber, we assume that the peak of the solid-line fit on the size distributions in Figs. 3.8, 3.9 represents the expected size of the main droplets. We plot these droplet sizes in Fig. 3.10, normalized by the initial thread radius, as a function of the characteristic wavenumber χ.

A theoretical estimate of the sizes of droplets can be obtained by assuming that a cylindrical thread with the same initial radius R_0 and with a length equal to the characteristic wavelength $\lambda = 2\pi R_0/\chi$ will transform into a single spherical droplet with radius R_D [20]. The final expression is obtained by equating the cylinder volume with the sphere volume as a function of the wavenumber χ. The formula is:

$$R_D/R_0 = \sqrt[3]{\frac{3\pi}{2\chi}}. \tag{3.59}$$

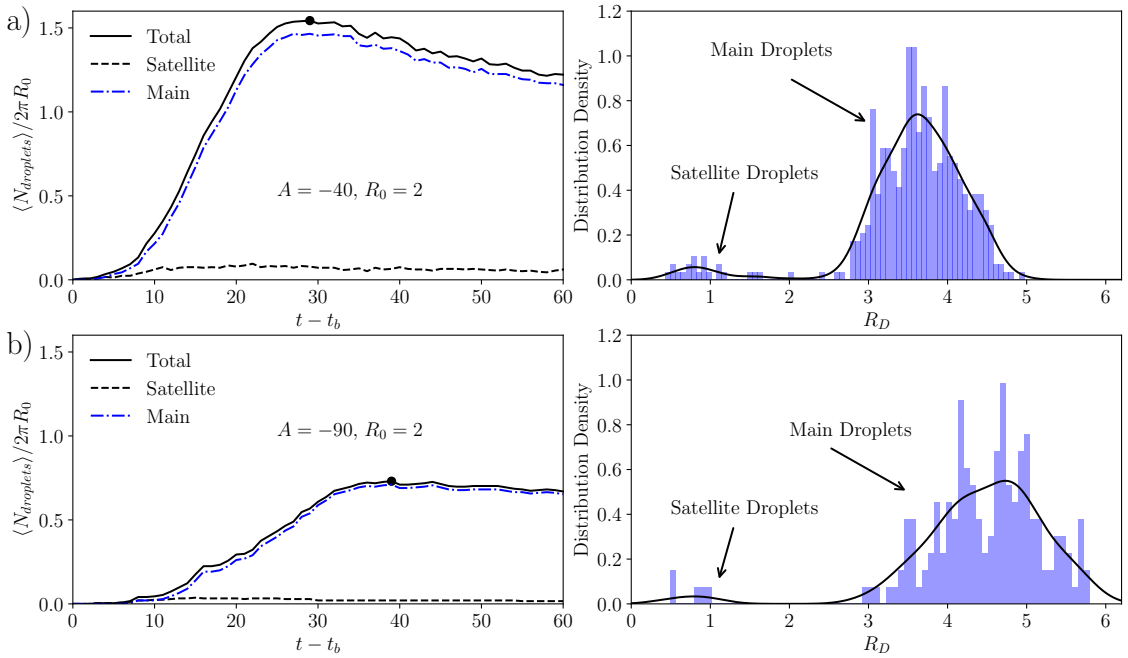

FIGURE 3.9: The left panels illustrate the evolution of the linear number density of droplets *versus* time (t_b is the time of the first breakup event) for the main and satellite droplets, as well the total sum of the two, as indicated, for liquid with a) Oh = 0.428 and b) Oh = 2.43 . The right panels show the distribution of the size of droplets (calculated from the radius of gyration, R_D) at the time of maximum droplet count, indicated by the black dot in the left panels. The two distinct populations are the satellite (left peak at smaller R_D) and the main (right peak at larger R_D) droplets. Both cases had initial cylinder radius $R_0 = 2$.

Figure 3.10 demonstrates that droplet size is indeed dependent on the characteristic wavenumber, with droplet size decreasing as the wavenumber increases. However, the rate of change follows a steeper trend than expected. A power-law fit yields a scaling relationship where the droplet radius scales as $R_D / R_0 \sim \chi^{-0.62}$, in contrast to the theoretically predicted scaling $R_D / R_0 \sim \chi^{-1/3}$. This deviation is attributed to the stochastic nature of the breakup process driven by thermal fluctuations. These fluctuations, introduced as Gaussian noise through the MDPD thermostat, generate multiple perturbation modes during the growth phase of the instability, as shown in the Fourier spectrum in Fig. 3.6 a). This leads to slightly different thinning rates at different pinching points along the liquid thread, some of which end up being suppressed, thus, leading to locally larger droplets.

To elucidate the suppression mechanism, we show the thinning process in more detail for a section of the liquid thread in Fig. 3.11. Focusing on the formation of droplet 3, we observe that the pinching point on its left side initially had a

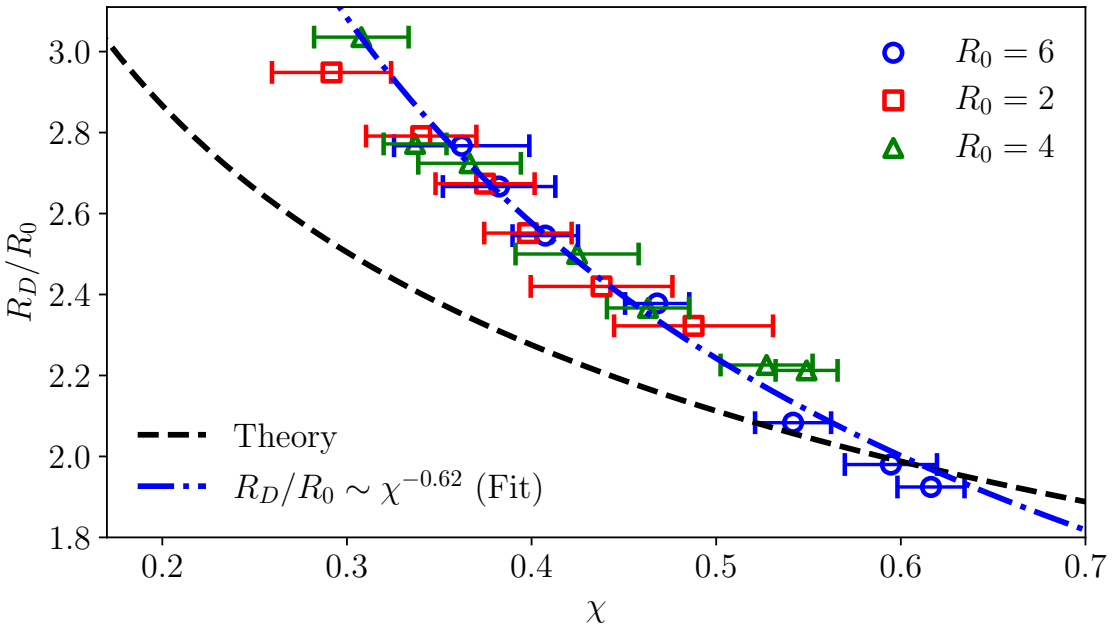

FIGURE 3.10: Dependence of the average expected radius, R_D, of the main droplets *versus* the characteristic wavenumber, χ. The dashed line shows the expected value (Eq. 3.59) based on the volume balance with respect to χ. The blue dashed line shows a power-law fit of the simulation data, i.e., $R_D/R_0 \sim \chi^{-0.62}$. Adapted from Carnevale et al. [67] with permission by AIP Publishing.

wavelength closer to the characteristic wavelength, causing it to pinch-off before the thinning neck on the right side. Once the bulge destined to become droplet 3 detaches from one side, a retracting liquid filament moves toward the bulge. This retraction imparts linear momentum to the droplet, causing it to drift to the right. The liquid filament retraction is indicated in the formation of droplet 1.

In the case of droplet 2, initially two bulges are connected by a thinning neck. However, the thinning necks to the left and right of these bulges pinch-off first, while the central neck continues thinning. As the two bulges retract from both sides, they gain momentum toward each other, as shown by the arrows in the figure. This inward retraction suppresses the thinning of the middle neck, preventing it from pinching off and resulting in the formation of a larger droplet. The same process is observed in the formation of droplet 4. Moreover, droplets 5 and 6 were also formed by two bulges in a similar manner. However, the wavelength that formed the central pinching point was too small and it did not have enough time to grow before it got suppressed. The mechanism behind the formation of a satellie droplet between droplets 5 and 6 will be explained in a later section.

It is important to note that droplets formed from systems with lower χ values exhibit a larger deviation from the theoretical prediction. These cases correspond

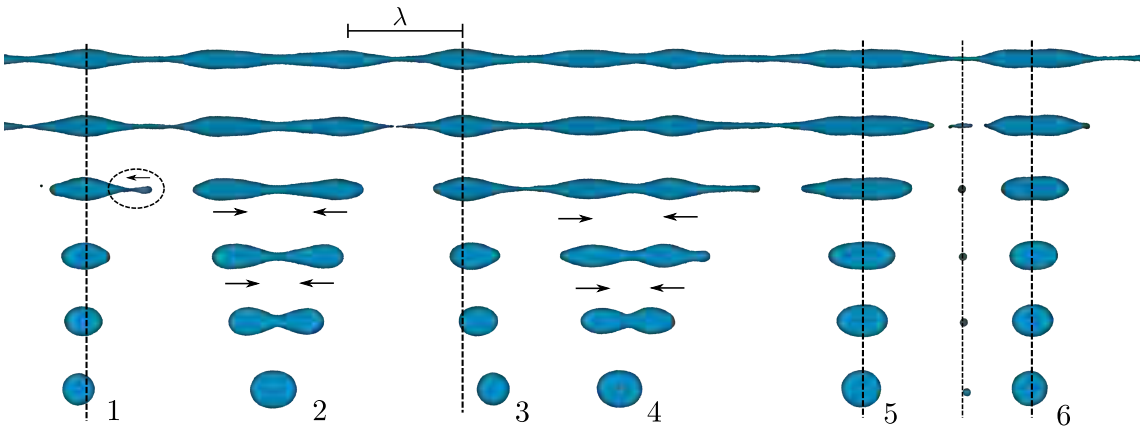

FIGURE 3.11: Time evolution of a breakup simulation showing the mechanism of breakup suppression due to the asymmetry in the pinching events, which can also suppress the formation of satellite droplets, and the mechanism by which droplets acquire lateral momentum that will lead to coalescence later on. Numbers indicate droplets discussed in the text. This simulation corresponds to the case where Oh $= 1.137$ and $R_0 = 6$. Reprinted from Carnevale et al. [67] with permission by AIP Publishing.

to higher Oh values where viscous effects slow down the thinning process, and, thus, have a longer breakup time. This difference in time scale seems to favor the suppression mechanism due to the change in the growth rate of perturbations for higher Oh systems.

3.2.3 Satellite droplets formation

Satellite droplets are typically undesirable in applications like inkjet printing, where their formation is often attributed to nonlinear effects that arise near the pinching point [25]. As mentioned in the previous section, the number of satellite droplets appears to depend on both the initial radius and the attractive parameter A. Variations in these parameters correspond to changes in the non-dimensional Oh and Th numbers.

Petit et al. [7] experimentally demonstrated that thermal fluctuations tend to suppress satellite droplet formation. However, their proposed relationship does not account for the role of viscosity, which also acts to reduce satellite formation.

In Figure 3.12, we plot the ratio of satellite droplets to the total number of droplets as a function of the combined parameter OhTh, with each point representing a different simulation case. We observe that the proportion of satellite droplets follows a power-law trend with an exponent of -0.72 ± 0.04, which indicates that

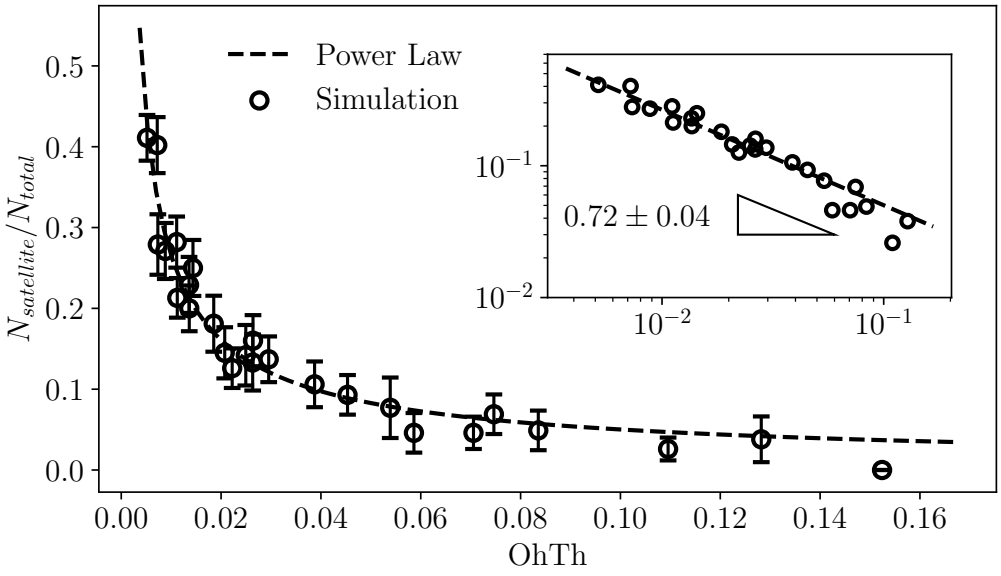

FIGURE 3.12: Dependence of the proportion of satellite droplets, $N_{satellite}$, compared to the total number of droplets N_{total}, *versus* the product of the Ohnesorge (Oh) and thermocapillary numbers (Th). Adapted from Carnevale et al. [67] with permission by AIP Publishing.

both viscosity and thermal fluctuations hinder the formation of satellite droplets. Additionally, no satellite droplets are formed when OhTh equals 0.15. Unfortunately, we are unable to explore higher values of OhTh, as we have reached the limit of the MDPD parameter space for accurately modeling liquids [44].

The decision to use OhTh was inspired by the work of Zhao et al. [76], who suggested that breakup dynamics might depend on both Oh and Th. We also empirically tested various combinations of the form $\mathrm{Oh}^a\mathrm{Th}^b$, where a and b are fitting exponents, and found that the best fit occurred when $a = b = 1$. This form was chosen because similar terms appear in a one- dimensional approximation of the Landau–Lifshitz–Navier–Stokes equation, specifically the stochastic lubrication equation [4, 80].

After identifying a power-law governing the proportion of satellite droplets in a system, we next investigate the dynamics of the thinning neck to understand how these droplets form. A new set of simulations was conducted by setting the liquid thread length equal to one characteristic wavelength, $L = \lambda = 2\pi R_0/\chi$. This approach ensures that only one pinching point develops along the thread. Given the stochastic nature of satellite droplet formation, we conducted simulations for two cases: one with a lower probability of satellite formation (Oh= 0.461) and

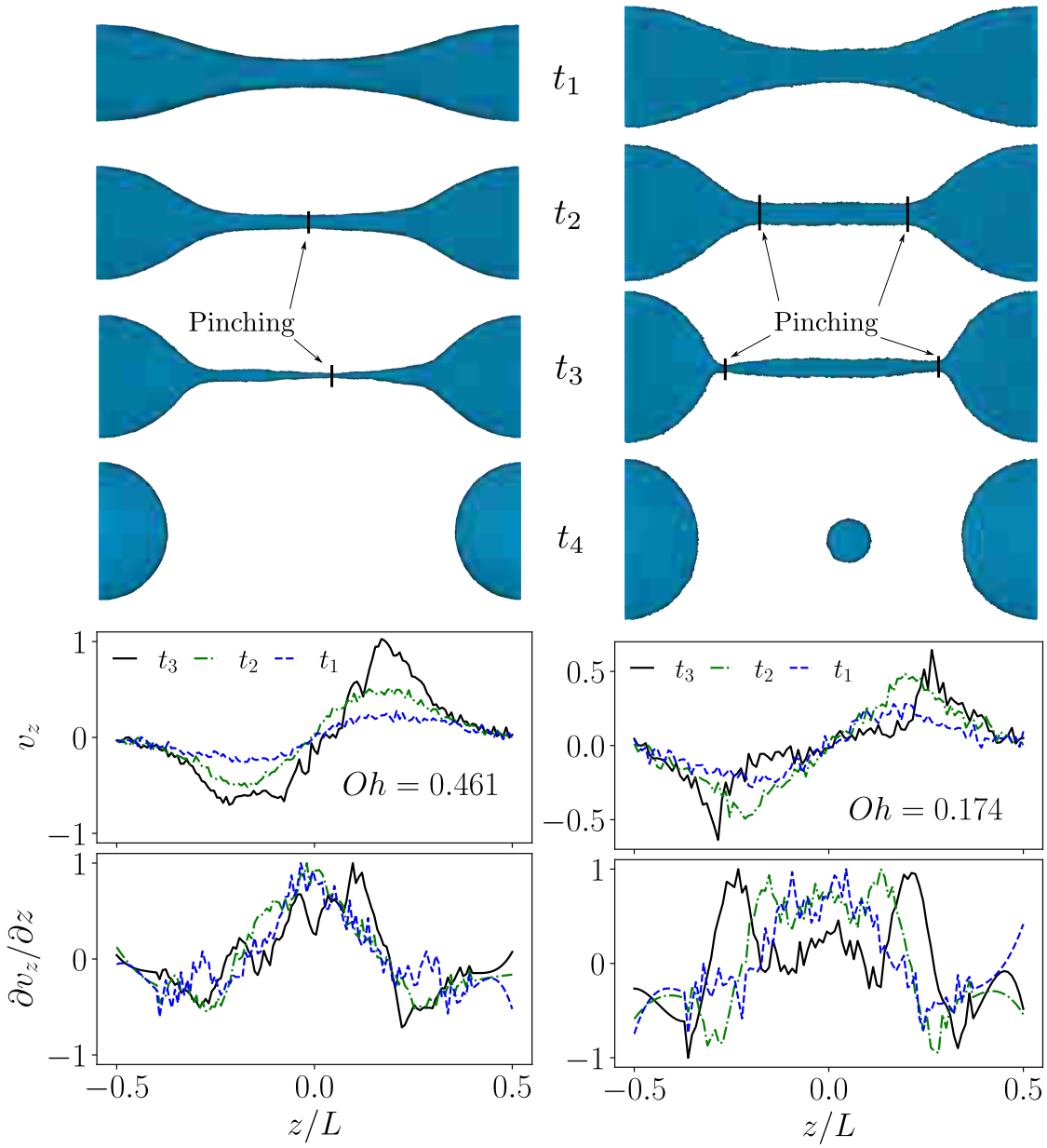

FIGURE 3.13: Breakup of liquid threads with different Oh numbers. The formation of satellite droplets in the case of lower Oh is seen and tracked in the right panel. We observe the advection of the pinching points towards the region that connects the thinning neck to the main droplet. The advection coincides with maxima of the axial velocity gradient. Reprinted from Carnevale et al. [67] with permission by AIP Publishing.

one with a higher probability (Oh= 0.174), minimizing the need for multiple simulations.

Due to the symmetry of the system, we focus on the axial velocity, v_z, to characterize the flow field within the thinning neck [81–83]. The velocity was measured as the average of particle velocities in defined spatial bins along the axial direction at

a radial position of $r = 0$. Furthermore, to reduce noise, the results were averaged over four consecutive time steps. While averaging over more steps could further reduce noise, doing so would blur the results due to the system's time-dependent changes.

The velocity fields and corresponding simulation snapshots are presented in Fig. 3.13. The left panels show a scenario where no satellite droplet forms, while the right panels depict a case where a satellite droplet does form. As shown in Fig. 3.13, satellite droplets emerge when two pinching points develop in the thinning neck, separating it from the main droplets on either side. These pinching points coincide with maxima in the velocity gradient $\partial v_z/\partial z$. During satellite droplet formation, these maxima shift away from the center of the thinning neck, consistent with previous studies [27, 84]. Viscous effects counteract the movement of the pinching points, because viscosity resists to rapid changes in the flow field, particularly in regions of high velocity gradients. In the thinning neck, viscosity acts to dampen the deformation, which slows down the neck's thinning process and resists the advection of the pinching points.

3.3 Conclusions

To conclude this chapter, we have presented a detailed investigation into the Rayleigh–Plateau instability, focusing on the breakup of liquid threads and the formation of droplets, with particular emphasis on the role of thermal fluctuations and viscous effects in determining droplet dynamics. Our study utilized particle-based mesoscale simulations to provide precise values for key parameters, such as the characteristic wavenumber, which directly influences the stability of liquid threads and their subsequent fragmentation.

By exploring various fluid properties characterized by different Ohnesorge numbers, we confirmed that the dependence of the characteristic wavenumber on the Ohnesorge number aligns well with theoretical predictions from stability analysis. Moreover, the Oh numbers utilized are within the range of applications in inkjet printing [17]. These findings validate the use of MDPD as a robust model for simulating the breakup of liquid threads, capturing both macroscopic fluid behavior and the molecular- scale interactions driving the process.

One of the key outcomes of this study is the identification of a clear power-law relationship between the number of satellite droplets and the combined Ohnesorge and Thermocapillary (OhTh) numbers. The exponent derived from this relationship suggests that viscosity and thermal fluctuations play a significant

role in suppressing satellite droplet formation, with higher viscosity fluids showing fewer satellite droplets due to the dampening effect of viscous forces on the thinning neck dynamics.

In addition, our investigation into the formation of main droplets revealed that the average droplet size is closely tied to the characteristic wavelength of the breakup process. However, we also observed deviations from the expected scaling law at higher Ohnesorge numbers. These deviations are attributed to the asynchronous breakup events and the increased timescales associated with viscous fluids, which suppress the formation of pinch points and lead to larger main droplets.

Furthermore, our analysis of the velocity fields within the thinning neck during the breakup process provided an insight into the mechanisms behind satellite droplet formation. We found that satellite droplets form when two strong pinching points, associated with peaks in the velocity gradient, move towards the ends of the thinning neck. This prevents the neck from merging with the main droplets, resulting in the creation of a satellite droplet. In contrast, when viscous effects are strong enough to slow the movement of these pinching points, satellite droplets are less likely to form.

In conclusion, this chapter has provided a comprehensive examination of the Rayleigh–Plateau instability, highlighting the critical factors that govern the breakup of liquid threads and the formation of droplets for different liquids. Not only the insights gained from our simulations validate theoretical predictions, but, also, extend our understanding of the interplay between viscosity, thermal fluctuations, and fluid dynamics in the breakup process. These findings have important implications for applications such as inkjet printing and spray formation, where controlling droplet size and minimizing satellite droplet formation are crucial. Future research can build on these results by exploring more complex fluids and incorporating additional factors, such as surfactants and external forces, into the MDPD framework.

Chapter 4

Surfactant Laden Liquid Thread Breakup

In the previous chapter, we examined the Rayleigh–Plateau instability driven by thermal fluctuations in pure liquids with varying properties, focusing on the mechanisms of droplet formation. Many industrial applications that involve, or are influenced by, droplet production from liquid jets rely on the addition of various chemicals to tailor fluid properties. Among those, surfactants are commonly employed. Surfactants are amphiphilic molecules characterized by hydrophobic chemical groups on one side and hydrophilic groups on the other. This dual nature causes them to adsorb at liquid interfaces, where their primary impact is to reduce surface tension. Since the Rayleigh–Plateau instability is fundamentally governed by surface tension, the presence of surfactants is expected to significantly alter the breakup process.

Current research highlights two primary ways in which surfactants affect the thinning dynamics of liquid threads. First, during the thinning process, surfactants are advected away from the pinching point, creating a surface tension gradient due to the concentration gradient. This induces Marangoni stresses, which slow down the thinning process and delay breakup [33]. However, if the system exceeds the saturation surface concentration and surfactant surplus is present in the bulk liquid, adsorption dynamics play a crucial role. When the adsorption time is much faster than advection, the surfactant concentration at the interface remains constant. Nevertheless, the breakup dynamics differ from those of pure liquids due to surface rheological effects [34, 36].

This chapter will focus on understanding the behaviour of surfactant molecules during the breakup of liquid threads induced by the Rayleigh–Plateau instability. It begins with the description and MDPD parametrization of the surfactant model tailored for a water–air interface. Next, the key properties of the surfactant

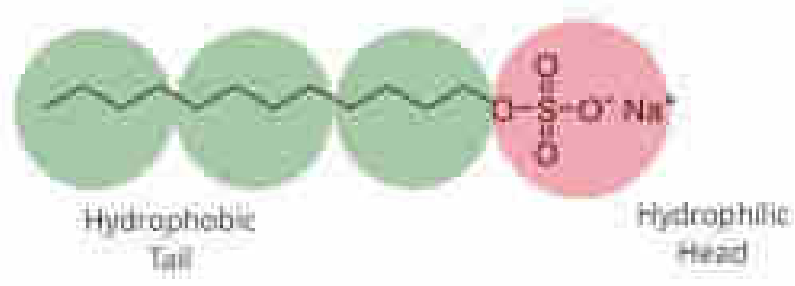

FIGURE 4.1: Schematic representation of the coarse-grained HT_3 surfactant model (see text for details)[86]. Reprinted from Carnevale et al. [85] with permission by AIP Publishing.

are characterized, including surface tension and critical micelle concentration. Finally, the influence of surfactants on the thinning process is analyzed through measurements of characteristic wavelengths, radius thinning regimes, and surfactant concentration distributions at the interface near the pinching point. The findings presented in this chapter are primarily based on one of our publications (see [85]).

4.1 Surfactant model and parametrization

4.1.1 Model

We have chosen to use sodium dodecyl sulfate (SDS) as our surfactant due to its ample use in industrial applications. Following the literature on coarse-grained models of SDS, we decided to represent it by combining two kinds of particles. The hydrophilic head group is modeled as a single 'H'-type particle. The alkane hydrophobic tail is modeled by three 'T'-type particles. Figure 4.1 shows the coarse grained representation of the HT_3 model molecule. To model the bonds between particles and the angles in the molecular structure we use the harmonic potentials:

$$E_{bond} = k\left(r_{ij} - r_0\right)^2, \tag{4.1}$$

$$E_{angle} = k_A\left(\theta_{ijk} - \theta_0\right)^2, \tag{4.2}$$

where k and k_A are constants, r_0 is the equilibrium bond length, and θ_0 the equilibrium angle.

To simulate a physical system with SDS at the water–air interface we use a typical three-to-one mapping to model the liquid phase. This means that one 'W'-type particle represents three water molecules.

4.1.2 Parametrization

The parameters used in our simulations were found in the literature of MDPD models for surfactants and in this section we describe the procedure that is typically utilized [86].

To parametrize the interactions between the different types of particles, we begin by mapping a pure liquid system, where the self-interaction $A_{WW} = -40$, to real water properties [45, 48]. This leads to the conversion between MDPD and real units presented in Tab. 4.1.

With the water self-interactions and the units mapping set, simulations with only 'T'-type particles were done and the self-interactions A_{TT} were systematically varied until the system reproduced the surface tension of hexadecane, which is a hydrophobic alkane that can be modeled by bonded 'T'-type particles. Afterwards, a system with hexadecane and water was created to tune the cross interaction A_{WT} to reproduce their real interfacial tension. Lastly, the 'H'-type particle self and cross interactions were empirically defined by qualitatively testing the SDS molecule behavior at the water–hexadecane interface. The interactions are presented in Tab. 4.2

The bond and angle potentials parameters were also obtained from the literature. We adopted the values $r_0 = 0.45$, $k = 400$ of Ref. [87], while the same angle potential parameters[86] were kept, namely, $\theta_0 = 160°$, $k_A = 100$.

TABLE 4.1: Conversion between MDPD and real units. The scaling is done by matching surface tension and density of water to values measured from MDPD simulations using $A = -40$ and $B = 25$. The coarse-graining level is defined so that one MDPD particle represents three water molecules.

Parameter	MDPD value	Real value
Particle	1	3 H_2O
r_c	1	8.17 Å
ρ	6.05	997 kg/m^3
γ	7.62	72 mN/m

4.2 Surfactant properties

We have extensively characterized different properties of our surfactant model through various simulations of water–SDS–air interfaces. Our primary goal was to identify the change in surface tension with the increase in surfactant concentration. Furthermore, we measure interfacial thickness, density profiles, and surface excess concentration. To report our results, we have chosen to express three distinct types of concentrations, all in terms of the free surface area. The total initial concentration, C, is the ratio between the total number of surfactant molecules, N_t, divided by the surface area A_s, thus, $C = N_t / A_s$. The surface excess concentration, Γ, depends only on the number of SDS molecules that are adsorbed at the interface, so $\Gamma = N_s / A_s$. Finally, the bulk concentration $C_b = N_b / A_s$ depends on the molecules in the bulk phase so that we have $N_t = N_b + N_s$. The surface area was chosen to compute the concentration, because the interface saturation becomes more evident and different simulations are initialized with a specified number of surfactants already on the free surface.

To obtain measurements, we initialized a system with a cubic region of water in the middle of the simulation domain with lateral size $h = 20$. The lower and upper periodic boundaries are set at the coordinates -10, 10 in the x and y directions, and at -35, 35 in the z direction, which is normal to the interface. This defined our simulation box with dimensions $L_x = L_y = 20$ and $L_z = 70$. Afterwards, the same number of surfactant molecules at a given initial concentration are placed evenly spaced at both sides of the water region in the normal direction and close to the interface. The system is then run for 10^5 time steps to attain thermodynamic equilibrium. Once equilibrium was reached, we performed an additional 10^6 time steps of simulation to acquire data for calculating the properties of interest. Figure 4.2 shows a typical simulation box, where the water particles have been removed and substituted by the blue shaded area only for easier visualization of bulk surfactants molecules.

TABLE 4.2: MDPD interaction parameters for the HT_3 surfactant model and water. W is the water particle, H the hydrophilic particle, and T the hydrophobic one. The MDPD repulsive parameter is $B = 25$.

A_{ij}	W	H	T
W	-40		
H	-32.18	-19	
T	-27	-5.98	-22

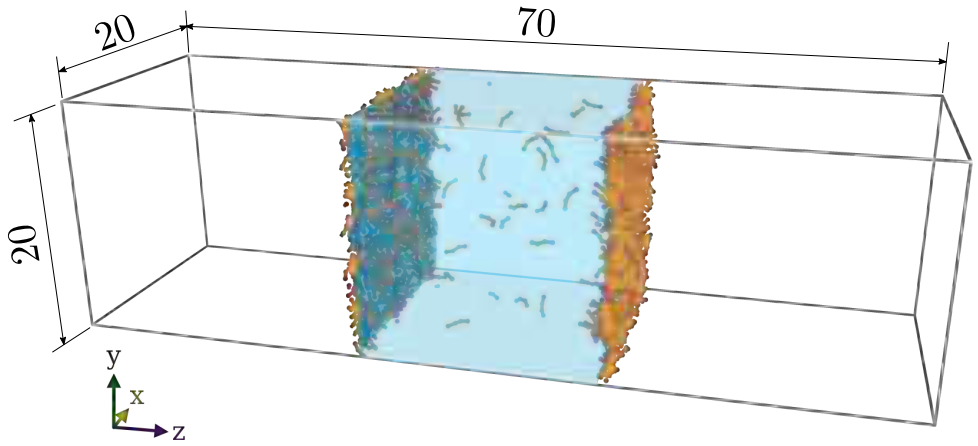

FIGURE 4.2: Example of a system used to measure the surface tension of a liquid slab in the presence of surfactants. The water particles are represented by the transparent blue volume for easier visualization. In this case, the concentration of surfactants is below CMC, and the surfactant molecules are not aggregated in the bulk phase. Reprinted from Carnevale et al. [85] with permission by AIP Publishing.

4.2.1 Surface tension and surfactant concentration

Surface tension from our simulations can be measured from the Kirkwood–Buff method [46]. Similarly to Chapter 2, this is calculated by

$$\gamma = \frac{L_z}{2}\left\langle P_{zz} - \frac{P_{xx}+P_{yy}}{2}\right\rangle, \tag{4.3}$$

where P_{ii}, $i \in \{x,y,z\}$ are the normal components of the pressure tensor. We averaged the results over windows with 10^4 time steps to obtain 100 data samples and estimate the standard deviation of the surface tension value for each concentration simulated.

Our results are presented in Fig. 4.3 for a wide range of concentrations. It is evident that by increasing the concentration of surfactants the surface tension of the water–SDS system continuously decreases until it reaches a plateau. Generally, this minimum value is achieved when the system has reached the critical micelle concentration (CMC), which indicates that the surface is already saturated and new surfactant molecules will go into the bulk phase and form aggregates. This saturation can be confirmed by measuring the surface excess concentration, Γ, also shown in Fig. 4.3. At first, Γ increases linearly with the initial concentration, as is expected, following the line $\Gamma = C$. However, when the surface tension reaches its minimum value, the surface excess concentration also reaches a

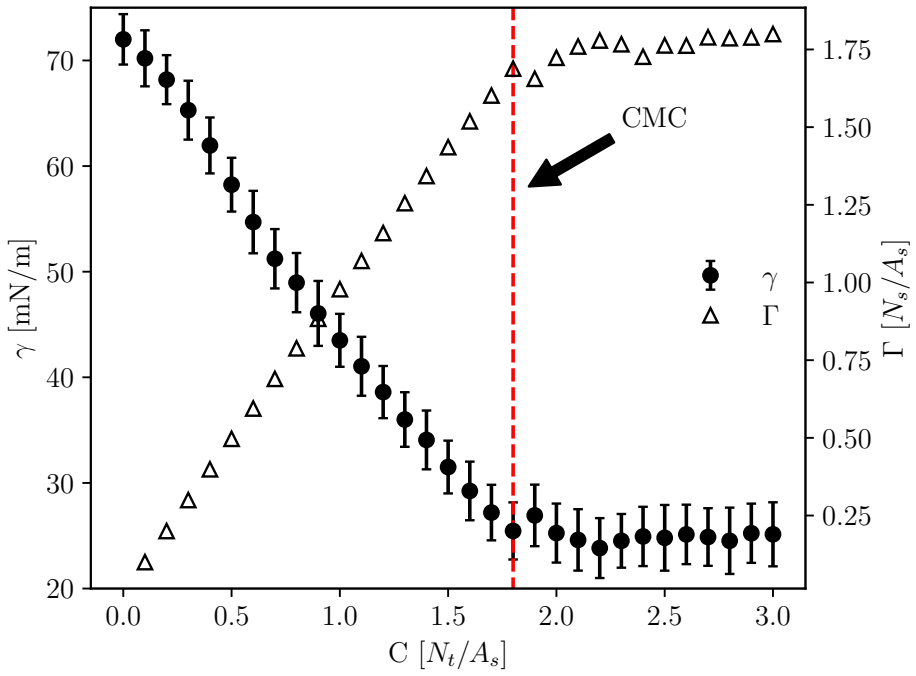

FIGURE 4.3: Dependence of surface tension, γ (circles) and surface excess concentration, Γ (triangles), on the number of surfactant molecules per surface area, C. Both values reach a plateau after crossing the CMC (dashed line) indicating that the interface is fully saturated. Reprinted from Carnevale et al. [85] with permission by AIP Publishing.

plateau, indicating the saturation of the interface with the saturation concentration being $\Gamma_\infty = 1.75$ (MDPD units). A system above the CMC is shown in Fig. 4.4, where micelles are clearly visible in the bulk phase and we also see the presence of free monomer molecules in the liquid. These findings support our MDPD model as it properly represents surfactant behavior.

4.2.2 Interfacial thickness

Another interfacial property that can characterize our surfactant model is the interfacial thickness. As is the case of real fluids, the interfacial region between two phases can be distinguished by the density distribution of its different constituents. Such distribution is depicted in the inset plot of Fig. 4.5 for a simulation with $C = 1.5$. Our fluid is represented by the density of the 'W'-type particles and we can observe that it decreases from the bulk liquid phase value of $\rho = 6.05$ to the vapor phase with $\rho \approx 0$. In the density distribution plot, we can also observe that the hydrophobic tail of the surfactant molecules tend to stay further away from the liquid phase and that the hydrophilic groups tend to stay closer to the

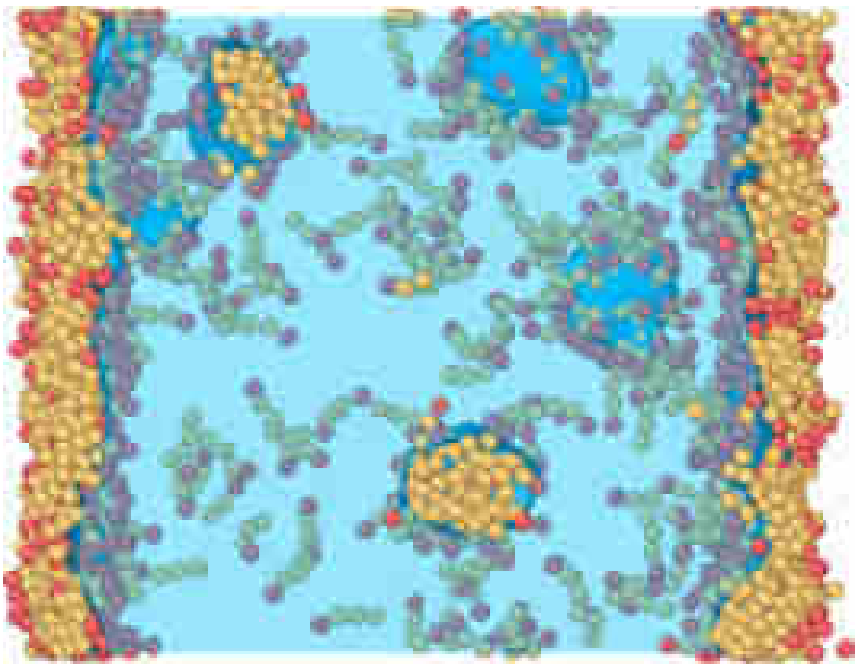

FIGURE 4.4: Simulation of an equilibrated system with a concentration above the CMC. Four micelles are visible together with free monomer molecules in the liquid bulk phase. In this simulation, $C = 2.3$.

liquid. To quantitatively represent the water density distribution, we have fitted our measurements using the hyperbolic tangent function

$$\rho(z) = \frac{\rho_l}{2}\left[1 - \tanh\left(\frac{2(r - z_0)}{\delta}\right)\right], \tag{4.4}$$

where ρ_l represents the bulk density of the liquid phase, z_0 is the Gibbs dividing surface position and δ the thickness of the interface. The Gibbs dividing surface is an idealized surface that assumes a sharp transition with zero thickness between the phases and its position can be calculated by

$$z_0 = \frac{1}{\rho_l}\int_0^\infty z\frac{d\rho}{dz}dz, \tag{4.5}$$

assuming a flat interface and vanishing vapor density. The position of the interface and its thickness are drawn in the inset of Fig.4.5 as the dash-dot and dashed vertical lines, respectively.

Repeating the fitting procedure for all the simulations done, we can investigate the variation the interfacial thickness with the change in concentration. This is presented in the main plot of Fig.4.5, where we can see an initial linear increase

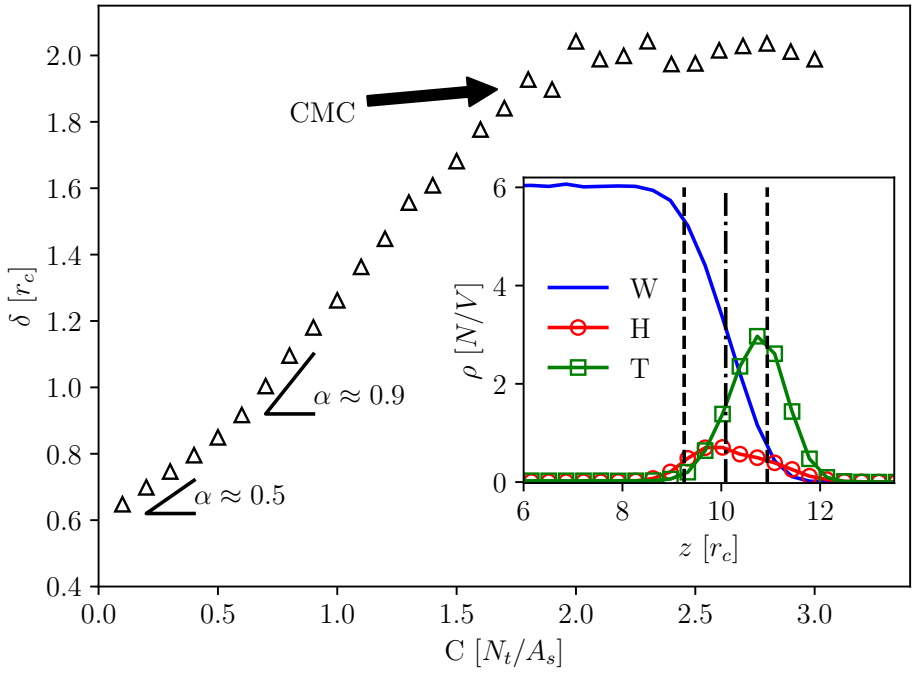

FIGURE 4.5: Change in the interfacial thickness with the increase in the number of surfactant molecules per surface area (α gives the slope.). It remains at a constant value upon reaching the CMC. Inset: example of a density distribution near the interface for a simulation below CMC. The vertical lines indicate the position of the interface and its thickness from a hyperbolic tangent fit (Eq. 4.4). W, H, T are the liquid, head, and tail beads, respectively. Reprinted from Carnevale et al. [85] with permission by AIP Publishing.

with slope $\alpha \approx 0.5$ until the concentration of $C = 0.6$. The thickness continues to increase linearly between $C = 0.6$ and $C = 1.8$, however, with a slope $\alpha \approx 0.9$. The difference in slopes is attributed to a change in orientation of surfactants at the interface. At lower concentrations, the surfactant tails tend to stay parallel to the interface, almost lying just above the surface. With higher concentrations, the molecules rearrange to a more upright position, perpendicular to the interface due to the decrease in available surface area [88]. Systems above the CMC don't experience an increase in the surface excess concentration, thus the number of molecules remains constant at the interface and we see no change in its thickness.

4.3 Breakup simulations

4.3.1 Characteristic wavenumber

We study the liquid thread breakup process in the same manner as it was presented in Chapter 3 by computing the reduced wavenumber $\chi = 2\pi R_0/\lambda$ from a density correlation function along the axial direction [77].

Due to the presence of surfactants in the system, more care is required in constructing the initial configuration of our simulations. We first make a water cylinder with radius $R_0 = 8$ and length $L_z = 24$. Afterwards, we placed the surfactants evenly spaced directly above the surface according to a specified initial concentration. This system is then allowed to run for 2×10^5 time steps to achieve thermodynamic equilibrium. In case of simulations above the CMC this was enough time for the formation of the micelles in the liquid bulk. It it important to note that this initial equilibration procedure was possible because of the short length of the liquid cylinder, which is stable and does not break ($L_z < 2\pi R_0$).

After equilibration, we construct longer liquid threads by replicating the system in the axial direction 48 times. As previously shown in Chapter 3, using longer threads enables more accurate measurements and we also verified that there are no finite-size effects. The, now unstable, system is then allowed to run until the end of the breakup process and all the main and satellite droplets have been formed. To obtain better statistics for our measurements, we performed 20 simulations for each concentration, using different random number seeds for the fluctuation term in the MDPD thermostat, and averaged the results.

A typical simulation trajectory is shown in Fig.4.6 for a concentration $C = 0.5$. We can see the formation of seven droplets and one satellite droplet. We also note that the suppression mechanism described in Chapter 3 is present and it acts more strongly during the formation of droplets. To gain a better understanding of the breakup process, we also show the simulation of a thread four times shorter than the typical ones in Fig. 4.7. This was done only for better clarity, as the longer threads are poorly represented in a figure due to its dimensions. Here, we see the growth of a perturbation with a wavelength $\lambda \approx L/3$, but, due to asynchronous breakup, only one final droplet is formed. It is also possible to note that the surface excess concentration appears to be lower in the region closer to the pinching point.

As the addition of surfactants lowers the surface tension, which acts as the main driving force of the instability, we see a considerable slowing down of the

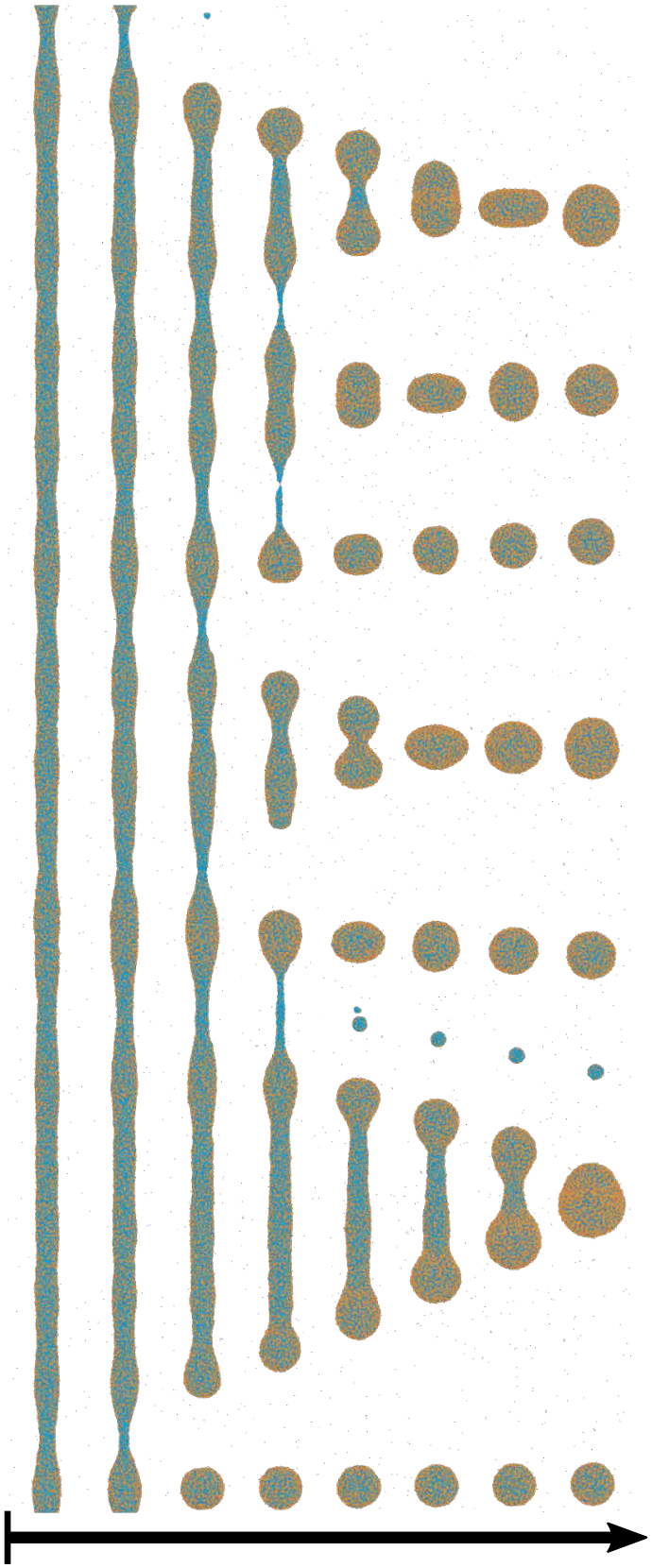

FIGURE 4.6: Simulation trajectory of a typical long thread breakup process. The initial concentration is $C = 0.5$, which is below the CMC.

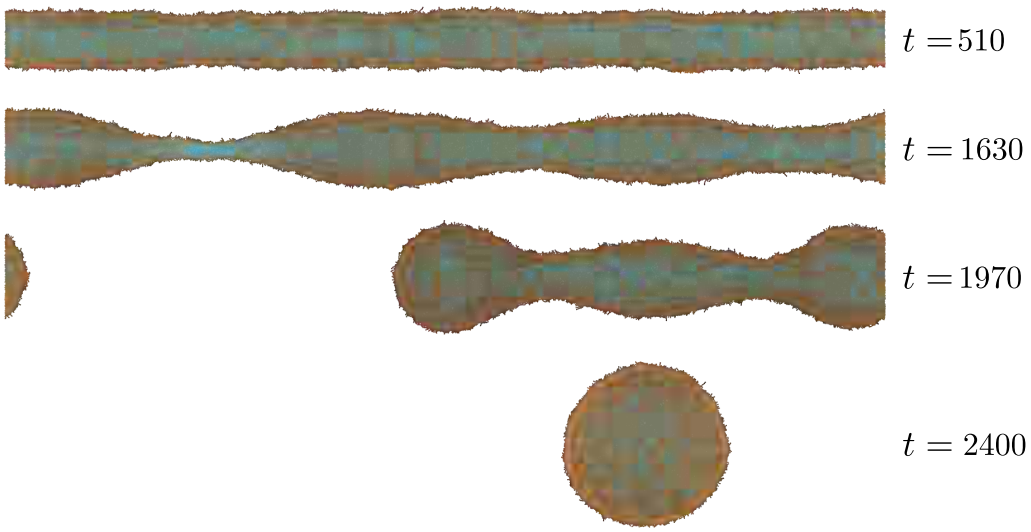

FIGURE 4.7: Simulation snapshots of the breakup process of a short liquid thread. The system develops perturbations that grow with time and lead to the pinch-off and subsequent formation of a droplet. The concentration of surfactant is below CMC in this example. The threads used for statistical analysis were four times longer in the axial direction than the simulation shown here, which was shortened for the sake of clarity. Reprinted from Carnevale et al. [85] with permission by AIP Publishing.

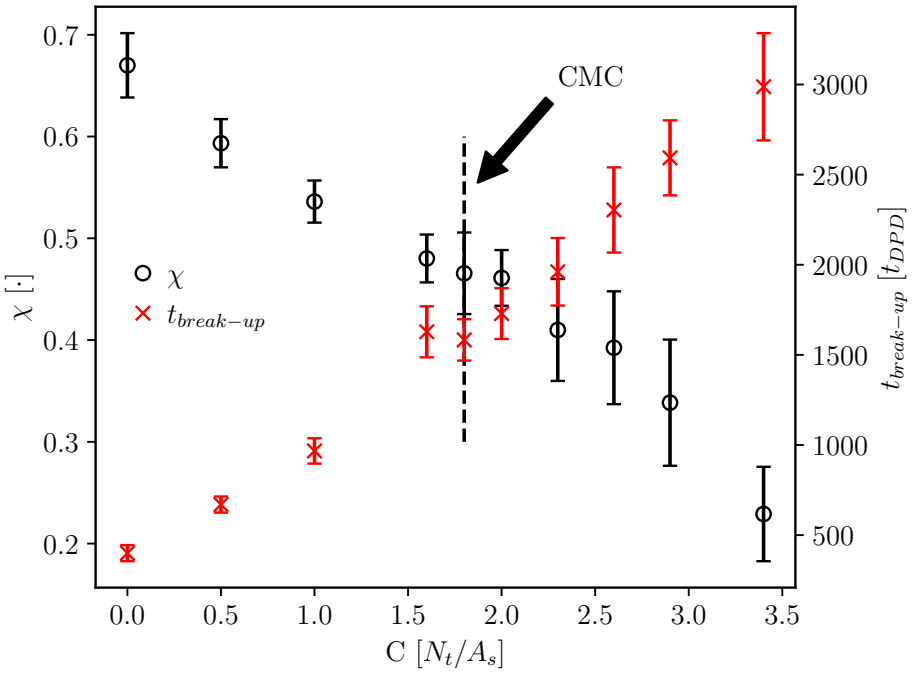

FIGURE 4.8: Change in reduced characteristic wavenumber and time to breakup vs total surfactant concentration (total number of surfactant molecules divided by the initial surface area of the system). Reprinted with permission from Carnevale et al. [85].

breakup process. This is indicated by the linear growth in the time required for the first pinch-off along the thread to occur ($t_{\text{break-up}}$). The results are presented in Fig. 4.8, where we also observe the reduction in the characteristic wavenumber as more surfactants are added to the system. Lower χ values translate to longer wavelengths becoming the more unstable modes that grow along the liquid thread. Interestingly, this decrease is also observed for concentrations above the CMC and cannot be explained by the change in surface tension anymore. Indeed, for this region the surface tension remains constant, but the number of micelles in the bulk liquid increases. For a thinning region to be allowed to break, it first requires that the micelles move away from the pinching point, which apparently vary the viscosity of the fluid. The stronger viscous effects may explain the further slowing down of the dynamics and the lower characteristic wavenumber. We also observe an increase in the standard deviation in our measurements, which can be attributed to the increase of the thermocapillary length consequently intensifying the significance of the fluctuations in the system.

4.3.2 Droplet-size distribution

Following the breakup process, the temporal evolution of both main and satellite droplets was analyzed using cluster analysis conducted with OVITO software [63]. As in Chapter 3, clusters were also defined as groups of particles in proximity within a specified threshold ($r_{ij} \leq 0.8$), and the size of each droplet was determined from the radius of gyration of the spherical clusters.

Our droplet-size measurements are depicted in Fig. 4.9. There is a general increase in the sizes of droplets as the concentration of surfactant increases. This is in line with the expectation that longer wavelengths will form bigger droplets, as less pinching points form. Moreover, there is a slight distinction in the growth trend for systems above the CMC, which could be explained by the slowing down of the breakup process. Slower pinching dynamics favors the suppression mechanism explained in Chapter 3. In contrast, the size of satellite droplets exhibited no statistically significant variation with concentration. Their sizes were consistently measured at $R_s/R_0 = 0.24 \pm 0.03$ across all simulations.

We further investigated the proportion of satellites formed and found a clear reduction in their formation as more surfactants are in the system. This reduction is likely due to the larger thermocapillary length scale, as thermal fluctuations are known to inhibit satellite droplet formation [4, 6, 67]. Above the CMC, this proportion approaches an asymptotic value, as depicted in the inset of Figure 4.9.

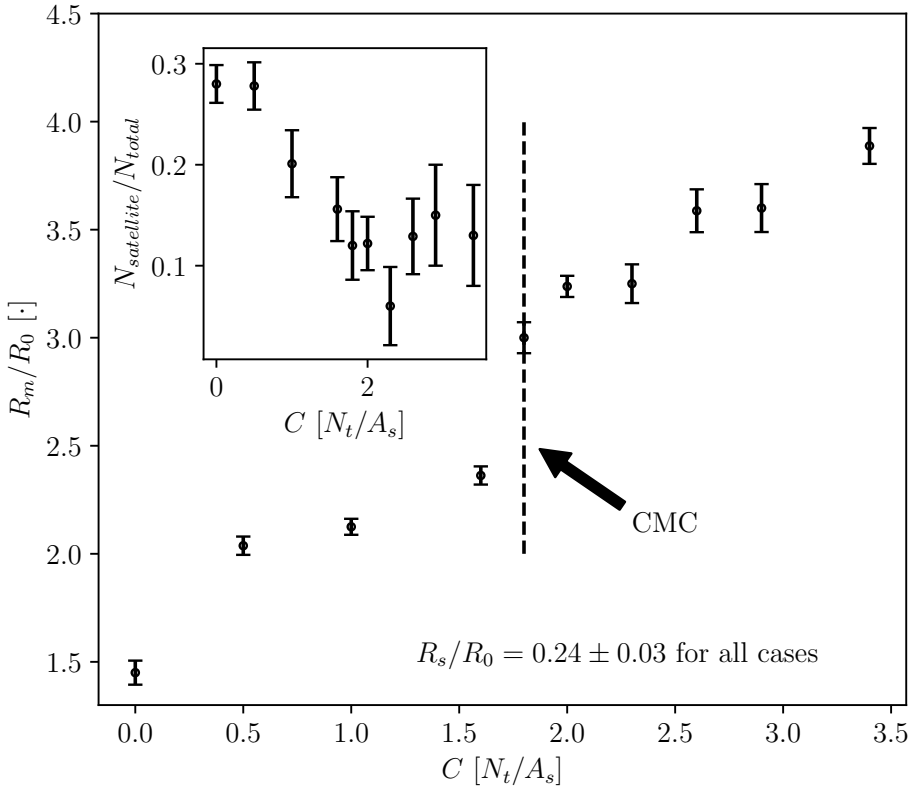

FIGURE 4.9: Size of main droplets, R_m, normalized with the initial thread radius *versus* total surfactant concentration, C. The radius of satellite droplets did not present any statistically significant variation with respect to the change in concentration, and therefore data are not plotted here (see main text for further details). Inset shows the change in the proportion between the number of satellite droplets and the total number of droplets formed. Reprinted from Carnevale et al. [85] with permission by AIP Publishing.

4.3.3 Surfactant distribution at the interface

Understanding how surfactants are distributed along the liquid thread interface is essential for explaining the pinch-off dynamics during breakup. Moreover, any gradient in concentration on the surface will lead to Marangoni stress that hinders the instability [33].

To investigate the transport mechanism of surfactants during the breakup, we conducted a new set of simulations of shorter liquid threads, with a single pinching point. This is achieved by setting the thread's length equal to the most unstable perturbation, i.e. $L_z = 2\pi R_0/\chi$. Statistical robustness was also ensured by running 20 simulations for each concentration investigated. We considered two systems below the CMC with initial concentrations $C = 0.5$, $C = 1.0$, and two systems above the CMC with $C = 2.3$ and $C = 2.9$.

We utilized the software OVITO [63] to analyze our simulations. The first step was to group all the particles into axial bins based on their position. The bin size was chosen empirically and set as $h_{\text{bin}} = 1.2$ to avoid too much noise in the data and still yield meaningful measurements. We identified surface particles with OVITO's alpha-shape method and used their positions to fit circles on each bin. The radii of those circles along the axial direction defined a surface shape profile, $h(z)$. Surfactant molecules were then tagged as being interfacial molecules if they were within a thickness δ from $h(z)$. Otherwise, they were tagged as being in the bulk phase. The number of molecules on the surface N_s and in the bulk N_b are divided by the surface area A_i on each bin to obtain the distribution of surface excess concentration $\Gamma(z)$ and the bulk concentration $C_b(z)$.

Due to the stochastic nature of the breakup in our simulations, the pinching point does not always form in the same position on our computational domain. However, to obtain statistically relevant results, we require a strategy to compute the ensemble averages of our measurements. Therefore, we define the reference position $z = 0$ as being the point where the shape profile has its minimum value and then shift all threads to align with this definition. Moreover, we flip some profiles around the pinching point to preserve large anti-symmetrical effects. The condition for flipping is given by a volumetric balance that leads to [76]:

$$\int_{-L_z/2}^{0} h(z)dz > \int_{0}^{L_z/2} h(z)dz. \tag{4.6}$$

Figure 4.10 presents the average shape profile and surfactant concentration distributions for all simulated cases at the last time step before the breakup occurred. Lines represent the average values and the shaded areas indicate one standard deviation. At low concentrations, the breakup profiles exhibit a prolonged thinning neck with the pinching point located closer to one of the main droplets. Drifting of the pinching point from the center of the thinning neck is more noticeable at the lowest concentration. As the surfactant concentration increases, the breakup profile approaches that of an asymmetrical double cone, becoming almost symmetrical for the highest concentration. The double cone profile is expected when the breakup is dominated by thermal fluctuations [4, 8].

Surfactant molecules are in the bulk phase of our systems with lower initial concentrations (Fig. 4.10 a), b)). This result is expected due to the distance to the CMC. We observe the advection of surfactants away from the pinching point, indicated by the lower surface excess concentration at that point and along the thinning neck. At the same time, we also see an increase in Γ on the main droplets,

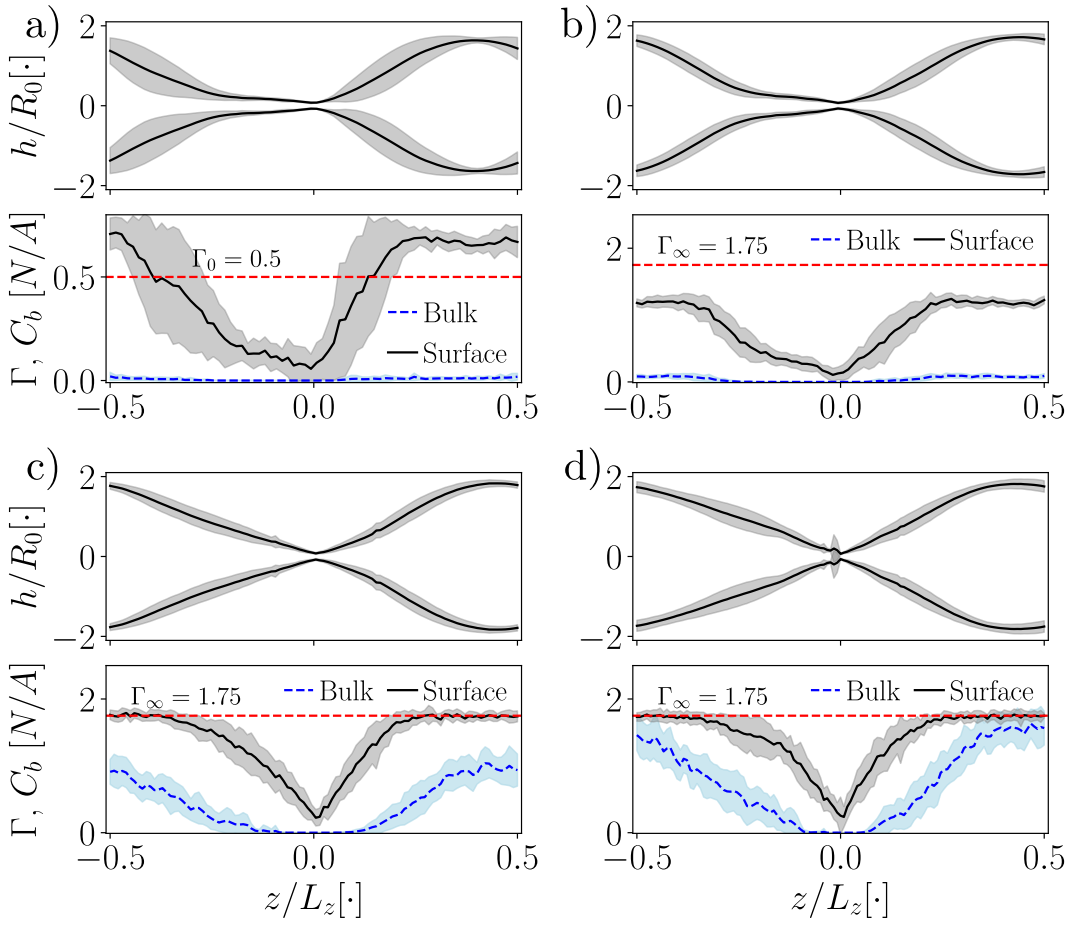

FIGURE 4.10: Profile shapes, h/R_0, and surfactant concentration along the z axis at the surface and in the bulk of the fluid. Lines represent the ensemble average and shaded area is one standard deviation. The averages were obtained at the moment of pinch-off and for two surfactant concentrations below CMC, a) $C = 0.5$ and b) $C = 1.0$, and two above CMC, c) $C = 2.3$ and d) $C = 2.9$. Γ_∞ is the highest surfactant excess concentration at surface saturation. Γ is the surface excess concentration and C_b is the bulk concentration (number of molecules per surface area). Reprinted from Carnevale et al. [85] with permission by AIP Publishing.

which becomes higher than the initial surface excess Γ_0. At concentrations above the CMC, surfactant bulk concentrations become evident. In those cases, we also observe the advection of surfactants from the pinching point toward the main droplets. However, the surface excess concentration never exceeds its saturation value, Γ_∞, in the main droplet regions. To further investigate the surfactant mass transport mechanism, we present the temporal evolution of the concentration distribution for the highest concentration case ($C = 2.9$) in Fig. 4.11. The analysis over time was done by matching all the simulations at the breakup time so that

$t_{\text{break-up}} - t = 0$. The advection of surfactants occurs not only on the surface, but, also, on the bulk phase, which indicates the necessity of micelles to move away from the pinching point. Furthermore, the increase in bulk concentration and the constant surface-excess concentration on the main droplets suggest that the advected surfactants migrate from the interface to the bulk during the breakup process.

4.3.4 Radius scaling

The thinning dynamics of liquid threads were investigated to understand how the minimum neck radius, h_{min}, evolves over time until the pinch-off event. We used the same set of simulations as in the previous section and report the results with respect to their relative time from breakup, $\tau = (t_{\text{break-up}} - t)$.

Theoretically, distinct scaling laws are expected based on the dominant forces at play during the thinning process. When surfactants are advected away from the pinching point, the dynamics are predicted to follow linear scaling, known as the viscous regime, with $h_{min} \sim \tau$ [24, 34]. However, our results in Fig. 4.12 do not exhibit this behavior. When inertial forces are dominant during the breakup, the predicted regime is indicated by the scaling $h_{\text{min}} \sim \tau^{2/3}$ [23]. Another relevant regime happens when the thermal fluctuations become the driving force of the breakup, presenting the scaling $h_{\text{min}} \sim \tau^{0.418}$ [5], which has been experimentally verified [8].

The lowest concentration case presented in Fig. 4.12 follows close to the inertial regime and we do not observe a clear transition or presence of the thermal fluctuation regime. From the literature, MDPD simulations of a liquid without surfactants also have shown a deviation from the thermal fluctuation scaling [80]. As the concentration of surfactants increases, lowering the surface tension, the thinning dynamics is shifted and exhibits a transition between the inertial regime and the thermal fluctuation one. This transition is consistent with predictions obtained by stochastic lubrication theory as surface tension vanishes [76].

All cases also showed a transition to a different behavior when the neck radius approaches the breakup time. A new regime has been previously proposed near the breakup time from MDPD simulations [54]. However, we argue that this is an artifact from the simulation method as the transition occurs when h_{min} falls below the interaction cutoff between particles. At this scale, the local density of each particle near the pinching point starts to decrease, weakening the repulsive forces between particles. This, in turn, increases the relative attraction and slows

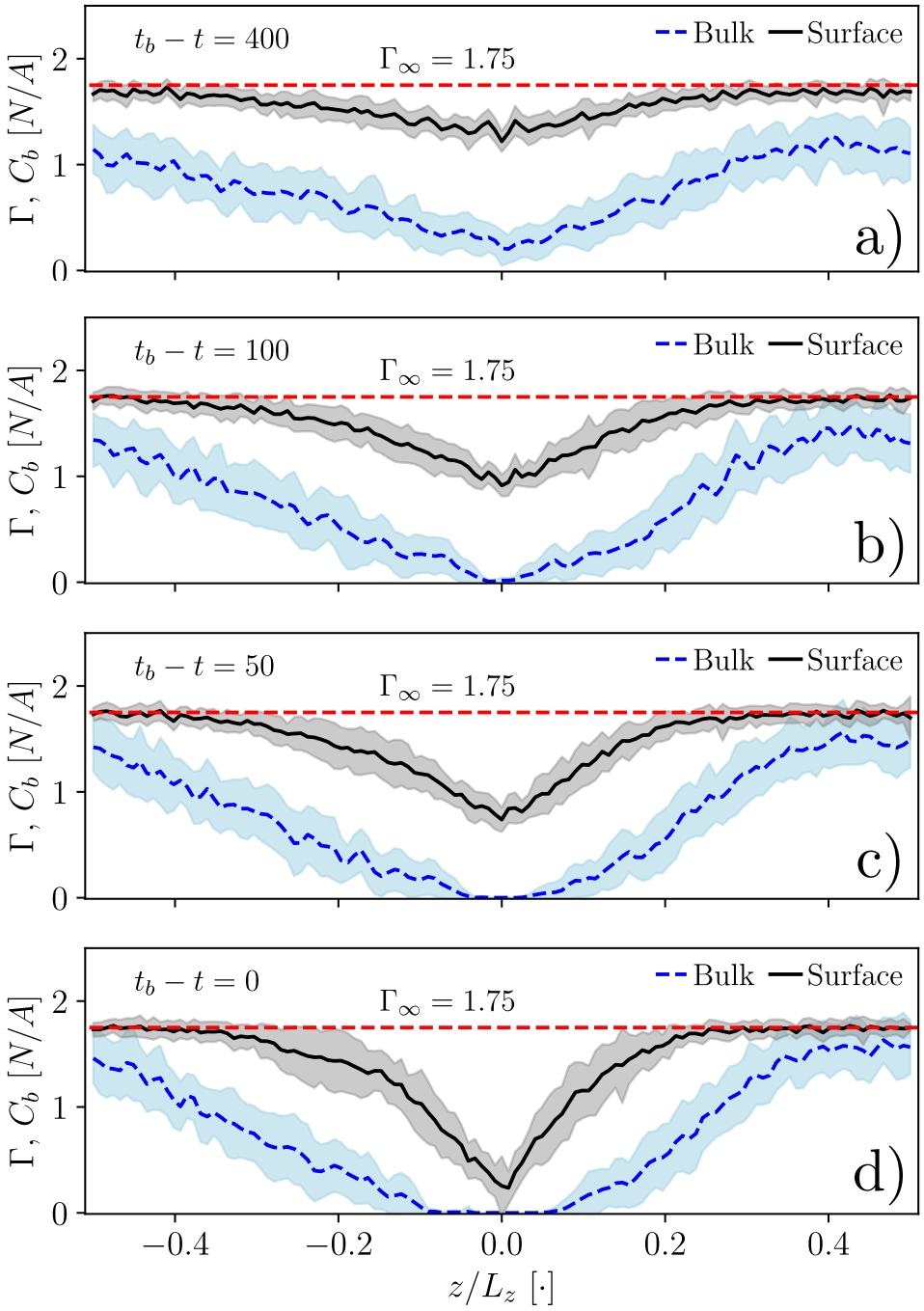

FIGURE 4.11: Time evolution of the surfactant distribution for a case above CMC ($C = 2.9$) showing the advection of surfactants from the pinching point and increase in bulk surfactant in the main droplet region. Γ is the surface-excess concentration and C_b is the bulk concentration (number of molecules per surface area). Reprinted from Carnevale et al. [85] with permission by AIP Publishing.

the thinning process. Interestingly, this artificial regime scales as $h_{\text{min}} \sim e^{\tau}$, which

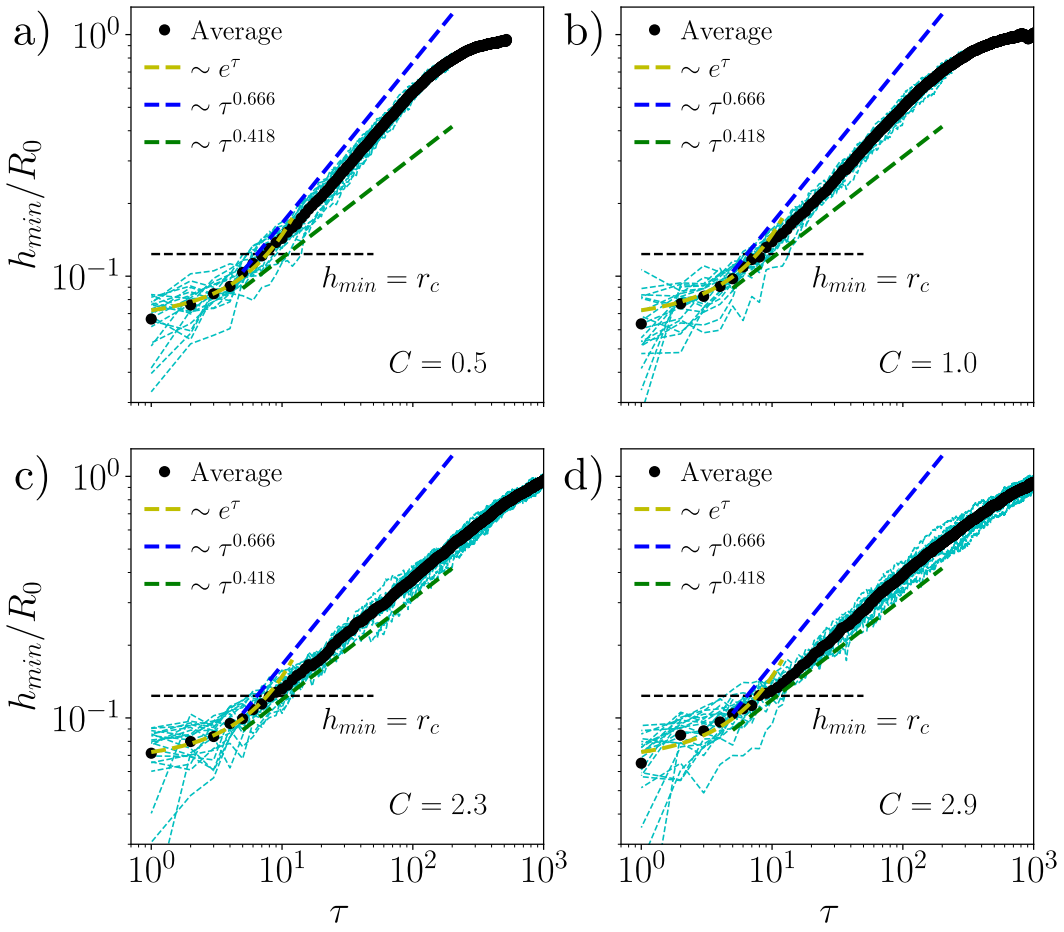

FIGURE 4.12: Radius scaling of the thinning process for threads with four different surfactant concentrations and comparison with known breakup regimes. a) $C = 0.5$; b) $C = 1.6$; c) $C = 2.3$; d) $C = 2.9$. Each case is an ensemble average of 20 simulations, indicated by the black dots. r_c is the cutoff distance for the attractive interaction. Dashed lines were added just as reference to the theoretical regimes and have the same values in all plots. Reprinted with permission from Ref. [85].

is a regime observed for viscoelastic fluids [89] and for special surfactant cases when they are not advected from the pinching point [35, 36].

4.4 Conclusions

In this chapter, we provided a comprehensive investigation of the breakup dynamics of surfactant-laden liquid threads, focusing on how surfactants influence the process under thermal fluctuations. By utilizing MDPD and the coarse-grained SDS model, this research successfully captured key interfacial properties

like surface tension, micelle formations above the CMC and interfacial thickness variation. Our results demonstrate that our method and model are a robust tool for simulating surfactant behavior in real liquids.

A detailed study of the breakup of liquid threads revealed that increased surfactant concentration leads to longer breakup times and larger unstable wavelengths. While the initial increase in breakup time and wavelength can be explained by the decrease in surface tension, the continued trend at concentrations above the CMC suggests the emergence of bulk viscous effects, caused by the growing number of micelles. These findings highlight the importance of considering both surface and bulk properties when studying surfactant-laden systems.

Lastly, we observed a shift in thinning dynamics from the inertial regime toward the thermal fluctuation regime as surfactant concentration increases. We found that, at the lowest concentration investigated, instead of the predicted viscous regime, the dynamics were mostly governed by inertia. Nonetheless, this is in agreement with experimental observations [32]. We also argued that the presence of a new "breakup" regime closer to the pinch-off is likely an artifact of the simulation method as the transition happens when the thinning neck radius falls below the interaction cutoff between particles.

Chapter 5

Conclusion

The thesis presents a detailed investigation into the dynamics of liquid thread breakup, focusing on the Rayleigh–Plateau instability and its role in droplet formation. This classical instability, driven by surface tension, causes perturbations along a liquid thread to grow, ultimately leading to fragmentation into droplets. While macroscopic theories have provided insight into this process, this study emphasizes the molecular-level interactions and nanoscale effects, such as thermal fluctuations and viscous forces, that influence droplet dynamics. Using many-body dissipative particle dynamics (MDPD) simulations, key parameters, including the characteristic wavenumber, were quantified to assess the stability and fragmentation of liquid threads.

The study first analyzed the breakup of pure liquid threads under varying conditions characterized by the Ohnesorge number (Oh), which encapsulates the interplay between inertial, viscous, and surface tension forces. A strong correlation was observed between the characteristic wavenumber and the Ohnesorge number, aligning with theoretical predictions from stability analysis. This finding validates the use of MDPD as a powerful mesoscale modeling tool capable of accurately simulating droplet formation processes.

In addition, the study explored the formation of satellite droplets, which are smaller droplets generated alongside main droplets during thread breakup. A clear power-law relationship was identified between the number of satellite droplets and the combined Ohnesorge and Thermal capillary (OhTh) numbers. The results show that as viscosity increases, satellite droplet formation is suppressed due to the dampening of thinning neck dynamics by viscous forces.

The study also revealed that the size of the main droplets depends closely on the characteristic wavelength of the breakup process. However, deviations from

expected scaling laws were observed at higher Ohnesorge numbers. These deviations were attributed to asynchronous breakup events and longer timescales in viscous fluids, where the pinching dynamics are slower and result in larger main droplets. The thesis extended the investigation to surfactant-laden liquid threads, which introduce additional complexity due to their ability to reduce surface tension and create surface tension gradients. Surfactants, being amphiphilic molecules, alter the breakup process significantly by influencing both the thread's interfacial and bulk properties.

The results show that increasing surfactant concentration leads to longer breakup times and larger unstable wavelengths. Initially, these changes are explained by the reduction in surface tension, which increases the Ohnesorge number. However, above the critical micelle concentration (CMC), surface tension becomes constant, and the continued increase in breakup time and wavelength is attributed to bulk viscous effects arising from the formation of micelles.

Furthermore, the study identified a transition in thinning dynamics from an inertial regime to a thermal fluctuation regime as surfactant concentration increased. At low concentrations, the breakup was governed by inertia, which aligns with experimental observations, even though viscous or visco-inertial regimes are typically expected. At higher concentrations, the dynamics shifted towards the thermal fluctuation regime, where nanoscale thermal effects dominate.

Detailed simulations provided molecular-level insights into the surfactant distribution during thread breakup. The findings show that surfactant gradients along the interface induce the Marangoni effect, which opposes the flow and slows the breakup process. This effect is particularly pronounced at high surfactant concentrations, where the suppression of satellite droplets was observed.

The study also noted a potential artifact in the MDPD model, where the thinning neck radius approaches the particle interaction cutoff during the final stages of breakup. This transition causes a disproportionate slowdown in thinning dynamics due to the dominance of attractive forces, suggesting that further refinement of the simulation method is needed for extremely small length scales.

This research has significant implications for practical applications where precise droplet control is essential, such as inkjet printing, and spray formation. The ability to manipulate droplet size and minimize satellite formation through surfactant concentration offers new opportunities for optimizing industrial processes.

In conclusion, this thesis advances the understanding of liquid thread breakup by integrating molecular insights with mesoscale simulations. Future research could

extend these findings by exploring more complex fluids, incorporating external forces, or further refining MDPD to capture even smaller-scale dynamics. Some of our ongoing work in developing MDPD has been placed in the appendix of this thesis, as its main topic goes well beyond the main droplet breakup theme. These efforts will pave the way for innovative droplet manipulation techniques in both scientific and industrial contexts.

Appendix A

Martini coarse-graining approach with MDPD

A.1 Introduction

Molecular dynamics (MD) simulations are a cornerstone in computational sciences, being a powerful tool to study the behavior of systems at the atomic and molecular level [90]. The popularity of the MD method can be partially attributed to the many well-documented, open-source, free, software, such as LAMMPS [91, 92] and GROMACS [93]. At the core of MD lies the force-field, a mathematical model that governs the interactions among particles. Moreover, the reliability of MD simulations depends on the ability of the force-field to replicate key physical properties of the system under specific conditions, such as surface tension for surfactant-laden interfaces [94].

As the complexity and size of simulated systems grow, all-atom force-fields become inconvenient due to the higher computational demand. This can be mitigated by representing groups of atoms as single interaction sites in what are known as coarse-grained (CG) models [95–98]. Among various CG force-fields, the Martini force-field [56, 99–101] stands out as a versatile and widely adopted model that is constantly being improved [57]. Part of the success of the Martini force-field is due its modular approach, where particles are mainly classified in terms of their polarity. This classification allows the use of different particles as building blocks to construct various molecules.

Despite the success of Martini within the MD paradigm, the computational demands of MD remain a consideration for large-scale systems or phenomena requiring long simulation times. Many-body dissipative particle dynamics (MDPD) is an alternative to MD that offers the potential to lower the computational cost. The improvement comes from MDPD's use of a soft potential, which

allows for larger time steps in simulations [9, 53, 55, 80, 102, 103]. In general, MDPD is suitable for simulating multi-phase and multi-component systems that are much larger than in MD [29, 55, 67, 85].

This appendix explores the synergy between the Martini approach and the MDPD method. We start by giving an overview of the MD method and the protocol used in our simulations. Afterwords, we parametrize the interactions in the MDPD version of the Martini force-field by following Martini's top–down approach based on water–octanol partition coefficients [104]. We further compare the performance of MD and MDPD in simulating CG lipid models. The results presented in this appendix have been partially published (see Ref. [29]). Unpublished results have been submitted for publication and are under review.

A.2 Molecular dynamics

Molecular dynamics is a particle based method that aims to simulate the movement of atoms and molecules over time. At its core, MD integrates Newton's equations of motion for a collection of particles, where forces are derived from interaction potentials. The main difference between MD and the MDPD method, described in Chapter 2, is in the choice of potential functions. Typically MD uses the Lennard-Jones (LJ) pair potential to describe the interaction between particles. The form of this potential is:

$$U(r_{ij}) = 4\epsilon_{ij}\left[\left(\frac{\sigma_{ij}}{r_{ij}}\right)^{12} - \left(\frac{\sigma_{ij}}{r_{ij}}\right)^{6}\right] \tag{A.1}$$

where r_{ij} is the distance between the center of particles i and j, and σ_{ij} and ϵ_{ij} are parameters of the pair interaction, respectively. The LJ potential is shown in Fig. A.1 with the influence of its parameters indicated. The potential crosses the x axis at $r_{ij} = \sigma_{ij}$ and the energy depth of the potential is equal to ϵ_{ij}. As is the case in MDPD, MD also computes the interactions between particles only up to a given cutoff distance.

A.2.1 Martini MD force-field

The Martini MD force-field has been under development for over 20 years and has found success in a wide range of applications. It has been used to simulate complex molecules, such as proteins [105–108], polymers [109], carbohydrates [110], glycolipids [111], glycans [112], DNA [113], RNA [114], water [115], and

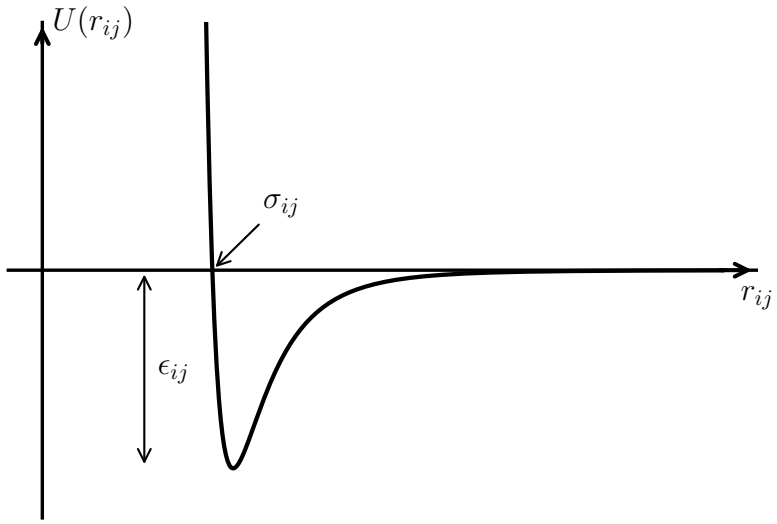

FIGURE A.1: The Lennard-Jones potential, given in Eq. A.1, models the interaction between a pair of particles as a function of their separation distance, r_{ij}. The potential reaches zero at $r_{ij} = \sigma_{ij}$. The minimum value of the potential, which represents the most stable energy state of the system, occurs at a depth of ϵ_{ij}.

various solvents [116], while various extensions include simulations for specific pH [117] and more recently chemical reactions [118].

In general, Martini maps four heavy atoms and their associated hydrogens to one particle. Nonbonded interactions are parametrized by changing the well depth of the LJ potential, that is, by changing ϵ_{ij} in Eq. A.1. Originally, every particle was considered to have the same size, σ_{ij}. However, a recent version of the force-field have incorporated different size choices for each class of particle [57]. Martini has different classes of particles that are used to represent nonpolar, intermediately polar, polar and charged chemical groups. Further subclasses are defined to provide different levels of interaction. The simulations presented in this appendix were done with Martini 2.0 [56], while the most recent version is 3.0 [57]. The nonbonded interactions between the particles used to build the lipid models in Section A.4 is presented in Tab. A.1. It is important to note that, in total, Martini 2.0 has 18 different particles that can interact through 10 different energy levels. Charged particles also interact via the Coulombic potential

$$U_{el}(r_{ij}) = \frac{q_i q_j}{4\pi\varepsilon_0\varepsilon_r r_{ij}}, \tag{A.2}$$

where q_i is the charge of particle i, ε_0 the vacuum dielectric constant, and the dielectric constant $\varepsilon_r = 15$.

Martini represents bonded interactions between different particles by the harmonic potential

$$E_{\text{bond}} = \frac{k_{\text{bond}}}{2}\left(r_{ij} - r_0\right)^2, \tag{A.3}$$

where r_0 is the bond equilibrium distance. For the sake of simplicity, and as is usually done in CG models [119], all bonds have the same harmonic potential coefficient, $k_{\text{bond}} = 1250$ kJ mol^{-1}nm^{-2}, and equilibrium distance $r_0 = 0.47$ nm. Stiffness of molecule chains is described by the harmonic cosine potential

$$E_{\text{angle}} = \frac{k_{\text{angle}}}{2}\left[\cos(\theta_{ijk}) - \cos(\theta_0)\right]^2, \tag{A.4}$$

where θ_{ijk} is the angle between the vectors $\mathbf{r}_i - \mathbf{r}_j$, and $\mathbf{r}_k - \mathbf{r}_j$ of three consecutive beads with ids i, j, and k. The equilibrium angle θ_0 depends on specific molecular structures, and the harmonic potential constant value is $k_{\text{angle}} = 45$ kJ mol^{-1} for all interactions.

A.3 MDPD-Martini force-field parametrization

Much like in the Martini MD force-field, we choose one parameter to represent the different levels of interactions between particles in the MDPD parametrization. Due to MDPD's "no-go" theorem [42], the value of the parameter B in Eq. 2.21 has to be constant. Therefore, the attractive coefficients A_{ij} are used in the parametrization. Furthermore, we make the usual choice of keeping $B = 25$.

Bonds have been modeled with the same harmonic potential in Eq. A.3, however with the parameters $k_{\text{bond}} = 150$, and $r_0 = 0.5$, in MDPD units. In our MDPD

TABLE A.1: Martini MD 2.0 interaction matrix for particles used to build the lipid models in Section A.4. Roman numerals denote the different energy levels ϵ_{ij}: 5.6 (O); 5.0 (I); 4.5 (II); 4.0 (III); 3.5 (IV); 3.1 (V); 2.7 (VI); 2.3 (VII); 2.0 (VIII); 2.0 (IX); all in units of kJ/mol. The parameter $\sigma_{ij} = 0.47$ nm for all interaction levels except level IX for which $\sigma_{ij} = 0.62$ nm.

	Q_a	Q_0	P_4	N_a	C_1	C_3
Q_a	I	II	O	III	IX	VII
Q_0		IV	O	III	IX	VII
P_4			I	III	VIII	VI
N_a				III	VI	VI
C_1					IV	IV
C_3						IV

force-field, we have used the harmonic angle potential,

$$E_{\text{angle}} = \frac{k_{\text{angle}}}{2}\left(\theta_{ijk} - \theta_0\right)^2, \tag{A.5}$$

to model chain stiffness. All angle interactions use the same coefficient value, $k_{\text{angle}} = 5$.

The parametrization between different A_{ij} interactions is done by computing water–octanol partition coefficients. This approach was used because the partition coefficients are a useful tool to classify particles in terms of their polarity, which is the same top–down approach used in the development of the Martini MD force-field.

First, we prepare our reference system by parametrizing the water particles. Differently than Martini 2.0, we have decided to use a specific particle to model water, named W particle, to be in line with the more recent Martini 3.0. We set the water–water self interaction $A_{ww} = -50$ by definition and then scaled some simulation properties to the properties of real water to obtain a mapping between MDPD and real units. This scaling procedure is explained in Chapter 2. We then proceed to parametrize the C_1 particles, which represent 4 carbon atoms and are used to compose the octanol molecule. To this end, we conduct a series of MDPD simulations with only octane, built from two bonded C_1 particles. By systematically varying their self interaction value, we matched simulated surface tension values to that of experimental measurements. Surface tension in our simulations can be calculated from Eq. 2.34, and the same procedure is also explained in Chapter 3. The same surface tension matching procedure was done to obtain the self interaction between N_a particles. In this case, they were matched with diethylene glycol, built from two bonded N_a particles [88]. Finally, the cross interaction between water particles and C_1 particles was obtained by matching their interfacial tension to that of water–octane interfaces.

With most of our reference system parametrized, we now build a simulation box where half of its domain is composed of water particles and the other half by octanol molecules. The octanol is built by bonding a N_a particle to a C_1 particle. To obtain the remaining cross interaction parameters, we systematically vary their values and, now, match it to the partition coefficient for water particles in the octanol phase and octanol molecules in the water phase. The water–octanol partition coefficients were calculated by measuring the molar concentrations of solute molecules in the water, $[S]_w$, and octanol phases, $[S]_o$, following a similar

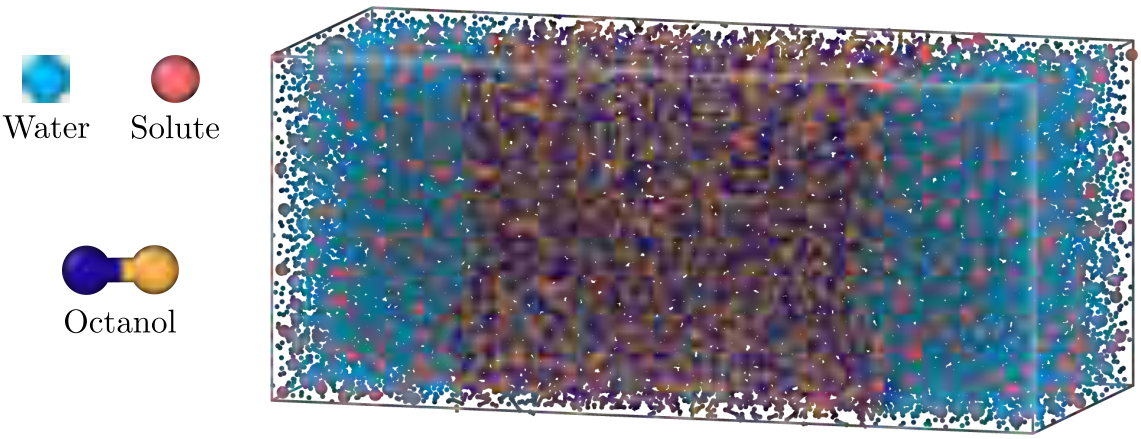

FIGURE A.2: (a) Typical simulation snapshot of a water–octanol system used for the parametrization of a solute particle (red bead) based on the water–octanol partitioning (Equation A.6). Reprinted from Ref. [29].

procedure as in a previous study [104]. The partition coefficient is defined as

$$\log P = \log \frac{[S]_o}{[S]_w}. \tag{A.6}$$

Our method of measuring $\log P$ is limited to the size and the amount of solute particles used in the system. We directly measure molar concentrations as the ratio between the number of solute particles to the number of solvent particles in each phase. The maximum (or minimum) $\log P$ value scales as $\log N$, where N is the number of solute particles. The systems used in our parametrization procedure were composed of 1500 solute particles, which gives the upper and lower limits of our measurements as $\log P_{o/w} = \pm 3.17$. However, this limitation does not compromise our approach as most chemical substances can be found within these limits [120]. The last type of particle parametrized was a Q_a /Q_0 particle, which will represent the head chemical group of the lipid model used. In the Martini MD force-field, the particles Q_a and Q_0 are charged, have distinct interactions and represent different groups in the CG lipid models used. However, we decided to model both head groups with a single type particle and we assume that the Coulomb interactions will be represented through the choice of A_{ij}. All its interaction values were obtained from the water–octanol simulation presented in Fig. A.2. As this is a more polar chemical group, we set the desired $\log P = -1.7$ to reproduce that of phosphocholine [121], which is a combination of the choline and phosphate groups represented by the Q_0 and Q_a particles in Martini MD, respectively.

The final values of all the interactions in our force-field are presented in Tab. A.2. Our partition coefficient measurements using those interaction values agree well with experimental data, with water in octanol exhibiting a $\log P$ of 1.3 (experimental) and 1.4 (simulated), while octanol in water shows a $\log P$ of 3.1 (experimental) and 2.9 (simulated). The accuracy of the model is further validated by comparing the calculated ethylene glycol (single N_a particles) $\log P$ values (-1.5), which closely match the experimental value -1.4 [122, 123].

A.4 Coarse-grained lipid models

In this appendix, we showcase our MDPD force-field parametrization in a composite system consisting of water and different lipids [87, 124], which serves as a benchmark in the simulation of biological membranes. We further compare our results with MD simulations of the same models. Three phosphatidylcholine lipids were chosen for our simulations, DPPC, DOPC, and POPC. These lipids are distinguished by their respective aliphatic chains. Figure A.3 shows the CG model of the three lipids and the respective particle labels used. Note that the particle C_3 is used to model the unsaturated part of the chains in the POPC and DOPC molecules.

The particles used represent the following chemical groups [99]:

- Q_0 – Choline;
- Q_a – Phosphate;
- N_a – Glycerol ester;
- C_1 – saturated carbon part;
- C_3 – unsaturated carbon part;
- W/P_4 – Water.

Angle potentials were defined for all possible combinations of three consecutive particles. An equilibrium angle value of $\theta_0 = 120°$ was used for the triplets: Q_a

TABLE A.2: Interaction matrix for parametrized MDPD beads organized in five interaction levels (I-VI) with corresponding attractive parameters (A): -50 (I); -43 (II); -34 (III); -30 (IV); -28 (V); -26 (VI).

	W	Q_a /Q_0	N_a	C_1	C_3
W	I	I	II	VI	V
Q_a /Q_0		IV	II	VI	V
N_a			III	VI	V
C_1				VI	VI
C_3					VI

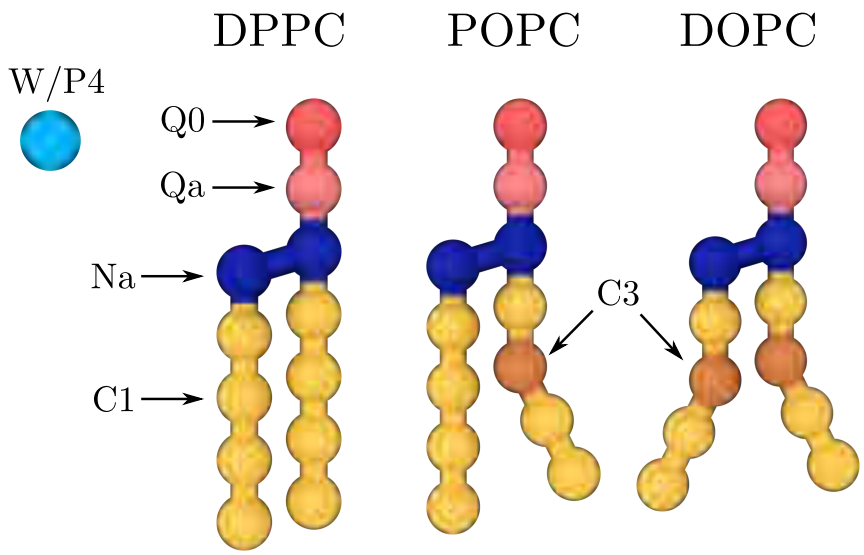

FIGURE A.3: MD and MDPD-Martini models of different lipid molecules and water.

–Na–Na; Na–Na–C_1; C_1–C_3–C_1. All other angles were set with the equilibrium value $\theta_0 = 180°$.

A.5 Simulation setup

We use Martini's online tutorials [125] as a benchmark for comparison. These tutorials were originally implemented using GROMACS software [93], however, we have used LAMMPS [91, 92] to carry out both MD and MDPD simulations. Our MD simulations were adapted from a Moltemplate software example [62, 126].

All our simulations were initialized with a randomly distributed system of water particles and lipid molecules in a 10:1 ratio, respectively. Three sizes of systems were evaluated at first and characterized by the number of lipid molecules. The initial simulation box was defined as a cube with dimensions $L = 70$ Å, 90 Å, and 120 Å, for MD systems with, 128, 256, and 512 lipid molecules, respectively. Equivalently, the box dimensions were, $L = 8.2$, 10.5, and 14 in MDPD units. We begin our simulations by minimizing the system's energy before integrating the equations of motion, to avoid strong numerical oscillations and unphysical instabilities that could arise due to the improper placement of the randomly distributed particles.

Following this minimization, we start evolving the MD system in an NPT ensemble employing the Nosé–Hoover thermostat, keeping the temperature constant at

300 K and pressure at 1 bar. This step relaxes the system until we obtain an equilibrium box volume. Subsequently, we run the system under NVT conditions, now with a temperature set to 450 K to remove any undesired structures that may have formed. Finally, we lower the temperature back to 300 K and run an NPT simulation again until a final lipid bilayer has formed without any defects. The MDPD simulations were run entirely with an NVT ensemble at $k_BT = 1$ after the initial minimization, until the final bilayer was formed. Lastly, the equilibrium properties of theses bilayer were measured by running NPT simulations at zero surface tension condition for both MD and MDPD. This condition is achieved by coupling the pressure barostat in the bilayer plane. Some results were obtained by replicating a bilayer already formed and in equilibrium to achieve a larger system.

A.6 Results

A.6.1 Self-assembly

Lipids tend to aggregate when in solution and form what is known as a bilayer. Figure A.4 shows this aggregation process for a system with 512 DPPC molecules, simulated with our Martini MDPD force-field. Interestingly, the bilayer formation process follows the same dynamics as in previous Martini MD studies [99].

As presented in Fig. A.4, initially, the lipid molecules are randomly distributed in the simulation box and, after a short amount of time, they start to form small aggregates ($t = 30\ \tau$). These clusters try to keep the hydrophobic chains closer together in the inside part of the aggregates, away from the water phase, to minimize the interaction energy of the system. The small clusters, however, start to coalesce and form larger aggregates ($t = 100\tau$). These structures, subsequently, undergo further transformations until a bilayer configuration starts to form. The initial bilayer configuration ($t = 200\tau$) exhibits two kinds of defects — pores, and lipid bridges. These defects vanish over time, resulting in a final defect-free structure ($t = 300\tau$).

The same aggregation procedure is observed for POPC and DOPC, both in MD and MDPD simulations. Our first comparison between both simulation methods regards the computational time required to produce a defect-free bilayer. Table A.3 presents our results for the different system sizes considered. The time comparison was done with simulations on the same machine, Intel Core i7-10700 @

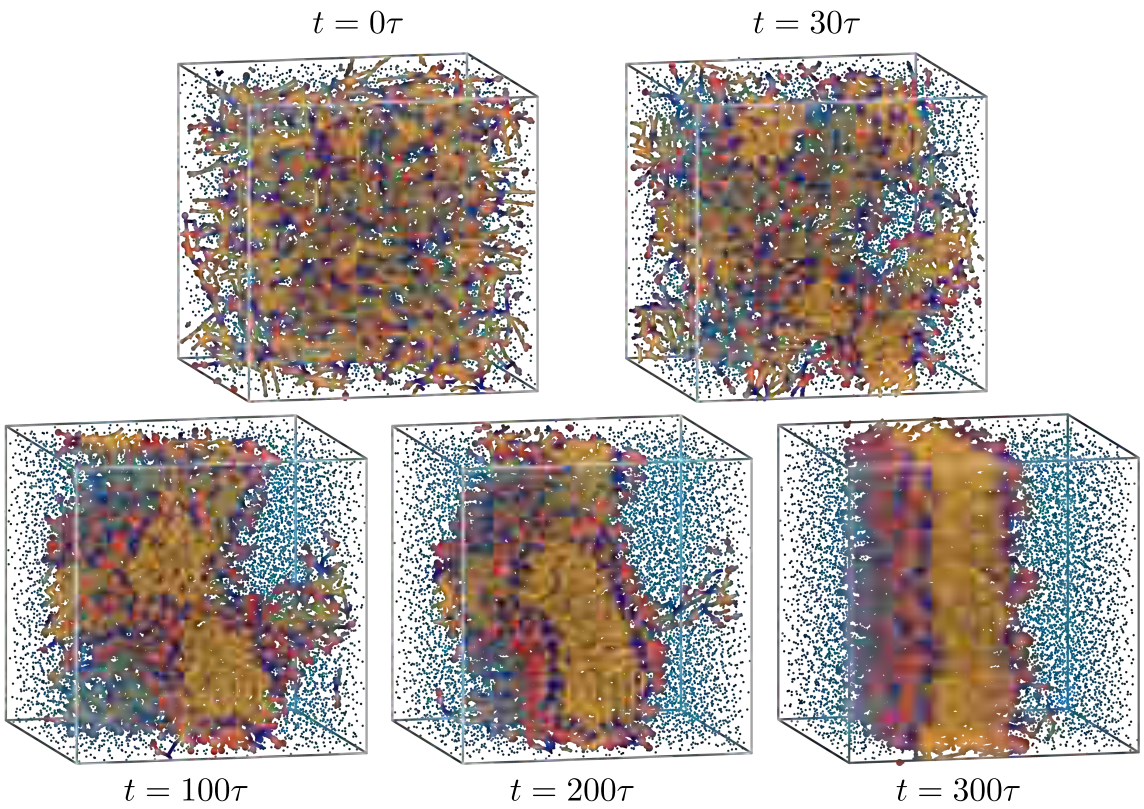

FIGURE A.4: Snapshots illustrate the gradual formation of the DPPC bilayer over time, starting from a random distribution of 512 lipid molecules, which aggregate into clusters and then coalesce to produce the lipid bilayer. Time τ is in MDPD reduced units. Size of particles was modified for better visualization. Adapted from Ref. [29].

2.9 GHz, and running on 8 CPU cores. Our findings demonstrate that a considerable acceleration in computational efficiency is possible when using the soft, short-range interactions in the MDPD method.

A.6.2 Area per lipid and thickness

The area per lipid (APL) is a property of lipid bilayers that quantifies how much surface area is occupied by a single lipid molecule. From our simulations, this can be obtained directly by dividing the area of the simulation box face in the tangential plane of the bilayer by half the total number of lipids, N_{lipids}. If we assume the bilayer normal is in the z direction, then, $\text{APL} = 2L_xL_y/N_{\text{lipids}}$.

The thickness of a lipid bilayer is also an important property that depends on its constituent molecules. To measure this property, we calculate density profiles along the normal direction of the bilayer. All particles in the simulation box were divided into 250 equally spaced bins in the z direction and their partial densities

were computed as the number of particles of type i in the bin divided by the volume of the bin. Such profiles are presented in Fig. A.5 for both MD and MDPD simulations. Since we decided to use the same interactions for the head group particles in the MDPD force-field, instead of separately defining interactions for the Q_a and Q_0 particles, we compare the bilayer thickness by measuring the distance between Q_a density peaks.

Results from the APL and thickness measurements are presented in Tab. A.4. Our MD bilayers closely reproduce the expected values for both properties when compared to recent simulation literature using the most recent and optimized version of Martini MD [124]. Our MDPD force-field was able to attain similar thickness values, however, the APL measurements are underestimated, on average, by 6.1 $Å^2$. It is important to also note that, even with this difference, the MDPD simulations exhibited the same trend in the reduction of APL as the thickness increased. This trend can be explained by the unsaturation in the POPC and DOPC chains, which creates a kink in their chain structure. As a result, the molecules occupy slightly larger areas.

A.6.3 Secon rank order parameter

Further structural comparisons between our MDPD force-field and the MD force-field are done by computing the second-rank order parameter [127, 128]

$$P_2 = \frac{1}{2}\left(3\langle\cos^2\theta\rangle - 1\right), \tag{A.7}$$

where θ is the angle between a given bond direction and the bilayer normal direction. The P_2 parameter, thus, indicates the level of alignment of each segment of a molecule with respect to the bilayer. A value of $P_2 = 1$ indicates perfect alignment, $P_2 = 0$ a random orientation and $P_2 = -0.5$ anti-alignment.

TABLE A.3: Time comparison of simulation runs on eight cores Intel Core i7-10700 @ 2.9 GHz for the formation of a bilayer with no defects. Successful formation highly depends on initial configuration, but MDPD is always four to seven times faster than MD. Three system sizes were considered, with 128, 256, and 512 lipid molecules; all with a 10:1 proportion of water beads for both MDPD and MD.

System size	128	256	512
MDPD	20 s	1.5 min	5 min
MD	70 s	5 min	35 min

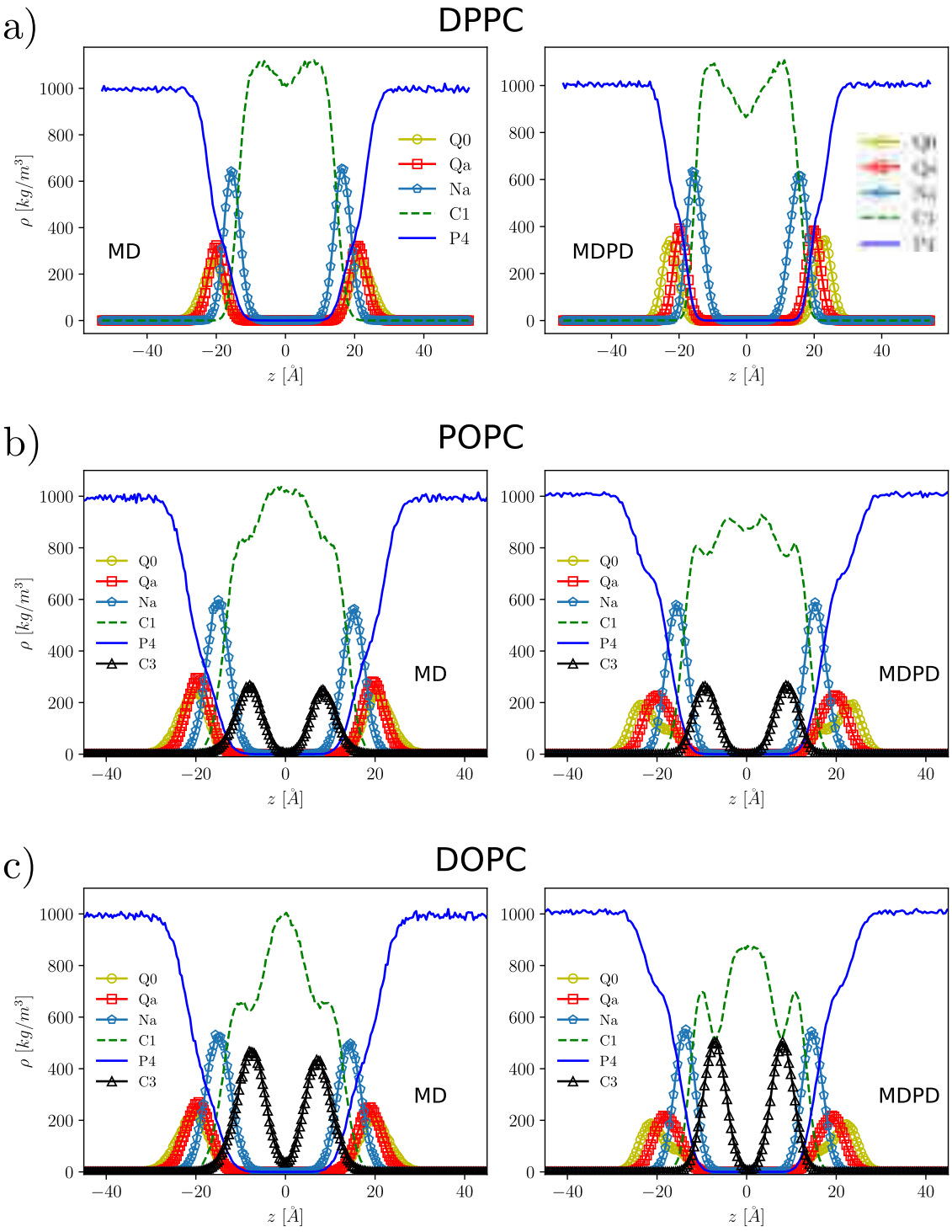

FIGURE A.5: Comparison of bilayer thickness in MDPD and MD simulations. Density profiles from MDPD and MD simulations, with a bilayer thickness measured between the peaks of the Q_0 particle. All simulations consist of 512 lipid molecules. Results for DOPC (a) were adapted from Ref. [29].

The results presented in Fig. A.6 were obtained by averaging the values over all the molecules in our larger systems (512 lipids), at the end of each simulation.

They were also averaged over both aliphatic chains on each molecule, at the same positions. The MDPD simulations successfully reproduced results comparable to those from MD simulations, particularly for DOPC lipids. The divergence observed near the ends of the hydrophobic tails in DPPC molecules, and to a lesser extent in POPC molecules, may be attributed to the harmonic angle potential parameters used for the saturated chains. This indicates that a model refinement procedure might be necessary to accurately model chain stiffness.

A.6.4 Bending modulus

Lipid bilayers are extensively studied for their elastic properties, quantified by the bending modulus, k_c [129]. The bending modulus reflects the membrane's resistance to bending, with a higher value indicating a stiffer membrane. Understanding this property is crucial for insights into cellular mechanics, such as vesicle formation. To obtain larger undulations and properly measure the bending modulus, each lipid system containing 512 lipids was replicated in both x and y directions to create a larger membrane of 8192 lipids. Mathematically, the bending modulus governs the long wavelength undulation behavior of a membrane through the relation

$$\langle \hat{u}^2 \rangle = \frac{k_B T}{A k_c q^4}, \tag{A.8}$$

where $\hat{u}$ is the Fourier spectrum of undulations, $A = L_x L_y$ is the lipid membrane area, $q = |\mathbf{q}| = \sqrt{q_x^2 + q_y^2}$ the wavevector length in Fourier space.

These undulations are analyzed using a height function by marking the lipid's head group particles as reference points. Deviations of these reference points from the average position of the bilayer plane gives a surface $u(x,y)$, as depicted

TABLE A.4: MDPD and MD measurements of area per lipid and bilayer thickness for the different lipid molecules considered. Both methods produce membranes of comparable thickness, while the current MDPD force-field underestimates the APL.

		MDPD	MD
DPPC	APL	46.2 Å^2	51.6 Å^2
	Thickness	44.2 Å	44.0 Å
POPC	APL	54.3 Å^2	61.6 Å^2
	Thickness	40.1 Å	39.5 Å
DOPC	APL	59.1 Å^2	64.7 Å^2
	Thickness	37.8 Å	38.4 Å

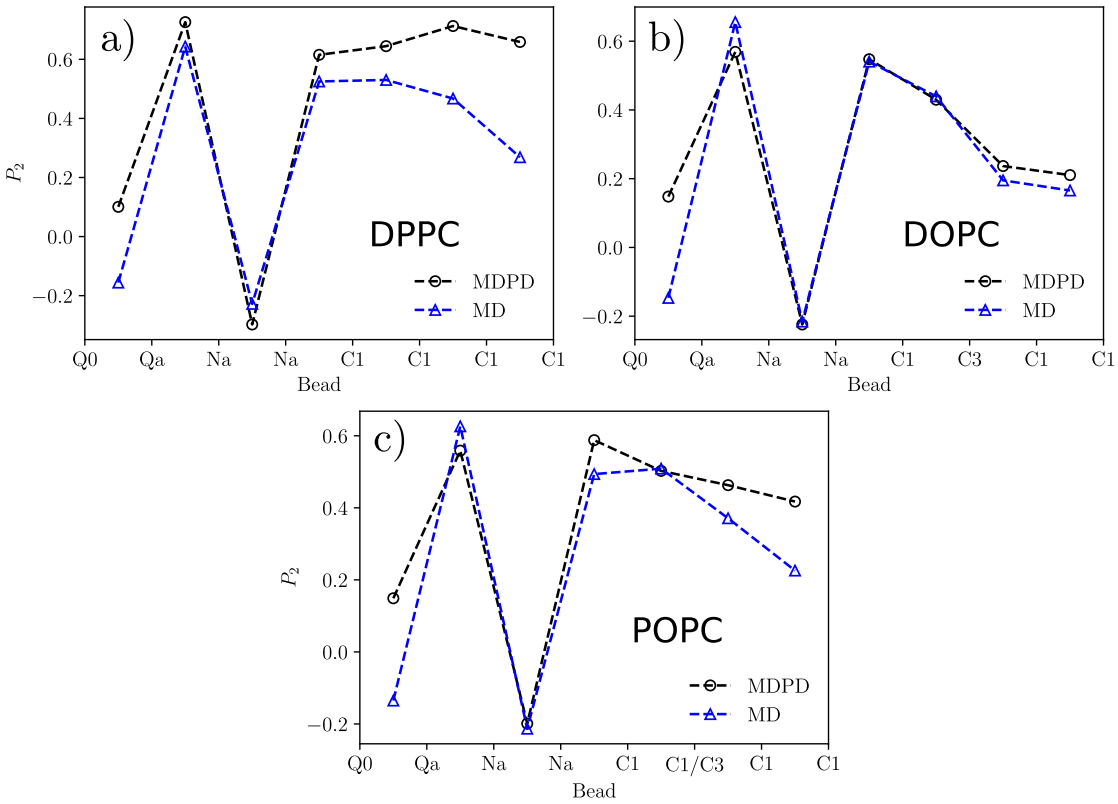

FIGURE A.6: Second rank order parameter calculated for every bond in the lipid molecule. The data is averaged over all the bonds in the bilayers consisting of 512 lipids. Each plot compares MD and MDPD results of the lipids: (a) DPPC (adapted from Ref. [29]); b) DOPC; c) POPC.

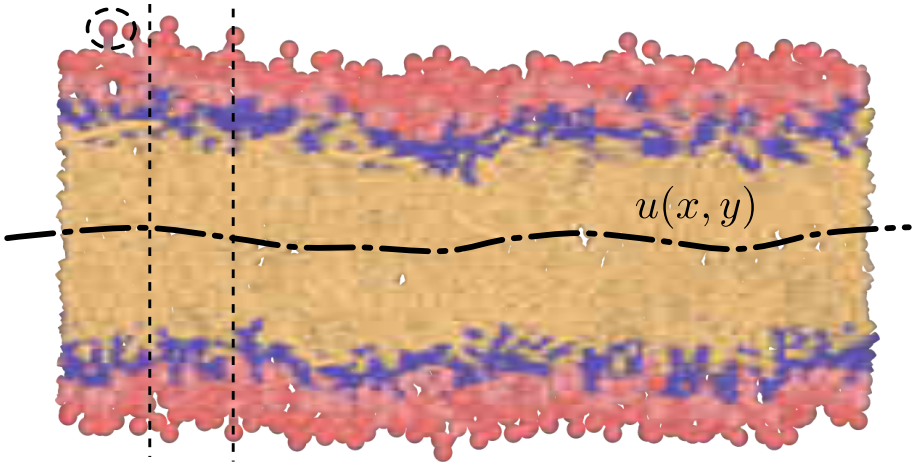

FIGURE A.7: Undulating surface of a lipid membrane obtained by averaging the positions of the choline head groups at different bins (dashed lines) in the x and y directions.

in Fig. A.7. The undulation spectrum is found by applying the Fourier transform

$$\hat{u}(\mathbf{q}) = \frac{1}{N} \int u(\mathbf{x}) e^{-i\mathbf{q}\cdot\mathbf{x}} \mathbf{dx}. \tag{A.9}$$

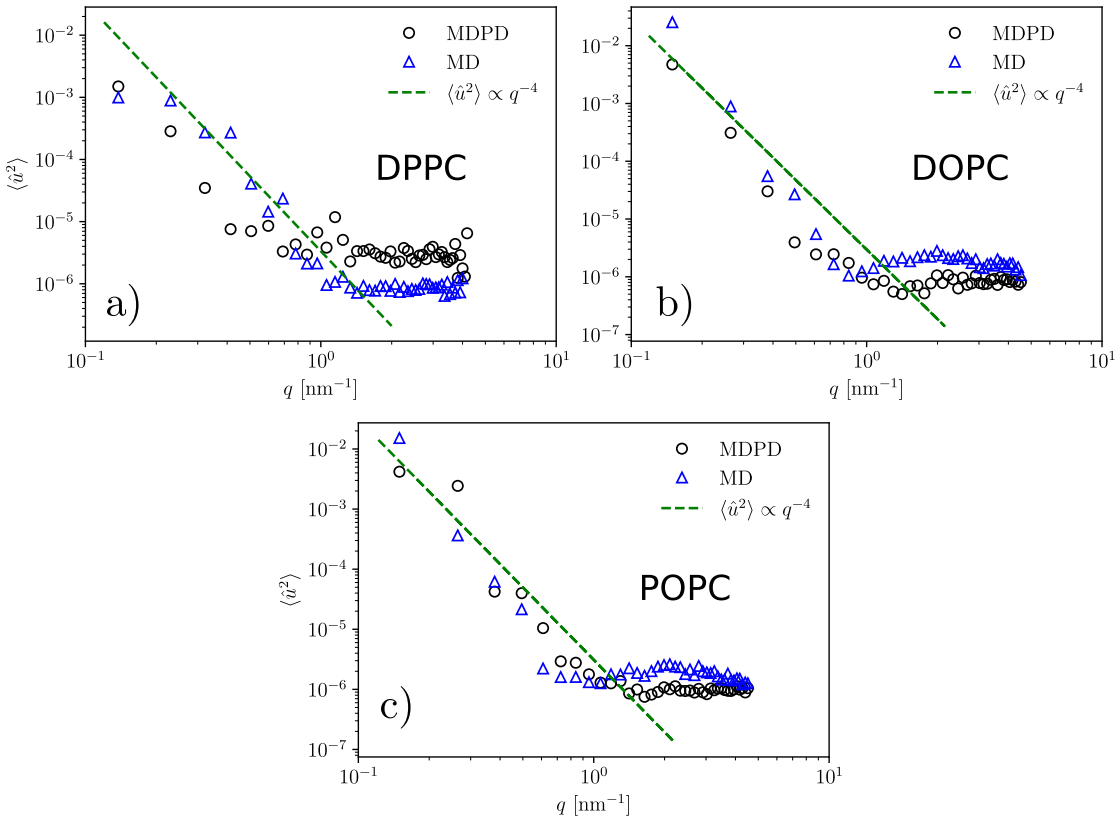

FIGURE A.8: Spectrum intensities of the undulation modes of the bilayer. Long wavelengths obey the q^{-4} behavior, transitioning to a constant value around a 1 nm wavelength. The data is averaged for 200 snapshots sampled over 2×10^5 time steps of a system consisting of 8192 lipids. Each plot compares MD and MDPD results of the lipids: a) DPPC; b) DOPC; c) POPC.

Figure A.8 shows the undulation power spectrum for all the membranes considered. The undulation intensities, predicted by Eq. A.8, display a characteristic scaling of $u \sim q^{-4}$ for long wavelengths. This same scaling is observed in all our simulations, both MD and MDPD, making it clear that our force-field is capable of reproducing the elastic properties of lipid membranes. Moreover, the dashed line in every plot shows a bending modulus value of $k_c = 5 \times 10^{-20}$ J, which has been experimentally obtained [130]. This long wavelength behavior transitions to a constant undulation intensity around 1 nm, which is also consistent with other MD simulations of lipid membranes [99].

A.7 Conclusions

This study has demonstrated the efficacy of the MDPD force-field as a compelling alternative to the widely utilized MD framework for coarse-grained simulations.

Both methodologies proved capable of generating defect-free lipid bilayer structures with comparable self-aggregation dynamics, while also yielding structural properties — such as area per lipid, bilayer thickness, bending modulus, and orientation order parameter — that closely align with experimental observations.

Notably, the MDPD method offers a significant advantage through its reliance on soft, short-range interactions, enabling faster simulations without compromising essential system properties. This computational efficiency is particularly valuable in the context of large-scale molecular simulations, where the ability to explore increasingly complex, large systems is of paramount importance.

Moreover, the inherent adaptability of MDPD-Martini further underscores its potential toward a general-purpose force-field, with the flexibility to incorporate additional interaction levels, diverse bead types, and varying bead sizes. Such versatility positions MDPD as a robust tool for simulating a wide range of molecular systems, expanding the scope of coarse-grained simulations.

Bibliography

(1) Savart, F. *Annales de chimie* **1833**, *55*, 257–310.

(2) Plateau, J. *Mémoires de l'Académie royale de Belgique* **1849**, *23*, 1–150.

(3) Rayleigh, L. *Proceedings of the London Mathematical Society* **1878**, *s1-10*, 4–13.

(4) Moseler, M.; Landman, U. *Science* **2000**, *289*, 1165–1169.

(5) Eggers, J. *Physical Review Letters* **2002**, *89*, 084502.

(6) Aarts, D. G. A. L.; Schmidt, M.; Lekkerkerker, H. N. W. *Science* **2004**, *304*, 847–850.

(7) Petit, J.; Riviére, D.; Kellay, H.; Delville, J. P. *Proceedings of the National Academy of Sciences of the United States of America* **2012**, *109*, 18327–18331.

(8) Hennequin, Y.; Aarts, D. G. A. L.; van der Wiel, J. H.; Wegdam, G.; Eggers, J.; Lekkerkerker, H. N. W.; Bonn, D. *Physical Review Letters* **2006**, *97*, 244502.

(9) Warren, P. B. *Physical Review E: Statistical Physics, Plasmas, Fluids, and Related Interdisciplinary Topics* **2003**, *68*, 066702.

(10) Pagonabarraga, I.; Frenkel, D. *Molecular Simulation* **2000**, *25*, 167–175.

(11) Español, P.; Warren, P. *Europhysics Letters* **1995**, *30*, 191.

(12) Basaran, O. A. *AIChE Journal* **2002**, *48*, 1842–1848.

(13) Kuz, V. A. *Physical Review E: Statistical Physics, Plasmas, Fluids, and Related Interdisciplinary Topics* **1994**, *49*, 1246–1250.

(14) Ueda, T.; Gao, Q. Z.; Yamaichi, E.; Yamagishi, C.; Akiyama, M. *Journal of Crystal Growth* **1994**, *145*, 707–713.

(15) Chen, A. U.; Basaran, O. A. *Physics of Fluids* **2002**, *14*, L1–L4.

(16) Nielsen, N. J. *Hewlett-Packard Journal* **1985**, *36*, 4–10.

(17) Basaran, O. A.; Gao, H.; Bhat, P. P. *Annual Review of Fluid Mechanics* **2013**, *45*, 85–113.

(18) Boland, T.; Xu, T.; Damon, B.; Cui, X. *Biotechnology Journal* **2006**, *1*, 910–917.

(19) Mansour, N. N.; Lundgren, T. S. *Physics of Fluids A: Fluid Dynamics* **1990**, *2*, 1141–1144.

(20) Montanero, J. M.; Gañán-Calvo, A. M. *Reports On Progress in Physics* **2020**, *83*, 097001.

(21) Clanet, C.; Lasheras, J. C. *Journal of Fluid Mechanics* **1999**, *383*, 307–326.

(22) Utada, A. S.; Fernandez-Nieves, A.; Stone, H. A.; Weitz, D. A. *Physical Review Letters* **2007**, *99*, 094502.
(23) Eggers, J. *Physical Review Letters* **1993**, *71*, 3458–3460.
(24) Papageorgiou, D. T. *Physics of Fluids* **1995**, *7*, 1529–1544.
(25) Eggers, J. *Reviews of Modern Physics* **1997**, *69*, 865–930.
(26) Eggers, J.; Villermaux, E. *Reports On Progress in Physics* **2008**, *71*, 036601.
(27) Castrejón-Pita, J. R.; Castrejón-Pita, A. A.; Thete, S. S.; Sambath, K.; Hutchings, I. M.; Hinch, J.; Lister, J. R.; Basaran, O. A. *Proceedings of the National Academy of Sciences of the United States of America* **2015**, *112*, 4582–4587.
(28) Schmiedel, P.; von Rybinski, W. In *Chemistry and Technology of Surfactants*; John Wiley & Sons, Ltd: 2006; Chapter 3, pp 46–90.
(29) Carnevale, L. H.; Theodorakis, P. E. *The European Physical Journal Plus* **2024**, *139*, 539.
(30) Goodarzi, F.; Zendehboudi, S. *Canadian Journal of Chemical Engineering* **2019**, *97*, 281–309.
(31) Doi, M., *Soft Matter Physics*; Oxford University Press: 2013.
(32) Kovalchuk, N. M.; Nowak, E.; Simmons, M. J. H. *Langmuir : the ACS journal of surfaces and colloids* **2016**, *32*, 5069–5077.
(33) Kovalchuk, N. M.; Jenkinson, H.; Miller, R.; Simmons, M. J. *Journal of Colloid and Interface Science* **2018**, *516*, 182–191.
(34) Wee, H.; Wagoner, B. W.; Kamat, P. M.; Basaran, O. A. *Physical Review Letters* **2020**, *124*, 204501.
(35) Wee, H.; Wagoner, B. W.; Basaran, O. A. *Physical Review Fluids* **2022**, *7*, 074001.
(36) Martínez-Calvo, A.; Sevilla, A. *Physical Review Letters* **2020**, *125*, 114502.
(37) Hoogerbrugge, P. J; Koelman, J. M. V. A *Europhysics Letters* **1992**, *19*, 155–160.
(38) Groot, R. D.; Warren, P. B. *Journal of Chemical Physics* **1997**, *107*, 4423–4435.
(39) Trofimov, S. Y.; Nies, E. L. F.; Michels, M. A. J. *Journal of Chemical Physics* **2002**, *117*, 9383–9394.
(40) Thompson, A. P.; Aktulga, H. M.; Berger, R.; Bolintineanu, D. S.; Brown, W. M.; Crozier, P. S.; in 't Veld, P. J.; Kohlmeyer, A.; Moore, S. G.; Nguyen, T. D.; Shan, R.; Stevens, M. J.; Tranchida, J.; Trott, C.; Plimpton, S. J. *Computer Physics Communications* **2022**, *271*, 108171.
(41) Vanya, P.; Elliott, J. A. *Physical Review E: Statistical Physics, Plasmas, Fluids, and Related Interdisciplinary Topics* **2020**, *102*, 013312.
(42) Warren, P. B. *Physical Review E: Statistical Physics, Plasmas, Fluids, and Related Interdisciplinary Topics* **2013**, *87*, 045303.

(43) Jamali, S.; Boromand, A.; Khani, S.; Wagner, J.; Yamanoi, M.; Maia, J. *Journal of Chemical Physics* **2015**, *142*, 164902.

(44) Vanya, P.; Crout, P.; Sharman, J.; Elliott, J. A. *Physical Review E: Statistical Physics, Plasmas, Fluids, and Related Interdisciplinary Topics* **2018**, *98*, 033310.

(45) Arienti, M.; Pan, W.; Li, X.; Karniadakis, G. *Journal of Chemical Physics* **2011**, *134*, 204114.

(46) Kirkwood, J. G.; Buff, F. P. *Journal of Chemical Physics* **1949**, *17*, 338–343.

(47) Ghoufi, A.; Malfreyt, P. *The Journal of Chemical Physics* **2011**, *135*, 104105.

(48) Ghoufi, A.; Malfreyt, P. *Physical Review E: Statistical Physics, Plasmas, Fluids, and Related Interdisciplinary Topics* **2011**, *83*, 051601.

(49) Ghoufi, A.; Emile, J.; Malfreyt, P. *The European Physical Journal E* **2013**, *36*, 10.

(50) Tolman, R. C. *The Journal of Chemical Physics* **1949**, *17*, 333–337.

(51) Lei, Y. A.; Bykov, T.; Yoo, S.; Zeng, X. C. *Journal of the American Chemical Society* **2005**, *127*, 15346–15347.

(52) Marsh, C. A.; Backx, G.; Ernst, M. H. *Physical Review E: Statistical Physics, Plasmas, Fluids, and Related Interdisciplinary Topics* **1997**, *56*, 1676–1691.

(53) Zhao, J.; Chen, S.; Phan-Thien, N. *Molecular Simulation* **2017**, *44*, 213–224.

(54) Zhao, J.; Zhou, N.; Zhang, K.; Chen, S.; Liu, Y.; Wang, Y. *Physical Review E: Statistical Physics, Plasmas, Fluids, and Related Interdisciplinary Topics* **2020**, *102*, 023116.

(55) Zhao, J.; Chen, S.; Zhang, K.; Liu, Y. *Physics of Fluids* **2021**, *33*, 112002.

(56) Marrink, S. J.; Risselada, H. J.; Yefimov, S.; Tieleman, D. P.; de Vries, A. H. *Journal of Physical Chemistry B* **2007**, *111*, 7812–7824.

(57) Souza, P. C. T. et al. *Nature Methods* **2021**, *18*, 382–388.

(58) Groot, R.; Rabone, K. *Biophysical Journal* **2001**, *81*, 725–736.

(59) Vanya, P.; Sharman, J.; Elliott, J. A. *The Journal of Chemical Physics* **2019**, *150*, 064101.

(60) Li, Z.; Hu, G.-H.; Wang, Z.-L.; Ma, Y.-B.; Zhou, Z.-W. *Physics of Fluids* **2013**, *25*, 072103.

(61) Martínez, L.; Andrade, R.; Birgin, E. G.; Martínez, J. M. *Journal of Computational Chemistry* **2009**, *30*, 2157–2164.

(62) Jewett, A. I.; Stelter, D.; Lambert, J.; Saladi, S. M.; Roscioni, O. M.; Ricci, M.; Autin, L.; Maritan, M.; Bashusqeh, S. M.; Keyes, T.; Dame, R. T.; Shea, J.-E.; Jensen, G. J.; Goodsell, D. S. *Journal of Molecular Biology* **2021**, *433*, 166841.

(63) Stukowski, A. *Modelling and Simulation in Materials Science and Engineering* **2010**, *18*, 015012.

(64) Hoath, S. D., *Fundamentals of Inkjet Printing: The Science of Inkjet and Droplets*; John Wiley & Sons: Cambridge, 2016.
(65) Wu, H.; Zhang, F.; Zhang, Z. *Physics of Fluids* **2021**, *33*, 013317.
(66) Ye, Y. Y.; Biswas, R; Morris, J. R.; Bastawros, A; Chandra, A *Nanotechnology* **2003**, *14*, 390–396.
(67) Carnevale, L. H.; Deuar, P.; Che, Z.; Theodorakis, P. E. *Physics of Fluids* **2023**, *35*, 074108.
(68) Plateau, J., *Statique expérimentale et théorique des liquides soumis aux seules forces moléculaires*; Paris, Gauthier-Villars: 1873; Vol. 2.
(69) Rayleigh, L. J. W. S. *Proceedings of the Royal Society of London Series A* **1879**, *29*, 71–97.
(70) Rayleigh, L. *The London, Edinburgh, and Dublin Philosophical Magazine and Journal of Science* **1892**, *34*, 145–154.
(71) Chandrasekhar, S., *Hydrodynamic and Hydromagnetic Stability*; Oxford University Press: 1961.
(72) Weber, C. *Journal of Applied Mathematics and Mechanics* **1931**, *11*, 136–154.
(73) Lafrance, P. *The Physics of Fluids* **1975**, *18*, 428–432.
(74) Tiwari, A.; Abraham, J. *Microfluid. Nanofluidics* **2008**, *4*, 227–235.
(75) Gopan, N.; Sathian, S. P. *Physical Review E: Statistical Physics, Plasmas, Fluids, and Related Interdisciplinary Topics* **2014**, *90*, 033001.
(76) Zhao, C.; Lockerby, D. A.; Sprittles, J. E. *Physical Review Fluids* **2020**, *5*, 044201.
(77) Theodorakis, P. E.; Paul, W.; Binder, K. *Europhysics Letters* **2009**, *88*, 63002.
(78) Virtanen, P. et al. *Nature Methods* **2020**, *17*, 261–272.
(79) Danilov, D.; Barner-Kowollik, C.; Wenzel, W. *Chemical Communications* **2015**, *51*, 6002–6005.
(80) Zhao, C.; Zhao, J.; Si, T.; Chen, S. *Physics of Fluids* **2021**, *33*, 112004.
(81) Cohen, I.; Brenner, M. P.; Eggers, J.; Nagel, S. R. *Physical Review Letters* **1999**, *83*, 1147–1150.
(82) Cohen, I.; Nagel, S. R. *Physics of Fluids* **2001**, *13*, 3533–3541.
(83) Zhang, W. W.; Lister, J. R. *Physical Review Letters* **1999**, *83*, 1151–1154.
(84) Martínez-Calvo, A.; Rivero-Rodríguez, J.; Scheid, B.; Sevilla, A. *Journal of Fluid Mechanics* **2020**, *883*, A35.
(85) Carnevale, L. H.; Deuar, P.; Che, Z.; Theodorakis, P. E. *Physics of Fluids* **2024**, *36*, 033301.
(86) Zhou, P.; Hou, J.; Yan, Y.; Wang, J.; Chen, W. *Langmuir : the ACS journal of surfaces and colloids* **2019**, *35*, 8110–8120.
(87) Zhu, Y.; Bai, X.; Hu, G. *Biophysical Journal* **2021**, *120*, 4751–4762.

(88) Hendrikse, R. L.; Amador, C.; Wilson, M. R. *Soft Matter* **2023**, *19*, 3590–3604.
(89) Chang, H.-C.; Demekhin, E. A.; Kalaidin, E. *Physics of Fluids* **1999**, *11*, 1717–1737.
(90) Rapaport, D. C. In *The Art of Molecular Dynamics Simulation*, 2nd ed.; Cambridge University Press: Cambridge, 2004.
(91) Plimpton, S. *Journal of Computational Physics* **1995**, *117*, 1–19.
(92) Thompson, A. P.; Aktulga, H. M.; Berger, R.; Bolintineanu, D. S.; Brown, W. M.; Crozier, P. S.; in 't Veld, P. J.; Kohlmeyer, A.; Moore, S. G.; Nguyen, T. D.; Shan, R.; Stevens, M. J.; Tranchida, J.; Trott, C.; Plimpton, S. J. *Computer Physics Communications* **2022**, *271*, 108171.
(93) Berendsen, H.; van der Spoel, D.; van Drunen, R. *Computer Physics Communications* **1995**, *91*, 43–56.
(94) Arbabi, S.; Deuar, P.; Denys, M.; Bennacer, R.; Che, Z.; Theodorakis, P. E. *Physics of Fluids* **2023**, *35*, 063329.
(95) Noid, W. G. *Journal of Chemical Physics* **2013**, *139*, 090901.
(96) Kmiecik, S.; Gront, D.; Kolinski, M.; Wieteska, L.; Dawid, A. E.; Kolinski, A. *Chemical Reviews* **2016**, *116*, 7898–7936.
(97) Jin, J.; Pak, A. J.; Durumeric, A. E. P.; Loose, T. D.; Voth, G. A. *Journal of Chemical Theory and Computation* **2022**, *18*, 5759–5791.
(98) Noid, W. G. *Journal of Physical Chemistry B* **2023**, *127*, 4174–4207.
(99) Marrink, S. J.; de Vries, A. H.; Mark, A. E. *Journal of Physical Chemistry B* **2004**, *108*, 750–760.
(100) Marrink, S. J.; Tieleman, D. P. *Chemical Society Reviews* **2013**, *42*, 6801–6822.
(101) Alessandri, R.; Grünewald, F.; Marrink, S. J. *Advanced Materials* **2021**, *33*, 2008635.
(102) Pagonabarraga, I.; Frenkel, D. *Journal of Chemical Physics* **2001**, *115*, 5015–5026.
(103) Han, Y.; Jin, J.; Voth, G. A. *Journal of Chemical Physics* **2021**, *154*, 084122.
(104) Anderson, R. L.; Bray, D. J.; Ferrante, A. S.; Noro, M. G.; Stott, I. P.; Warren, P. B. *Journal of Chemical Physics* **2017**, *147*, 094503.
(105) Monticelli, L.; Kandasamy, S. K.; Periole, X.; Larson, R. G.; Tieleman, D. P.; Marrink, S.-J. *Journal of Chemical Theory and Computation* **2008**, *4*, 819–834.
(106) Periole, X.; Cavalli, M.; Marrink, S.-J.; Ceruso, M. A. *Journal of Chemical Theory and Computation* **2009**, *5*, 2531–2543.
(107) de Jong, D. H.; Singh, G.; Bennett, W. F. D.; Arnarez, C.; Wassenaar, T. A.; Schäfer, L. V.; Periole, X.; Tieleman, D. P.; Marrink, S. J. *Journal of Chemical Theory and Computation* **2013**, *9*, 687–697.

(108) Poma, A. B.; Cieplak, M.; Theodorakis, P. E. *Journal of Chemical Theory and Computation* **2017**, *13*, 1366–1374.

(109) Lee, H.; de Vries, A. H.; Marrink, S.-J.; Pastor, R. W. *Journal of Physical Chemistry B* **2009**, *113*, 13186–13194.

(110) López, C. A.; Rzepiela, A. J.; de Vries, A. H.; Dijkhuizen, L.; Hünenberger, P. H.; Marrink, S. J. *Journal of Chemical Theory and Computation* **2009**, *5*, 3195–3210.

(111) López, C. A.; Sovova, Z.; van Eerden, F. J.; de Vries, A. H.; Marrink, S. J. *Journal of Chemical Theory and Computation* **2013**, *9*, 1694–1708.

(112) Chakraborty, S.; Wagh, K.; Gnanakaran, S; López, C. A. *Glycobiology* **2021**, *31*, 787–799.

(113) Uusitalo, J. J.; Ingólfsson, H. I.; Akhshi, P.; Tieleman, D. P.; Marrink, S. J. *Journal of Chemical Theory and Computation* **2015**, *11*, 3932–3945.

(114) Uusitalo, J. J.; Ingólfsson, H. I.; Marrink, S. J.; Faustino, I. *Biophysical Journal* **2017**, *113*, 246–256.

(115) Yesylevskyy, S. O.; Schäfer, L. V.; Sengupta, D.; Marrink, S. J. *Plos Computational Biology* **2010**, *6*, 1–17.

(116) Vainikka, P.; Thallmair, S.; Souza, P. C. T.; Marrink, S. J. *ACS Sustainable Chemistry & Engineering* **2021**, *9*, 17338–17350.

(117) Grünewald, F.; Souza, P. C. T.; Abdizadeh, H.; Barnoud, J.; de Vries, A. H.; Marrink, S. J. *Journal of Chemical Physics* **2020**, *153*, 024118.

(118) Sami, S.; Marrink, S. J. *Journal of Chemical Theory and Computation* **2023**, *19*, 4040–4046.

(119) Müller, E. A.; Jackson, G. *Annual Review of Chemical and Biomolecular Engineering* **2014**, *5*, 405–427.

(120) Ulrich, N.; Goss, K.-U.; Ebert, A. *Communications Chemistry* **2021**, *4*, 90.

(121) For Biotechnology Information, N. C. PubChem Compound Summary for CID 1014, Phosphocholine, https://pubchem.ncbi.nlm.nih.gov/compound/Phosphocholine.

(122) Organization, W. H., www.inchem.org/#/.

(123) Lang, B. E. *Journal of Chemical & Engineering Data* **2012**, *57*, 2221–2226.

(124) Empereur-mot, C.; Pedersen, K. B.; Capelli, R.; Crippa, M.; Caruso, C.; Perrone, M.; Souza, P. C. T.; Marrink, S. J.; Pavan, G. M. *Journal of Chemical Information and Modeling* **2023**, *63*, 3827–3838.

(125) Martini Tutorials: Lipids with the Lipidome, https://cgmartini.nl/docs/tutorials/Legacy/martini2/lipids_and_lipidome.html, 2023.

(126) Moltemplate Examples, https://www.moltemplate.org/visual_examples.html, 2023.

(127) Lafrance, C.-P.; Nabet, A.; Prud'homme, R. E.; Pézolet, M. *Canadian Journal of Chemistry-revue Canadienne De Chimie* **1995**, *73*, 1497–1505.

(128) Chremos, A.; Theodorakis, P. E. *Polymer* **2016**, *97*, 191–195.

(129) Tarazona, P.; Chacón, E.; Bresme, F. *Journal of Chemical Physics* **2013**, *139*, 094902.

(130) Rawicz, W.; Olbrich, K.; McIntosh, T.; Needham, D.; Evans, E. *Biophysical Journal* **2000**, *79*, 328–339.